Akbar, Jehan (2012) High power mode locked lasers monolithically integrated with semiconductor optical amplifiers. PhD thesis

http://theses.gla.ac.uk/3461/

High Power Mode Locked Lasers monolithically Integrated with Semiconductor Optical Amplifiers

Jehan Akbar

March 2012

A thesis submitted in partial fulfilment for the degree of

Doctor of Philosophy (Ph.D)

in the

College of Science & Engineering

School of Engineering

Declaration of Authorship

I, Jehan Akbar, declare that this thesis titled "High Power Mode Locked Lasers with Integrated Semiconductor Optical amplifiers" and the contributions presented in it are my own. I confirm that:

- This work was done wholly or mainly while in candidature for a research degree at this University.

- Where any part of this thesis has previously been submitted for a degree or any other qualification at this University or any other institution, this has been clearly stated.

- Where I have consulted the published work of others, this is always clearly attributed.

- Where I have quoted from the work of others, the source is always given. With the exception of such quotations, this thesis is entirely my own work.

- I have acknowledged all main sources of help.

- Where the thesis is based on work done by myself jointly with others, I have made clear exactly what was done by others and what I have contributed myself.

Signed: Jehan Akbar

Date: 01/March/2012

In the name of Allah, the most Merciful, the most Beneficent.

Abstract

This thesis is concerned with the design, fabrication and characterisation of high power semiconductor mode locked lasers (SMLLs), operating at ~ 1.5 μm. The devices are based on a novel epitaxial structure with three quantum wells (QW) in the active region. The novel epitaxial structure was based on a commercially available five-QW AlGaInAs/InP epitaxial structure, with the number of QWs reduced to increase the gain saturation energy and a farfield reduction layer (FRL), and a spacer layer were inserted in the n-cladding layer. SMLLs based on both the five-QW and three-QW material, were fabricated and comparatively investigated. The devices based on the three-QW material exhibited an increased average output power, as well as reduced RF linewidth and pulse widths. The average output power obtained in the mode locked operation from a 40 GHz MLL, based on this three-QW material was limited to 28 mW. Single mode ridge waveguide semiconductor optical amplifiers (SOAs) were monolithically integrated with the SMLLs, which increased the average output power to 130 mW. The devices performance was investigated at both the saturable absorber (SA) and SOA facets. Transform limited pulses with a minimum duration of 3.3 ps and a peak power of > 1 W were obtained at the SOA facet. To take advantage of the higher saturation output power of the tapered SOAs, SMLLs were monolithically integrated with 2° and 6° tapered SOAs, respectively. The devices integrated with 2° tapered SOAs were mounted on Aluminium Nitride (*AlN*) sub-mounts using Gold-Tin (*AuSn*) soldering for better heat sinking. These devices resulted in an average output power of 200 mW, with corresponding peak power > 1.2 W. The SMLLs integrated with 6° tapered SOAs, mounted on conventional brass sub-mounts resulted in a lower output power (105 mW), compared to the devices integrated with ridge waveguide and 2° tapered SOAs, respectively.

List of Publications

(a)   Peer reviewed Publications directly related to this thesis work:

1. **<u>Jehan Akbar</u>**, Lianping Hou, Mohsin Haji, Michael Strain, John H. Marsh, A. Catrina. Bryce and Anthony. E. Kelly, "High power (130 mW) 40 GHz mode-locked DBR lasers with integrated optical amplifiers", *Optics letters Vol*. 37, *Issue 3, 2012.*

2. **<u>Jehan Akbar</u>**, Lianping Hou, Mohsin Haji, Michael John Strain, Piotr Stolarz, John H. Marsh, A. Catrina. Bryce and Anthony. E. Kelly, "High peak power (550 mW) 40 GHz mode-locked DBR lasers with integrated optical amplifier", *IEEE PHOTONICS CONFERENCE, Arlington, USA, 2011.*

3. **<u>Jehan Akbar</u>**, Lianping Hou, Mohsin Haji, Rafal Dylewicz, Michael Strain, John H. Marsh, A. Catrina. Bryce and Anthony. E. Kelly, "High average power (200 mW) 40 GHz mode-locked DBR lasers with integrated tapered optical amplifiers", Conference on Lasers and Electro-Optics *(CLEO) San Jose, California USA*, 2012.

4. **<u>Jehan Akbar</u>**, Lianping Hou, Mohsin Haji, Michael Strain, Michael Strain, John, A. Catrina. Bryce and Anthony. E. Kelly, "200 mW average output power 40 GHz mode-locked DBR lasers with integrated tapered optical amplifiers", in preparation for submission to *Optics Letters*.

(b)   Peer reviewed Publications not directly related to this thesis work:

5. Lianping Hou, M. Haji, **<u>Jehan Akbar</u>**, Bocang Qiu, A. Catrina. Bryce, "Low divergence angle and low jitter 40 GHz AlGaInAs/InP 1.55 μm mode-locked lasers," *Optics. Letters, Vol. 36, No.6, 2011.*

6. Lianping Hou, Mohsin Haji, Bocang Qiu, **Jehan Akbar**, A. C. Bryce, J. H. Marsh, "10 GHz AlGaInAs/InP 1.55 μm Passively Mode-Locked Laser with Low Divergence Angle and Timing Jitter," *IEEE Photonics. Technology. Letters, Vol. 23, No.15, 2011.*

7. Lianping Hou, M. Haji, **Jehan Akbar**, John H. Marsh, A. Catrina. Bryce, "CWDM source based on AlGaInAs/InP monolithically integrated DFB laser array" *Optics letters Vol. 36, No.21, 2011.*

8. Lianping Hou, M. Haji, **Jehan Akbar**, John H. Marsh, A. Catrina. Bryce, "AlGaInAs/InP Monolithically Integrated DFB Laser Array," *Journal of Quantum Electronics. Vol. 48, No.2, 2012.*

9. Mohsin Haji, Lianping Hou, Anthony E. Kelly, **Jehan Akbar**, John H. Marsh, John M. Arnold, Charles. N. Ironside, "High frequency optoelectronic oscillators based on the optical feedback of semiconductor mode-locked laser diodes" *Optics Express. Vol. 20 No 3, 2012.*

10. Lianping Hou, M. Haji, **Jehan Akbar**, John H. Marsh, A. Catrina. Bryce, "160 GHz 1.55 μm Colliding-Pulse Mode-Locked AlGaInAs/InP Laser with High Power and Low Divergence Angle," *IEEE Photonics. Technology. Letters, Vol. 24, No.12, 2012.*

11. Ann Catrina Bryce, Lianping Hou, Mohsin Haji, Jehan Akbar and John Marsh, "Low-cost light source for optical fiber communication systems," *SPIE Newsroom. DOI: 10.1117/2.1201204.004228, 2012.*

12. Mohsin Haji, Lianping Hou, Anthony E. Kelly, **Jehan Akbar**, John H. Marsh, John M. Arnold, and Charles N. Ironside "Ultralow 192 Hz RF linewidth optoelectronic oscillator Ultralow 192 Hz RF linewidth optoelectronic oscillator" Conference on Lasers and Electro-Optics *(CLEO) San Jose, California USA*, 2012.

13. Lianping Hou, M. Haji, **<u>Jehan Akbar</u>**, A. C. Bryce, J. H. Marsh, "Colliding-Pulse Mode-Locked AlGaInAs Laser Operating at 20 GHz with Narrow RF Linewidth" *IEEE PHOTONICS CONFERENCE, Arlington, USA, 2011*.

14. C. N. Ironside, Mohsin Haji, Lianping Hou, **<u>Jehan Akbar</u>**, Anthony E. Kelly, K. Seunarine, Bruno Romeira, and José M. L. Figueiredo. "Review of optoelectronic oscillators based on mode locked lasers and resonant tunneling diode optoelectronics", *Applications of Optics and Photonic (AOP), Braga 2011, (Invited paper)*.

15. Lianping Hou, M. Haji, C. Li, **<u>Jehan. Akbar</u>**, J. H. Marsh, Ann Bryce "80-GHz AlGaInAs/InP 1.55 μm colliding-pulse mode-locked laser with low divergence angle and timing jitter," *CLEO/Europe-EQEC Conference Munich, Germany, 2011*.

16. Lianping Hou, **<u>Jehan Akbar</u>**, Mohsin Haji, Piotr Stolarz, R. Dylewicz, A. Kelly, M. Sorel, John Marsh, Ann Bryce; B.C. Qiu, "40 GHz AlGaInAs/InP 1.55 μm passively mode-locked laser with low divergence angle and timing jitter," *Conference on Lasers and Electro-optics, Baltimore, Maryland, USA, 2011*.

(c) Non-Peer reviewed Publications:

17. **<u>Jehan Akbar</u>**, A. C. Bryce and A. E. Kelly, "Tapered Semiconductor Optical Amplifiers," *Engineering Postgraduate Conference, Glasgow, UK, 2010*.

18. Mohsin Haji, Lianping Hou, **<u>Jehan Akbar</u>**, Anthony E. Kelly, C. N. Ironside, "All Optical regeneratively mode-locked laser diode with a 40GHz repetition rate" *9th mm wave meeting, University of Glasgow, UK, 2011*.

Acknowledgements

Table of Contents

List of Figures

To my Parents.

Table of Abbreviations

Symbol	Description	Symbol	Description
AlGaInAs	Aluminium Gallium Indium Arsenide	MQW	multiple quantum well
AR	antireflection	OCDMA	optical code division multiple access
BPM	beam propagation method	OTDM	optical time division multiplexing
CW	continuous wave	PECVD	plasma enhanced chemical vapour deposition
DBR	distributed Bragg reflector	PMMA	polymethyl methacrylate
DC	direct current	QCSE	quantum confined stark effect
DH	Double heterostructure	QW	quantum Well
e-beam	electron-beam	RF	radio frequency
EBL	electron-beam lithography	RIE	reactive ion etching
EDFA	erbium doped fiber amplifier	RTA	rapid thermal annealer
FP	Fabry-Perot	RWG	ridge waveguide
FSR	free spectral range	SA	saturable absorber
FRL	farfield reduction layer	SS	spot size
FWHM	full width half maximum	SEM	scanning electron microscope
GaAs	Gallium Arsenide	SHG	second harmonic generation
GaInAsP	Gallium Indium Arsenic Phosphide	SOA	semiconductor optical amplifier
GRINSCH	graded index separate confinement heterostructure	SPM	self phase modulation
HSQ	Hydrogen silsesquioxane	TBP	time bandwidth product
InP	Indium Phosphide	TE	transverse electric
MLL	mode Locked Laser	TEC	thermoelectric controller
TLM	transfer length method	VRU	variable resolution unit

Symbol	Description	Symbol	Description
TM	transverse magnetic	*WDM*	wavelength division multiplexing
VI	voltage current		

Chapter 1

Introduction

1.1 Introduction

Semiconductor lasers are attractive sources for short optical pulse generation [1]. A wide range of schemes such as gain switching, Q-switching and mode locking have been applied to generate optical pulses in semiconductor lasers. Among these different techniques, mode locking is an efficient and widely used technique for generation of optical pulses in semiconductor lasers. Semiconductor mode locked lasers (SMLLs) are able to produce very short optical pulses with repetition rates up to several hundreds of GHz [2, 3]. Attractive features such as compact size, ease of integrability, direct electrical pumping and low cost makes the SMLLs superior to their solid-state and fiber counterparts [2]. SMLLs producing sub-picosecond pulses have a wide range of applications in future long haul high data rate optical communication systems [4], radio frequency (RF generation), remote sensing [5], spectroscopy [6], non-linear frequency conversion, optical sampling and signal processing [1]. To improve the systems performance and expand the range of applications, SMLLs with higher pulse energies, higher average and peak output powers are required [7]. In general, high power SMLLs are desirable since they reduce the need for optical amplification. The pioneering work on SMLLs started in early 1980's and despite two decades of active research, their performance is still limited in terms of the output powers as compared with their solid-

state and fiber counterparts, where average output power of a few Watts are readily achieved [8, 9]. However, the average output power obtained from single transverse mode, ridge waveguide SMLLs, operating at wavelength of ~ 1.55 μm are less than 20 mW [10]. Thus to increase the range of applications of SMLLs, a higher output power is desirable.

The research work presented in this thesis was partially supported by the Engineering and Physical Sciences Research Council (EPSRC) project "High Power, High Frequency Mode locked Semiconductor Lasers" running at the School of Engineering, University of Glasgow. The emission wavelengths under investigation in this EPSRC project for development of high power SMLLs were 1550 nm and 700-850 nm. The work presented in this thesis forms a part of this project, and is concerned with the development of high power SMLLs operating at 1.55 μm.

1.2 Focus of this Thesis

This thesis is mainly concerned with the design, fabrication and characterisation of high power SMLLs, with a repetition rate of around 40 GHz. The 1.55 μm wavelength range is of particular interest for optical fiber communications due to the minimum losses of optical fibers around this wavelength range [11]. The main aim of this research is to increase the relatively low output power (< 20 mW), typically generated by the SMLLs under the mode locking conditions. Due to the lack of fabrication complexity, the monolithically integrated master oscillator power amplifier (MOPA) configuration is used to increase the output power of the SMLLs. A single transverse mode semiconductor optical amplifier (SOA) is monolithically integrated at the output of the SMLL to boost the output power, while not affecting the mode locking performance of the device. The laser and the SOA sections of the device could be independently controlled and the bias conditions could be optimised for producing narrow pulse widths and higher output powers, simultaneously. Furthermore, the monolithically integrated device eliminates device-to-device coupling losses, reduces the package size and increases the device reliability. Distributed Bragg reflectors (DBRs) are used as intra-cavity reflectors to provide optical feedback in the laser cavity of the monolithically integrated SMLLs with SOAs. The effects of the integrated SOA on the output power, pulse duration, RF spectra and optical spectra are investigated. The SMLLs are also monolithically integrated with tapered-SOAs to obtain higher output power by taking advantage of the higher saturation

output power of the tapered SOAs. Improved heat sinking using Aluminium Nitride (*AlN*) sub-mounts and Gold Tin (*AuSn*) soldering is used for SMLLs integrated with tapered SOAs.

A wafer structure designed by the author's colleague Dr Lianping Hou, for high output power SMLLs is used for devices fabrication in this work. As will be detailed in Chapter 4 (Section 4.5), the epitaxial structure consists of three-quantum wells (QW) in the active region and a far-field reduction layer, which increases the mode spot size in the vertical direction. It will be shown that this improved waveguide design caused reduction in the internal losses, divergence angles and improved the output power of the devices. The performance of the devices based on the standard commercially available five-QW and novel three-QW active region materials are also investigated.

1.3 Summary of the main achievements

- Performance comparison of SMLLs based on commercially available five QW active region epitaxial material and optimized three QW active region epitaxial material with a far-field reduction layer.
- Design and fabrication of low loss, moderate reflectivity surface etched DBR gratings.
- Fabrication and characterisation of discrete SOAs with the waveguides tilted at 10° to the facets, achieving a saturation output power of ~ 15.8 dBm.
- Design, fabrication and characterisation of DBR-MLLs monolithically integrated with a narrow ridge waveguide SOAs.
- Design, fabrication and characterisation of DBR-MLLs monolithically integrated with tapered SOAs.
- Better heat sinking of SMLLs with integrated 2° tapered SOAs using *AlN* sub-mounts and *AuSn* soldering.
- Average output power of 130 mW, and peak output power of < 1W, from a 40 GHz passively mode locked laser with integrated narrow ridge waveguide SOA.
- Average output power of 200 mW, and peak output power of < 1.2W, from a 40 GHz passively mode locked laser with integrated 2° tapered SOA.
- Investigation of different integrated SOAs (narrow ridge waveguide, 2°tapered and 6° tapered) at the output of SMLLs.

1.4 Thesis contents

In this Chapter, the general introduction and the main focus of this research have been discussed. The majority of research work presented in this thesis is concerned with the design, fabrication and characterisation of high power SMLLs, operating at 1.55 μm.

Chapter 2 provides a brief overview of the optical communication systems, with a particular focus on the optical sources used in these systems. It is important for these sources to operate at high power to maintain high signal intensity during propagation. Design approaches to achieve high power SMLLs are thereby discussed. There are a number of other applications in which high power SMLLs are useful, and these are summarised.

Chapter 3 explains some of the basic background theory of SMLLs and SOAs. Different types of mode locking in the semiconductor lasers are explained, with a particular focus on the type considered in this work, i.e. passive mode locking. Methods to reduce facet back reflection of the SOAs are summarised, which is important to maximise the device performance. The basic characteristics of the SOAs such as optical spectra, optical gain and output power saturation are briefly discussed. The dynamic effects on pulse amplification in devices, including interband and intraband processes are given. And finally SMLLs integrated with DBRs are introduced.

Chapter 4 provides an introduction to QW lasers and the design of a novel epitaxial material used for fabrication of the devices in this work. The basic fabrication tools and processes used to fabricate devices are given. The material characterisation on the basis of ridge waveguide lasers analysis is presented. In order to assess the performance of the p-type ohmic contacts, the transfer length method (TLM) measurements results are also shown.

Chapter 5 presents a comparison of devices based on the three QW and five QW active region epitaxial structures. For these devices, the *L-I* curves, modal gain curves, simulated near-field, far-field, and measured far-field pattern are shown. The experimental set-up used for the characterisation of the devices and the mode locking performance of the devices based on the three QW and five QW active region epitaxial materials are compared.

The design, simulation results and experimental results of the surface-etched DBR gratings are also presented. Finally, results obtained from the SMLLs integrated with these DBRs are given.

Chapter 6 explains the measurement results of discrete SOA devices for a comparison. The simulation results for obtaining a low loss curved waveguide are given. The output power

measurements of the SMLLs monolithically integrated with single mode ridge waveguide SOAs, measured at both the SA and SOA facets are given and compared. The results of the far-field, measured at the SOA facet are given. The output peak power at different SOA currents is presented. The mode locking performance of the integrated device is investigated at the SA and SOA facets.

In Chapter 7, various heat sinking techniques of the semiconductor lasers are discussed. Improvements in heat sinking are obtained by mounting the devices on Aluminium Nitride (*AlN*) sub-mounts using eutectic Gold-Tin (*AuSn*) solder. The output power and the mode locking results of the SMLLs integrated with 2°-tapered SOAs, mounted on *AlN* sub-mounts using *AuSn* solder are presented. These devices were measured under CW current conditions. The effect of the integrated tapered SOA on the mode locking performance of the device is investigated. Output power measurements of the SMLLs integrated with 6°-tapered SOAs, measured under CW current conditions are discussed.

Chapter 8 discusses the conclusions and review of the work presented in this thesis. Some suggestions for future work as a follow up to this project are provided.

1.5 References

1.   D. J. Derickson, et al., *Short pulse generation using multisegment mode-locked semiconductor lasers.* IEEE Journal of Quantum Electronics, 1992. 28: p. 2186-2202.

2.   E. A. Avrutin, J. H. Marsh, and E. L. Portnoi, *Monolithic and multi-GigaHertz mode-locked semiconductor lasers: Constructions, experiments, models and applications.* IEE Proc. -Optoelectron. 2000. 147(4): p. 251-278.

3.   K. A. William, M. G. Thompson, and I. H. White, *Long-wavelength monolithic mode-locked diode lasers.* New Journal of Physics, 2004. 6(179): p. 1-30.

4.   K. Merghem, et al., *Short pulse generation using a passively mode-locked single AlGaAsP/InP quantum well laser.* Optics express, 2008. 16(14): p. 10675-10683.

5.   C. Latrasse, et al., *Low noise semiconductor lasers for remote sensing applications*, in *15th Coherent Laser Radar Conference*: Canada.

6.   D. J. Bradley and M. H. Holbrook, *Mode-Locked Semiconductor Lasers and their Spectroscopic Applications.* Philosophical Transactions. Royal. Society. Lond. A 1982. 307: p. 521-530.

7.   Jason J. Plant, J.T.G., ; Bien Chann,; Daniel J. Ripin,; Robin K. Huang,; Paul W. Juodawlkis,;, *250 mw, 1.5um monolithic passively mode-locked slab-coupled optical waveguide laser.* Optics letters, 2006. 31(2): p. 223-225.

8.   Andreas Schmitt-sody, et al., *High power hybrid mode-locked external cavity semiconductor laser using tapered amplifier with large tunability.* Research letter in Optics, 2008. Article ID-865092.

9.   P. Polynkin, et al., *All-fiber passively mode-locked laser oscillator at 1.5 μm with Watts-level average output power and high repetition rate* Optics Letters, 2006. 31(5): p. 592-594.

10.   K. Yvind, et al., *Low-jitter and high-power 40-GHz all-active mode-locked lasers.* IEEE Photonics Technology Letters 2004. 16: p. 975-977.

11.   T.Miya, et al., *"Ultimate low loss single mode fibre at1.55μm.* Electron Lett, 1979. 15(4): p. 106-108.

Chapter 2

Background

2.1 Introduction

In this chapter, a brief introduction of the telecommunication systems and different schemes to increase the transmission capacity of the optical links is discussed. The main applications of SMLLs are described. The issues related to achieving high output power in SMLLs and different approaches commonly used to obtain high power in SMLLs are also discussed.

2.2 Modern Optical Telecommunication Systems

Telecommunication can generally be described as the transmission of information from one point to another. In earlier times, telecommunications were based on fire signals, audio messages through coded drum beats etc. The need to communicate created interest towards the development of the communication systems and therefore rapid developments has been made. In the second half of the 20th century, the use of optical signal as the carrier wave was realised. As a keystone of the modern optical telecommunication, the first laser was demonstrated in 1960 [1]. In 1960s, many ideas for the laser transmitters using different modulation techniques including frequency modulation, phase modulation, intensity modulation, amplitude modulation and polarization modulation were developed. Unguided transmission systems in free space were also developed between 1960 and 1970 [2]. In 1966, the optical fiber was proposed as a suitable transmission medium [3]. A few years later, in 1970, low loss optical

fiber was demonstrated [4]. The backbone of almost all long-haul communication systems is now based on transmission of optical pulses over the optical fibers, generated by lasers. The main components used in the modern telecommunication systems are [2]:

- Optical sources.
- Means of modulating optical signals with the data to be transmitted.
- Transmission medium.
- Photodetectors.
- Amplification and signal processing to recover the signal.

The optical fibers are attractive choices as a transmission medium due to their low transmission losses (0.2 dB/km at 1.55 μm wavelength), low signal distortion and good mechanical characteristics [5]. Semiconductor lasers are attractive optical sources due to their compact size and low cost. In the future communication systems, special type of lasers such as SMLLs might have other functionalities as well. More details of this will be discussed in Section 2.3. The demand for transmission capacity in the telecommunication networks is continuously increasing with time. In order to increase the available transmission capacity of the current optical links, multiple access schemes are commonly used. The multiple access schemes are the optical time division multiplexing (OTDM), wavelength division multiplexing (WDM) and optical code division multiple access (OCDMA).

2.2.1   Wavelength Division Multiplexing

The concept of WDM was first proposed by O. DeLange in 1970 [6]. Conceptually, WDM is the same as frequency division multiplexing [7]. Typical WDM systems require optical transmitters, multiplexers, transmission media, de-multiplexers and receivers. The schematic of a typical WDM system is shown in Figure 2.1. A WDM system consists of a number of transmitters each one with a distinct wavelength and the output from different transmitters is combined onto one fiber by using an optical multiplexer. After travelling through the transmission medium, the signal is de-multiplexed into different channels and detected by the receivers. The number of wavelengths transmitted through the optical fiber determines the number of independent addresses.
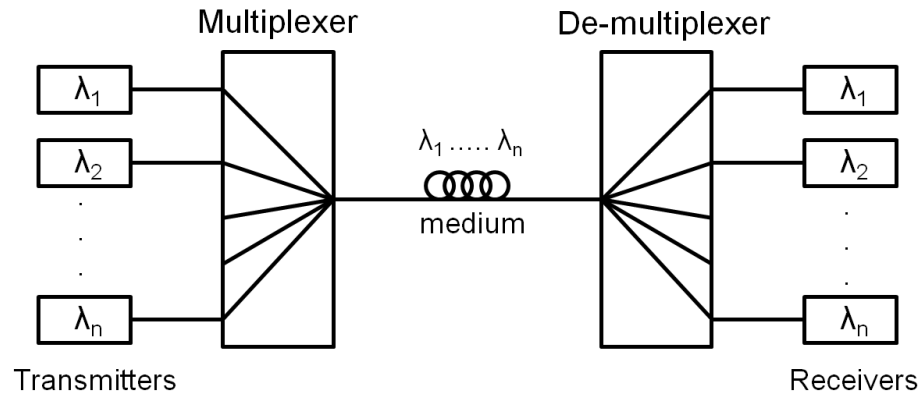
Figure 2.1: Schematic of a typical n-Channel WDM system [8].

Ideally, the different wavelengths in the transmission medium do not interfere with each other, however the noise in the systems arise when the wavelengths of the different channels overlap with each other. The noise due to the non-linear effects in the optical fibers degrades the overall performance of the system [9].

2.2.2   Optical Time Division Multiplexing

OTDM is a method of putting multiple data stream on a single signal by separating the signal into many parts in time domain such that each bit is assigned a discrete time slot. The schematic of a typical OTDM system is shown in Figure 2.2.
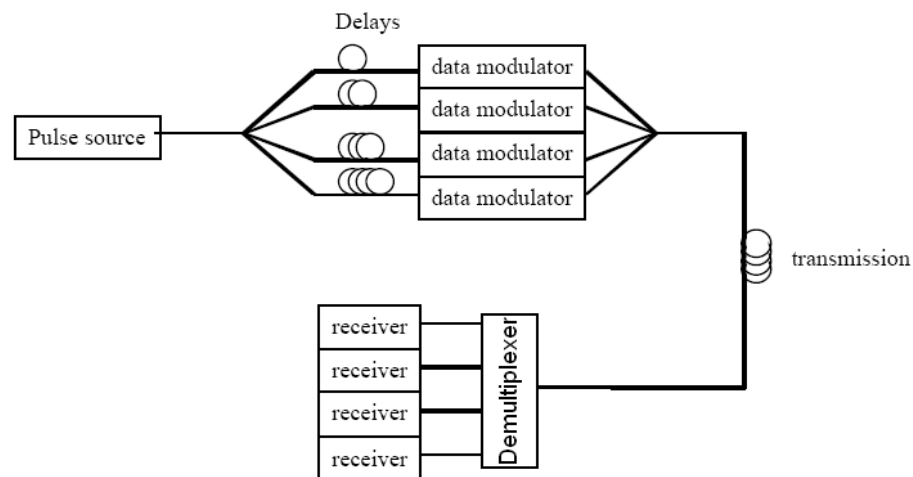
Figure 2.2: Schematic of a four channel OTDM system.

In OTDM systems, the short optical pulses generated by a laser are split in N-channels and each channel is delayed by a fraction of the bit period. [10]. If the pulses from the transmitter are emitted at repetition rate of X-GHz and the output is splitted into N-channels, then NxX

Gbit/s signal is formed at the output. The data is imposed on the optical signals through the modulators and the channels are then recombined to give a data stream. The data stream is transmitted in the optical fiber and then de-multiplexed. A timing clock is taken from the incoming signal and this extracted signal drives the de-multiplexers to recover the original channels.

2.2.3   Optical Code Division Multiple Access

OCDMA is an alternative multiplexing scheme to the WDM and OTDM schemes. OCDMA is very attractive for applications where privacy in the transmission important. OCDMA is realized by allocating each individual user one particular code which is assigned to the data pulses before the transmission. At the receiver end, each user requires correct decoding of the signal intended for them [11]. The main advantage of this scheme is unlike the two schemes already discussed, each user is allowed to use the entire available spectrum. The schematic of OCDMA is shown in Figure 2.3.
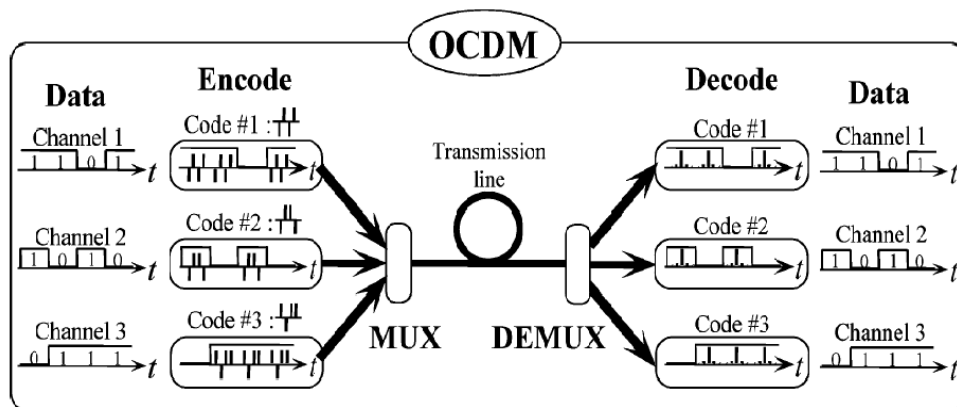
Figure 2.3: Schematic of a typical OCDMA system [12].

2.3 Light Sources for Telecommunications

Modern telecommunication systems require optical sources to transmit data from one place to another through optical fibers. The main light sources used for optical fiber communication systems are light emitting diodes (LEDs) and laser diodes The desired properties of the optical sources for use in telecommunication systems are high speed (bandwidth), high output power, higher optical coupling efficiency and directionality (output pattern). For optical communication systems requiring lower bit rates (<100-200 Mb/s), semiconductor LEDs are suitable light sources [7]. Most modern high speed optical telecommunication systems use

semiconductor lasers due to their higher modulation bandwidth, higher efficiency, narrow spectral width and wavelength stability. The first diode laser based on a Gallium Arsenide (GaAs) p-n junction, operating at a wavelength of 850 nm, transmitted data rates of up to 45 Mb/s [7, 13], with the repeater spacing of around 10 km, which was limited by the losses in the optical fibers. Due to the reason that optical fibers exhibit lower attenuation and dispersion at wavelength range of around 1300 nm and 1550 nm, semiconductor lasers operating in these wavelength ranges attracted the attention of researchers. The data stream can be transmitted through optical fibers by switching the laser output on and off i.e. through direct modulation of the lasers. However, the traditional direct current modulation techniques become un-efficient at higher frequencies (>10 GHz) thus limiting the transmission capacity. SMLLs generate modulated light at much higher frequencies (several hundred GHz) and are suitable pulse sources for a range of applications in optical communications and spectroscopy [14].

After the demonstration of first SMLL in 1978 [15], research has been dedicated to investigate the generation of high output power, short optical pulses from the SMLLs [16]. SMLLs combine advantages from ease of integrability and ultra-stable ultralow-noise performance to direct electrical pumping and compactness. The length of the cavity, position of the saturable absorber and the structural design of the SMLLs determine the repetition frequency and therefore, can be easily adjusted. In the long haul optical fiber communication systems, several repeaters may be needed between the source (transmitter) and the final target (receiver) to compensate for optical attenuation in the optical fibers. To reduce the system costs, high power SMLLs are required, which would increase the distance travelled by the optical pulse in the optical fibers before needing optical amplification. In general, high power SMLLs are desirable as they reduce the need for optical amplification and improve the optical signal to noise ratio. Applications of SMLLs shall be discussed in subsequent sections of this chapter.

2.4 Potential Applications of Semiconductor Mode locked Lasers

The small size, high stability, low cost and direct electrical pumping increases the range of applications of SMLLs. Moreover the ease of monolithic integrability of the SMLLs with other passive or active opto-electronic components such as modulators, multiplexers, filters and semiconductor optical amplifiers allow highly functional monolithically integrated photonic circuits. The potential applications of SMLLs are presented in the following sub-sections.

2.4.1   Optical Communication Systems

Perhaps one of the most important areas of applications of SMLLs generating short optical pulses is the future optical fiber communication, especially operating at wavelengths around 1.3 μm and 1.5 μm. SMLLs producing short optical pulses are used as pulse sources for WDM and OTDM systems [17]. To exploit the spectral properties of SMLLs, the output from these devices can be used as a multi-wavelength source in the WDM systems by using a narrow band spectral filtering to separate an individual locked longitudinal mode [18]. SMLLs are also suitable pulse sources for the OTDM systems due to their properties including short pulse generation, high pulse repetition rates and low noise performance. In OTDM systems, as mentioned earlier, the output of a SMLL operating at X-GHz repetition frequency is split into N-channels that are delayed, modulated and then recombined to form a NxX Gbit/s signal [19]. The de-multiplexing of high speed signals in the OTDM systems is more challenging because both the clock and data need to be recovered. SMLLs have been successfully demonstrated for all-optical clock recovery [20, 21]. SMLLs also have the potential to generate high quality millimetre-wave optical signals for fiber radio transmission which could be used for personal communication systems and distribution of signals for satellite antennas [22].

2.4.2   Non-Linear Optical Effects

Short optical pulses with high peak power generated by the SMLLs can be used to obtain non-linear effects. To obtain non-linear effects in non-linear media, very high optical intensities (~ 1 GW/cm^2) are required [23]. In order to get very high optical intensities, the optical pulses from SMLLs are focussed into small spots (~ 10 μm) by using a combination of lenses [24]. Second harmonic generation (SHG) is a common application of the non-linearities in which high intensity optical pulses interacting with non-linear material form photons with twice frequency and half wavelength of the initial photons. The second harmonic generation can be used to make ultraviolet, blue and green lasers [25]. SHG has also various applications in non-linear microscopy [26]. T. Yoda et al., reported high efficiency SHG by using externally amplified pulses at operating wavelength of 1550 nm [27].

2.4.3   Optical Sampling

A common way to characterise an optical data signal is using a photodetector and an oscilloscope. However, the overall bandwidth of the fastest available photodetector allows the measurement of data signals only down to several pico-seconds pulse duration. Changing the sampling process from electrical to optical domain would increase the bandwidth of the measurement process [28]. Sources producing short optical pulses are required for optical sampling. The temporal resolution of the optical sampling measurement is determined by the sampling pulse width and the timing jitter between the measured optical data pulses and sampling pulses. Thus, the pulse source used for sampling is the most important part of the measurement system [29]. The short optical pulses emitted from the SMLLs are attractive sources for optical sampling of other short events in time that could be optical, electrical, chemical or biological. Examples of optical sampling are analogue to digital converters (ADCs) for probing of ultrafast electrical signals and pump-probe measurement for probing a medium response to another more powerful signal [30]. The potential of short optical pulses emission at high repetition rate from the SMLLs make them the most suitable choice for sampling at higher sampling rates.

2.4.4   Terahertz Radiation Generation

The terahertz (THz) region of the electromagnetic spectrum is of interest due to its non-ionizing properties, higher resolution than microwave radiations and low absorption in many materials. The main applications of the THz signals include medical imaging, spectroscopy and security [31-33]. Semiconductor lasers are widely used for THz signal generation. THz radiation can be generated simply via a photomixer by heterodyning two continuous-wave (CW) single mode lasers with a wavelength difference corresponding to desired beat frequency [34]. THz radiation could be also generated by using short optical pulses from lasers. The optical pulses from the lasers are incident on a photoconductive emitter, electron and hole pairs are generated in the semiconductor material. The charge carriers are then accelerated by a bias voltage. The resulting transient photocurrent is proportional to this acceleration and radiates at THz frequencies [35]. Terahertz photoconductive switch based on InGaAs for the pump wavelength of 1.55 μm have been reported [36]. Nowadays, the development of ultrafast photoconductive emitters made it possible to produce practical power levels of THz radiation. Another approach to convert short optical pulses into THz radiation is

based on the emission of optical rectification inside a non-linear crystal. More details of this process are given in [35]. MLLs emitting high output power are required to generate THz radiation effectively and to get sufficient power in the THz components [24, 31].

2.5   High Power Operation of Semiconductor Mode Locked Lasers

As discussed earlier, SMLLs producing short optical pulses and high output powers have potential applications in the long haul high data rate optical communication systems, terahertz (THz) signals generation, radio frequency (RF) generation, non-linear frequency conversion, optical sampling, signal processing and optical measurements.[37, 38]. Conventional SMLLs although compact and in many cases cheaper than their solid state and fiber laser counterparts, produce low output powers to be used for some of the previously mentioned applications. To increase the range of applications of SMLLs, they should be designed to deliver high output power with narrow pulse widths and good beam quality. In the last two decades, there has been a great deal of research and substantial improvements have been achieved in high power operation of SMLLs at different operating wavelengths.

Output power in GaAs based single mode semiconductor lasers is limited by the facet degradation, which leads to catastrophic optical mirror damage (COMD) at high photon densities. The COMD mechanism can be described as; non-radiative recombination at the mirror facet releases thermal energy to the lattice which increases the local temperature. This induces band gap narrowing, which enhances absorption at the facet. The additional free carriers generated recombine non-radiatively and further increases the temperature of the mirror facets [39]. At extreme case, the facet melts and a catastrophic drop in the output power occurs. The COMD is a major problem for high power single mode devices at operating wavelength of < 1µm. However, InP based devices, such as those operating at 1.55 µm are less susceptible to COMD. The thermal conductivity of InP (0.68 WK^{-1}cm^{-1}) is higher than GaAs (0.44 WK^{-1}cm^{-1}), which is one of the reasons why the InP based devices do not readily suffer from COMD [40].

Typically, the output power from single mode lasers under the continuous wave (CW) current operation is higher than that in the mode locked operation. The output power of SMLLs increases with increasing the injection current. However, at a certain value of current and hence output power, the emitted pulses become temporally broader and chirped. A further

increase in injection current causes the mode locking to cease and switches the device operation regime to CW emission. The main reason for the difference in emitted CW and mode locked output power of SMLLs is the limitation on the pulse energy. Pulse formation in SMLLs is a balance between the pulse shortening and pulse broadening effects. This will be explained in more details in Chapter 3 (Section 3.4). Gain saturation in SMLLs, due to the amplification of large pulses causes time dependent variations in carrier density and hence refractive index, which leads to self-phase modulation (SPM). SPM broadens the optical pulses spectrally and temporally due to group velocity dispersion (GVD). Gain saturation and SPM induced pulse broadening in SMLLs increases significantly at pulse energies approaching the saturation energy, i.e. high injection currents. The pulse broadening in the gain section due to these effects supersedes the pulse shortening effects provided by SA section and hence prevents the mode locking. The saturation energy of the pulses in the MLLs is given by [37]:

$$E_{sat} = \frac{h\upsilon A}{\Gamma \, dg/_{dN}}$$

<div align="right">Equation 2.1</div>

where $h\upsilon$ is energy of photons, A is mode cross-sectional area, Γ is optical confinement factor and dg/dN is the differential gain.

Compared to passively MLLs, actively MLLs can produce higher pulse energies due to the pulse generation mechanism. As pulse formation in actively MLLs relies on the gain modulation, therefore pulses are not affected as much by gain saturation as in passively MLLs [41].

To allow high output power operation of passively MLLs, higher gain saturation energy (E_{sat}) is desirable. This reduces pulse broadening in the gain region. One way to increase the E_{sat} value is to reduce the optical overlap of the waveguide mode with the active region, i.e. maximize A/Γ. Another way to increase the E_{sat} is by decreasing the differential gain (dg/dN), which can be achieved by reducing the number of quantum wells in the active region of the epitaxial structure [42]. Other approaches used for improving the pulse energy limitation on output power of the MLLs include bowtie-shaped gain regions [43], arrayed laser structures [44], broad area lasers [45], flared waveguide lasers [46] and master oscillator power amplifiers (MOPAs) [47].

Arrayed lasers are based on evanescent field coupling between the adjacent waveguides. Single lobe emission results from overlap of radiation from the neighbouring emitters of the laser array. A narrow and coherent optical beam is emitted from the lasers array when there is a fixed phase relationship between the emitters. Passive mode locking of an array design at 40 GHz pulse repetition frequency with an average output power of 40 mW has been reported in [48].

Broad area lasers are also used to achieve high output power in mode locked operation. Standard broad area lasers suffer from filamentation and modal instabilities which results in poor beam quality [49].

Output power from SMLLs can also be increased by using a combination of narrow ridge waveguide structure and laterally tapered gain region. The tapered section of the waveguide increases the effective modal cross-sectional area, i.e. A/Γ which leads to higher saturation output powers. The narrow ridge waveguide section acts as saturable absorber and also mode filter to suppress the higher order transverse modes. Further, in these structures the saturation in the absorber section is enhanced due to the increase in effective modal cross-sectional area in the gain section. Using tapered gain and narrow saturable absorber design, an output peak power of 2.2 W from a 17 GHz quantum dot MLL with 360 fs wide pulses were obtained [50]. Another approach for getting higher output power from SMLLs is the master oscillator power amplifier (MOPA) configuration. The MOPA consists of a master oscillator (single mode laser) and a power amplifier (SOA) to increase the output power of the single mode laser. In MOPAs, the output emitted from the single mode lasers enters into the SOA section and get amplified as it travels inside the waveguide of the SOA. At the output facet of the SOA, an amplified signal is obtained at. In MOPAs, the master oscillators (laser) and power amplifiers (SOA) can be independently designed and biased to get required repetition rate, pulse width and power scaling. Further, the Monolithic integration of a laser and SOA eliminates the device to device coupling losses, reduces the package size and increases reliability. Due to the lack of fabrication complexity, the MOPA concept is the successful and effective configuration for achieving high output power from lasers. Single mode ridge waveguide SOAs as well as tapered SOAs can be integrated with a single mode laser to construct monolithically integrated master oscillator power amplifier (M-MOPA). In case of integration of a tapered SOA with a single mode laser, the optical mode gets amplified in the tapered waveguide and adiabatically expands as it propagates from the narrow facet towards the wide facet of the amplifier. The wide gain cross-sectional area at the output end of the tapered SOA

results in increased saturation output power of SOA and also further reduces facet back reflections. Further, tapered SOAs provide higher small-signal gain due to reduced gain depletion caused by the ASE noise, particularly at the narrow input end of the amplifier waveguide. High output powers together with better beam qualities have been demonstrated from MOPA devices at various wavelengths. R.Parke et al, reported on demonstration of single lobe diffraction limited CW output power of more than 1 W from monolithically integrated tapered amplifier MOPA [51]. The first mode locked operation of tapered amplifier MOPA was demonstrated by Alan Mar et al. achieving an average power of 296 mW at 940 nm wavelength [52]. Recently, average output power of 46.6 mW has been reported from a mode locked monolithic quantum dot master oscillator power amplifier, operating at 1300 nm wavelength [53].

There have been only a few reports on high output power SMLLs at operating wavelength of 1.5 μm. Generally, SMLLs operating near 1.5 μm wavelength have shorter upper-state lifetime than those operating below 1 μm. This shorter upper-state lifetime in devices operating at 1.5 μm wavelength limits the pulse energy [54]. Recently, passively mode locked slab-coupled optical waveguide lasers (SCOWLs) have demonstrated an average output power of 250 mW at repetition rate of 4.29 GHz, operating at wavelength of 1.5 μm. In SCOWL devices, due to the reduction of optical modal overlap with active region i.e. increased A/Γ, gain saturation energies can be scaled up to 30-100 pJ [54]. However, the SCOWL concept does not scale well to high repetition rates because the ultra low optical confinement factor ($\Gamma \sim 0.3\%$) requires longer cavities. Devices based on SCOWLs also typically require current > 1A. Furthermore, SCOWL based devices require etching through the active core of the epitaxial material leading to increased fabrication complexity and associated problems with exposure of the active region to air, which is of particular importance for Aluminium containing active regions.

In this work, the MOPA concept is used for improving the output power of SMLLs. The SMLLs are monolithically integrated with single transverse mode narrow ridge waveguide SOAs and tapered SOAs of different taper angles. The effect of the integrated SOA on the output power and the mode locking performance of these devices are investigated. These devices are based on a novel epitaxial structure with increased A/Γ, which will be described in Chapter 4 (Section 4.5). According to Equation 2.1, this epitaxial material will result in an increased E_{sat}, which will reduce the pulse broadening in the gain section and thus allow high output power operation of SMLLs.

2.6 Chapter Summary

This chapter presented a brief introduction of the modern telecommunication systems and the optical sources used in these systems. High power SMLLs were described to be attractive sources, especially for future telecommunication systems. Applications and different commonly used approaches for achieving high output power in SMLLs were discussed. The MOPA approach was used in this research work to realize high power SMLLs. The devices in this work were based on a novel epitaxial material with higher E_{sat}, which allow higher output power operation of the devices.

2.7 References

1.   T. H. Maiman, *Stimulated Optical Radiation in Ruby.* Nature, 1960. 187: p. 493-494.

2.   John Gowar, *Optical Communication Systems*. 1984, London: Prentice-Hall.

3.   K.C.Kao, G.A.H., *Dielectric-fibre surface waveguides for optical frequencies.* Proceedings of the IEEE. 1966. 113: p. 1151-1158.

4.   F. P. Kapron, D. B. Keck, and R. D. Maurer, *Radiation losses in glass optical waveguides,.* Applied Physics Letters. 1970. 17: p. 423-.

5.   Riccardo Scollo, *Mode-locked InP based laser diode with a monolithic integrated UTC-absorber for sub-ps pulse generation*. 2009, Swiss Federal institute of Technology: Zurich.

6.   O. DeLange, *Wide-band optical communication systems: Part II Frequency -division multiplexing.* Proceedings of the IEEE. 1970. 58(10): p. 1683-1690.

7.   Gerd Keiser, *Optical Fiber Communication*. 3rd edition.

8.   Anthony E Kelly, *Optimisation of Semiconductor Optical Amplifiers for Optical Networks*. 1999, University of Strathclyde: Glasgow.

9.   A. Singh, A. K. Sharma, and T. S. Kamal, *Four-wave mixing analysis in WDM optical communication systems with high order dispersion.* Optik 2008. 119: p. 788-792.

10.   Jian-Guo Zhang and A. B. Sharma, *High-speed Optical time Division Multiple Access (OTDMA) Networks using Optical Signal Processing.* Photonic Network Communication, 1999. 1(4): p. 273-285.

11.   Nikos Karafolas, D.U., *Optical fiber code division multiple access networks: A review.* Optical fiber technology, 1996. 2: p. 149-168.

12.   H. Sotobayashi, W. Chujo, and K. Kitayama, *Highly spectral efficient optical code-division multiplexing systems.* IEEE Journal of Quantum electronics. 2004. 10(2): p. 250-258.

13.   R. J. Sanferrare, *Terrestial lightwave system.* AT+T Tech. J. 66(1): p. 95-107.

14.   E. A. Avrutin, John H. Marsh, and E. L. Portnoi, *Monolithic and multi-GigaHertz mode-locked semiconductor lasers: Constructions, experiments, models and applications.* IEE Proc. -Optoelectron. 2000. 147(4): p. 251-278.

15.   P. T. Ho, et al., *Picosecond pulse generation with cw GaAlAs laser diode.* Applied Physics Letters. 1978. 33: p. 241-243.

16.   Leaf A. Jiang, Erich P. Ippen, and Hiroyuki Yokoyama, *semiconductor mode-locked lasers as pulse sources for high bit rate data transmission.* Journal of optical fiber communication reports, 2005. 2: p. 1-33.

17.   Masataka Nakazawa, *Solitons for Breaking Barriers to Terabit/Second WDM and OTDM Transmission in the Next Millennium.* IEEE Journal of Selected Topics in Quantum Electronics, 2000. 6(6): p. 1332-1343.

18.   Y. K. Chen, et al., *Multicolor single-wavelength sources generated by a monolithic colliding pulse mode-locked quantum well laser.* IEEE Photonics Technology Letters, 1991. 3(11): p. 971-973.

19.   Krestin Yvind, *Semiconductor mode-locked lasers for optical communication systems*, in Technical University of Denmark.

20.   B. K. Mathason and P. J. Delfyett, *Pulsed Injection Locking Dynamics of Passively Mode-Locked External-Cavity Semiconductor Laser Systems for All-Optical Clock Recovery.* Journal of Lightwave Technology, 2000. 18(8): p. 1111-1120.

21.   K. Smith and J. K. Lucek, *All-optical clock recovery using a mode-locked laser.* Electronics Letters, 1992. 28(19): p. 1814-1816.

22.   D. Novak, C. Lim, and H. F. Liu, *Optimization of Millimeter-Wave Signal Generation Using Multi-Electrode Semiconductor Lasers with Subharmonic Electrical Injection.* International Topical Meeting in Microwave Photonics, Japan, 1996: p. 85-88.

23.   Ricardo Elgul Samad, et al., *Ultrashort Laser Pulses Applications*, Instituto de Pesquisas Energéticas e Nucleares – IPEN-CNEN/SP: Brazil.

24.   Giuseppe Tandoi, *Monolithic High Power Mode Locked GaAs/AlGaAs Quantum Well Lasers*, in School of Engineering. 2011, University of Glasgow.

25.   Available   Online   http://www.rp-photonics.com/frequency_doubling.html,   *last accessed: 10 Janurary 2011*.

26.   Both M, et al., *Second harmonic imaging of intrinsic signals in muscle fibers in situ.* J. Biomed Opt., 2004. 9(5): p. 882-892.

27.   T. Yoda, et al., *High peak power picosecond optical-pulse generation with a gain switched semiconductor laser, and high efficiency wavelenght conversion.* Conference on Lasers and Electro-Optics, CLEO/Pacific Rim, 2005: p. 1606-1607.

28.   Carsten Schmidt-Langhorst and Hans-Georg Weber, *Optical sampling techniques.* J. Opt. Fiber. Commun. Rep. 2, 2005: p. 86-114.

29.   Masayuki Shirane, Y.H., Hirohito Yamada, Hiroyuki Yokoyama, *A Compact Optical Sampling Measurement System Using Mode-Locked Laser-Diode Modules.* IEEE Photonics Technology Letters, 2000. 12(11): p. 1537-1539.

30.   David Larsson, *Fabrication and characterization of low-noise monolithic mode-locked lasers*, in Technical University of Denmark. 2006.

31.   J. Zhang, et al., *Terahertz pulse generation and detection with LT-GaAs photoconductive antenna.* Optoelectronics IEEE Proceedings, 2004. 151(2): p. 98-101.

32.   M. Hangyo, T. Nagashima, and S. Nahima, *Spectroscopy by pulsed terahertz radiation.* Meas. Sci. Technol., 2002. 13: p. 1727-1738.

33.   B. B. Hu and M. C. Nuss, *Imaging with terahertz waves.* Optics Letters, 1995. 20: p. 1716-1718.

34.   M. D. Pelusi, et al., *THz optical beat frequency generation from a single mode locked semiconductor laser.* Applied Physics Letters, 1997. 71.

35.   Dan Andreyevitch Yanson, *GENERATION OF TERAHERTZ-MODULATED OPTICAL SIGNALS USING AlGaAs/GaAs LASER DIODES*, in Faculty of Engineering,. 2003, University of Glasgow.

36.   Kimani K. Williams, et al., *Toward a 1550 nm InGaAs photoconductive switch for terahertz generation.* Optics Letters, 2009. 34(20): p. 3068-3070.

37.   D. J. Derickson, et al., *Short pulse generation using multisegment modelocked semiconductor lasers,.* IEEE Journal of Quantum Electronics, 1992. 28: p. 2186-2202.

38.   Jason J. Plant, et al., *250 mW, 1.5 μm monolithic passively mode-locked slab-coupled optical waveguide laser.* Optics Letters, 2006. 31(2): p. 223-225.

39.   Guiseppe Tandoi, *Monolithic High Power Mode Locked GaAs/AlGaAs Quantum Well Lasers*, in School of Engineering. 2011, University of Glasgow, Glasgow.

40.   Lock, D., S.J. Sweeney., and A.R. Adams. *Wavelength dependence of catastrophic optical damage threshold in 980 nm semiconductor diode lasers.* in *Lasers and Electro-Optics Society, 2003. LEOS 2003. The 16th Annual Meeting of the IEEE*. 2003.

41.   Alan Mar, *High Power Mode-Locked Semiconductor Lasers, PhD Thesis*, in Department of Electrical and Computer Engineering. 1994, University of California, Santa Barbara.

42.   Lianping Hou, et al., *Low divergence angle and low jitter 40 GHz AlGaInAs/InP 1.55 μm mode-locked lasers.* Optics Letters 2011. 36: p. 966-968.

43.   S. Gee, et al., *High power mode-locked external cavity semiconductor laser using inverse bow-tie semiconductor optical amplifiers.* IEEE Journal of Selected Topics in Quantum Electronics, 1998. 4(2): p. 209-215.

44.   A. Mar, et al., *Mode-locked multisegment resonant-optical-waveguide diode laser arrays.* IEEE Photonics Technology Letters, 1993. 5(12): p. 1355-1359.

45.   Kaiser, J., et al., *Mode-locking in broad-area semiconductor lasers enhanced by picosecond-pulse injection.* IEEE Journal of Selected Topics in Quantum Electronics, 2004. 10(5): p. 968-973.

46.   D. I. Nikitichev, et al., *High-power passively mode-locked tapered InAs/GaAs quantum-dot lasers.* Applied Physics B: Lasers and Optics. 103(3): p. 609-613.

47.   Thorsten Ulm, et al., *InGaAs diode laser system generating pulses of 580 fs duration and 366 W peak power.* Applied Physics B: Lasers and Optics, 2008. 92(4): p. 481-485.

48.   Zarrabi, J.H., E.L. Portnoi, and A.V. Chelnokov, *"Passive mode locking of a multistripe single quantum well GaAs laser diode with an intracavity saturable absorber,".* Applied Physics Letters, 1991. 59(13): p. 1526-1528.

49.   J. Martı́n-Regalado, et al., *Mode control and pattern stabilization in broad-area lasers by optical feedback.* Physical Review A, 1996. 54(6): p. 5386-5393.

50.   I. H. White, et al., *Ultra-short Optical Pulse Generation by InGaAs Quantum-Dot Diode Emitters.* In 22nd IEEE International Semiconductor Laser Conference (ISLC), 2010, p. 168-169.

51.   R.Parke, et al., *2.0 W CW, diffraction-limited operation of a monolithically integrated master oscillator power amplifier,.* IEEE Photonics Technology Letters, 1993. 5: p. 297-300.

52.   A. Mar, et al., *Mode-locked operation of a master oscillator power amplifier"* IEEE Photonics Technology Letters, 1994. 6(9).

53.   V. F. Olle, et al., *20 GHz Picosecond Pulse Generation by a 1300nm Mode-Locked Quantum Dot Master Oscillator Power Amplifier*, in OFC. 2009.

54.   Jason J. Plant, et al., *250 mW, 1.5 μm monolithic passively mode-locked slab-coupled optical waveguide laser* Optics Letters, 2006. 31(2): p. 223-225.

Chapter 3

Device Background Theory

3.1   Introduction

This chapter begins with a brief introduction to semiconductor lasers. Different schemes for emission of optical pulses from semiconductor lasers are introduced with emphasis on mode locking. Mode locking is introduced as a widely used method for sub pico-second optical pulse generation. The conditions for mode locking and different phenomena related to pulse shortening and broadening in semiconductor mode locked lasers (MLLs) is detailed in Section 3.2.1. This is followed by the basic background theory, operating principles and important characteristics of semiconductor optical amplifiers (SOAs). Various schemes for reducing the output facet reflectivity of SOAs are presented. Optical gain of SOAs and its dependence on input power and injection current are discussed, which is followed by a brief discussion of saturation output power in SOAs. The inter-band and intra-band processes which determine the amplification of the optical pulses and the gain variations after propagation of optical pulses are described in Section 3.10. Finally, MLLs integrated with distributed Bragg reflectors are briefly discussed.

3.2   Semiconductor Lasers

Semiconductor lasers are used in several different applications, such as consumer electronics, medicine, industry, entertainment and military. Comparing to the other types of lasers,

semiconductor lasers are attractive due to their compact size, direct electrical pumping, high efficiency and low cost. Since the invention of the first semiconductor laser in 1962, huge research has been done to improve the performance of these devices [1]. These devices can emit light in a wide spectral range spanning from the near ultraviolet to the far infrared. The wavelength of the emitted light depends on the material system implemented for such devices. Semiconductor lasers emitting at around 1.3 μm or 1.5 μm are attractive sources for optical fiber communication systems. The most commonly used semiconductor laser material systems include GaAs/AlGaAs, InGaAsP/GaInAs/InP and InGaAs/AlGaInAs/InP [2].

In semiconductor lasers, electrons and holes are injected into the active region through electrical pumping, which introduces population inversion and produces optical gain. If the injected carrier density is large enough, the stimulated emission of the photons overcomes the losses and the laser achieves gain. More details on the operation of semiconductor lasers are given in Chapter 4 (Section 4.2). Mostly, semiconductor lasers are based on double heterostructure materials due to their improved carrier and optical confinement as compared to homojunction materials.

In general, semiconductor lasers can be classified into two groups, gain guided and index guided lasers [3]. In the gain guided lasers, the current is injected into a narrow strip along the cavity length, thus laterally limiting the width of the optical gain region. In the index guided lasers, a region of relatively higher refractive index provides optical mode confinement. The index guided lasers are further classified into two sub-groups, strongly index guided and weakly index guided lasers. In strongly index guided lasers, a ridge is etched through the core of the material and a material of lower refractive index is overgrown in a second epitaxial growth step. In the weakly index guided lasers, the discontinuity in the effective index is obtained by non-uniform cladding layers. A typical example of this type of lasers is the ridge waveguide laser. In such devices, the effective index step is obtained by etching the semiconductor material above the active layer, as shown in Figure 3.1.
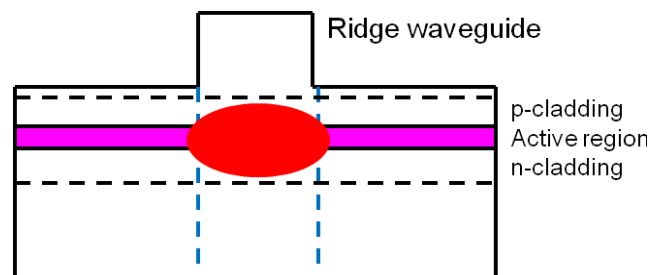
Figure 3.1: Schematic of the waveguide structure of a ridge waveguide laser.

The effective refractive index difference of the etched and the non-etched areas of the material provide horizontal optical confinement, while the index difference between the core and the cladding layers provides vertical optical confinement. The mode guiding mechanism in such lasers is partially gain guiding and partially index guiding. In this work, ridge waveguide lasers were used due to the ease of fabrication.

3.3   Pulse Generation in Semiconductor Lasers

As discussed in Chapter 2, optical pulses emitted from the semiconductor lasers have applications in optical fiber communication systems, radio over fiber communications systems, terahertz signals generation and fast optical sampling oscilloscopes. Since the development of the first laser, the generation of optical pulses in semiconductor lasers has been of interest. Semiconductor lasers exhibit wide gain bandwidth and short carrier lifetimes. In addition, features such as electrical pumping, compact size, ease of fabrication and long lifetime makes them attractive for being used as pulse sources. The basic idea of pulse emission from semiconductor lasers is based on the introduction of short periods of net gain or loss. Generally, three methods are applied to semiconductor lasers to generate optical pulses i.e. gain switching, Q-switching and mode locking. Among these techniques, the mode locking technique results in shorter and higher quality optical pulses [4]. The next section provides some basic theory related to the mode locking concept.

3.3.1   Mode Locking

Mode locking is a common method for producing short pulses in semiconductor lasers. This method is based on the introduction of a fixed phase relationship between the longitudinal modes of the laser cavity. Many research groups have investigated semiconductor mode locked lasers (SMLLs) soon after the first demonstration of 20 ps pulses from an AlGaAs laser diode [5]. In Fabry-Perot lasers, the standing waves in the laser cavity form longitudinal modes. The condition for oscillation of a wavelength in the laser cavity is:

$$k\lambda = 2nL$$

where k is an integer, λ is the wavelength of light, n is the effective refractive index of the guided mode and L is the length of the laser cavity.

The mode spacing between the adjacent longitudinal modes in the wavelength domain is:

$$\Delta\lambda = \frac{\lambda^2}{2n_g L}$$

Equation 3.1

where n_g is the group refractive index: $n_g = n - \lambda\, dn/d\lambda$.
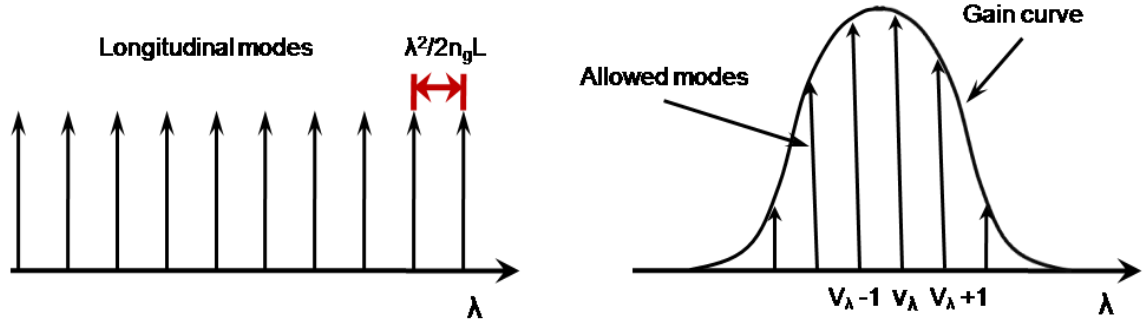
Figure 3.2: Graphical representation of (Left) longitudinal modes (Right) Gain curve of FP-laser [6].

The laser emits several longitudinal modes, the number of which depends on spectral bandwidth of the laser. The electric field of the laser output is the superposition of the electric field of the individual oscillating modes and is given by [4, 7]:

$$E_t = \sum_{n=0}^{N-1} A_n e^{[i(\omega_n t + \delta_n)]}$$

Equation 3.2

where A_n, ω_n and δ_n are the amplitude, angular frequency and phase of the nth mode, respectively.

If the cavity modes are incoherent (i.e. out of phase), the laser emits a constant wave (CW) mean output power. Then the total irradiance is the sum of the irradiances of the individual modes.

$$I = NA_n^2$$

Equation 3.3

If the modes are forced to maintain a fixed relative phase (δ) relationship with respect to each other, i.e. $\delta n = \delta$, the modes are phased locked and the light output becomes periodic in time. The total irradiance must then be found by adding the individual electric fields. Equation 3.2 can thus be written as:

$$E_t = A_n e^{(i\delta)} \sum_{n=0}^{N-1} e^{(i\omega_n t)}$$

Equation 3.4
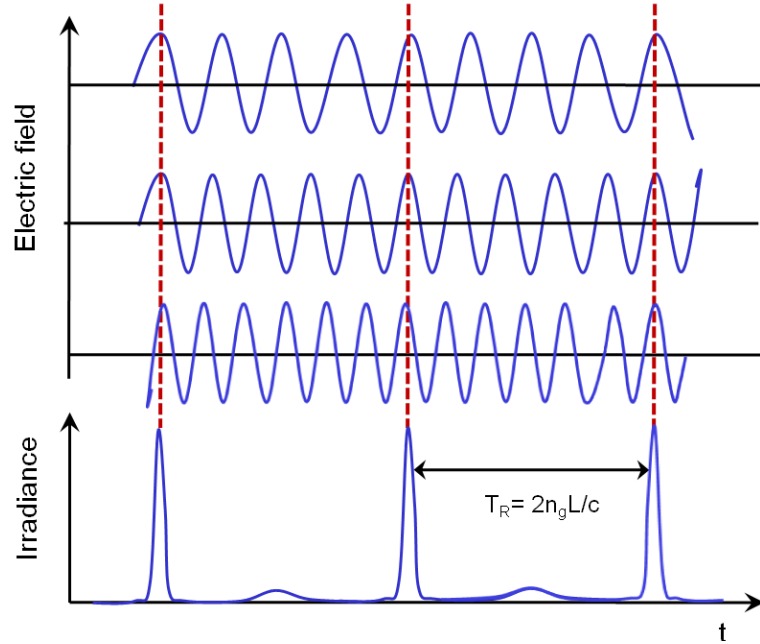
Figure 3.3: Schematic showing mode locked laser output [7].

The angular frequency ω_n can be written as $\omega_n = \omega - n\delta\omega$, where ω is the angular frequency of the highest frequency mode, $\delta\omega$ is the angular frequency separation between modes and n is the number of the mode.

$$E_t = A_n e^{(i\delta)} \sum_{n=0}^{N-1} e^{[i(\omega - n\delta\omega)t]}$$

This can be re-written as:

$$E_t = A_n e^{[i(\omega t + \delta)]} \sum_{n=0}^{N-1} e^{-in\delta\omega t}$$

$$E_t = A_n e^{[i(\omega t + \delta)]} (1 + e^{-i\delta\omega t} + e^{-2i\delta\omega t} + \ldots\ldots\ldots + e^{-(N-1)i\delta\omega t}$$

The second term in this equation is a geometric progression, it reduces to

$$E_t = A_n e^{[i(\omega t + \delta)]} \frac{sin\left(\frac{N\delta\omega t}{2}\right)}{sin\left(\frac{\delta\omega t}{2}\right)}$$

Equation 3.5

Equation 3.5 gives the electric field of mode locked modes. The total irradiance $I_{(t)}$ is given by:

$$I_t = E_{(t)}E_{(t)}^* = A_n^2 \frac{sin^2\left(\frac{N\delta\omega t}{2}\right)}{sin^2\left(\frac{\delta\omega t}{2}\right)}$$

<div align="right">*Equation 3.6*</div>

where N is the number of locked modes. From Equation 3.6 it is clear that the total irradiance $I_{(t)}$ is periodic (2π) with periodicity T_R, which equals to cavity round trip time. The shape of emitted light pulses in time domain are influenced by amplitude distribution (A_n) and phase distribution of the modes. The number of locked modes (N) is given by the ratio between the cavity round trip time (T) and the pulse width (Δt) [4]. Pulse width is inversely related to the spectral bandwidth of the laser and depends on the number of modes locked (N). Thus to get short output pulses, a large number of locked modes is required. Different techniques can be used to enforce a fixed phase relationship between different modes. These will be discussed in the next section.

3.4 Types of Mode Locking

Generally, three techniques are used for achieving mode locking in semiconductor lasers: active mode locking, passive mode locking and hybrid mode locking. Each of these techniques are briefly described in the following sub-sections. Since this research work involves only passive mode locking, the main focus of the discussion will be on passive mode locking.

3.4.1   Active Mode Locking

Active mode locking in semiconductor lasers is achieved by modulating the loss or gain of the laser at a frequency corresponding to the repetition rate of the pulses. Lower losses or higher gain in short periods of time concentrate the output energy of the laser in same periods. Electro-optic or acousto-optic modulators can be used as shutters to modulate the losses and hence establish a constant phase relationship between the longitudinal modes of the cavity [7]. Radio frequency (RF) current modulation can also be used to achieve mode locking in the semiconductor lasers. The current modulation causes carrier density modulation around the threshold value of the carrier density. The conditions for current modulation are chosen in order to provide a short window for the net gain, i.e. carrier density exceeds its threshold value for short time duration during each modulation period.
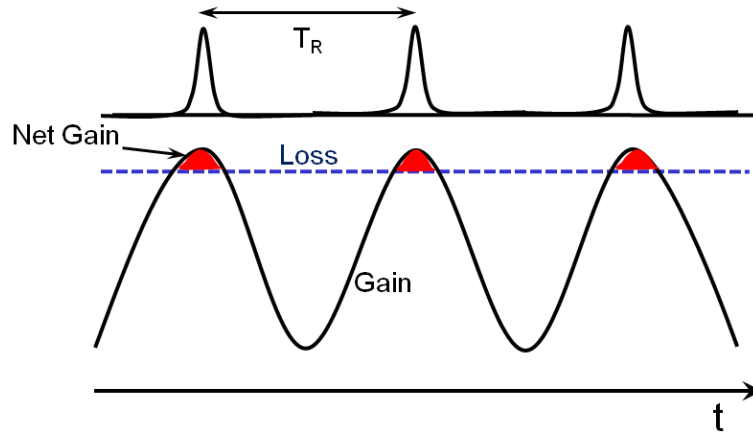
Figure 3.4: Schematic of pulse formation in time domain in the active mode locked lasers. The time window indicated by red colour represents the time duration when the device is in net gain.

This results in short optical pulses with a constant phase relationship as shown in Figure 3.4. The period of modulation should be equal to the cavity round trip time. The frequency of the output optical pulses is equal to the frequency of driving current [4].

3.4.2   Passive Mode Locking

Passive mode locking does not need any external signal for modulating the gain or loss of the laser. Passive mode locking takes place by incorporating an intra-cavity intensity dependent loss element. In quantum well (QW) lasers, a saturable absorber (SA) is typically placed in the cavity close to one of the facets, to act as the intensity dependent loss element. The SA section is made of the same semiconductor material as the gain section and hence the same band gap. However, the SA absorbs the photons generated in the active region of the lasers, which causes transition of electrons from the valence band (VB) to the conduction band (CB). When the excited electrons fill the CB and the holes VB, further transitions of electrons from the VB to CB are prevented. At this point, the SA is fully saturated and the absorber band edge is pushed towards the short wavelength end of the spectrum (blue shifted). Figure 3.5 shows the absorption versus incident light irradiance of a typical saturable absorber. In monolithically integrated passively mode locked QW lasers, the mechanism of growth of mode locked pulses is described as follows. Initially, the active medium of the lasers provides spontaneous emission characterised by incoherent fluctuations of intensity in the laser cavity. The fluctuations with higher intensity will then experience less absorption in the SA and will be partially transmitted by the SA, due to its intensity dependent transmission properties, as

shown in Figure 3.5. On the other end, the low intensity portions of the high intensity spikes are strongly attenuated. As the light in the cavity oscillates, this process repeats and narrower and higher intensity optical pulses are formed in the cavity [7, 8].
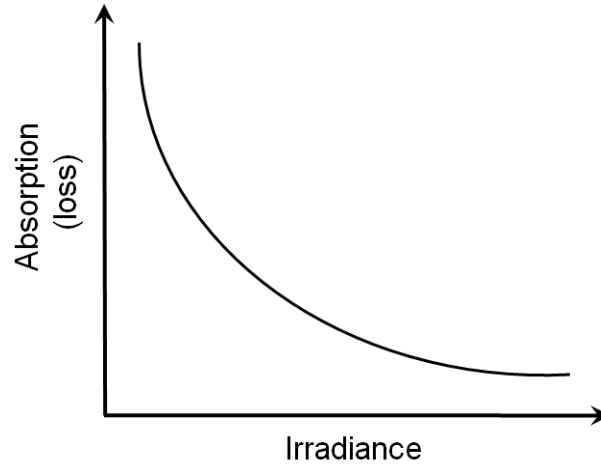
Figure 3.5: Schematic showing Absorption versus incident light Irradiance behaviour of a saturable absorber [7].

In the SMLLs, loss and gain approach their steady state conditions before the arrival of an optical pulse. As shown in Figure 3.6, in the steady state conditions, the loss (indicated by the red line) is larger than the gain (indicated by the blue line).
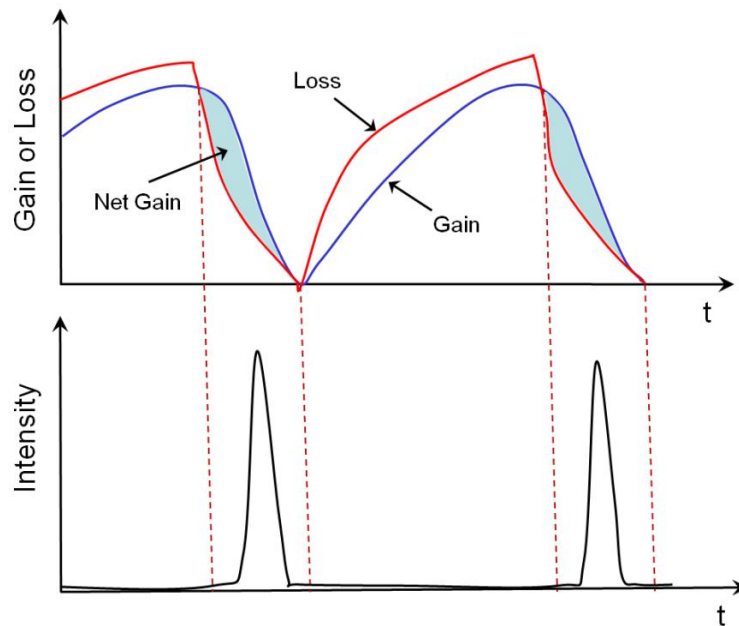
Figure 3.6: Schematic showing gain and loss dynamics of the passive mode locking.

Due to larger losses, the leading edge of the pulse experiences losses and saturate the SA. In saturated conditions, the central part (high intensity) of the pulse is transmitted, whereas the trailing edge of the pulse again experiences loss due to the recovery of the SA. If the value of loss remains greater than gain everywhere except near the peak of the pulse, spontaneous emission will not be able to build up between the emitted pulses [4]. The interplay between the non-linear gain, non-linear loss and the carrier lifetime creates a short time window of net gain, as shown in Figure 3.6. The net gain window results in the formation and shaping of optical pulses. SMLLs need to be designed to provide the net gain window as short as possible.

3.4.2.1   Conditions for Passive Mode Locking

A set of conditions must be satisfied for the formation of net gain window and amplification of the pulses in SMLLs. These conditions are as follows [8]:

(1)   The total energy of the pulse in the cavity must be larger than the total energy required for the SA saturation. The optical pulse should be able to fully saturate the SA in every round trip of the cavity.

(2)   The losses in the SA need to saturate with less pulse energy than that of the gain section, i.e. the saturation of the absorber E_{abs}^{sat} should be less than that of the gain section E_g^{sat}.

$$E_g^{sat} > E_{abs}^{sat}$$

or

$$\frac{hfA_g}{dg/dN} > \frac{hfA_\alpha}{dg/dN}$$

where *h* is the Plank constant, *f* is the frequency of light, A_g and A_α are the optical mode cross-sectional area in the gain and absorber section, respectively, and *dg/dN* is the differential gain in these sections.

In QW materials, there is non-linear dependence of gain on carrier density due to the step-like density of states. In monolithic mode locked lasers with a short SA section, the differential gain in the SA section is larger than that in the gain section [8]. Thus, the second condition of mode locking for QW mode locked lasers is always satisfied.

(3)   The recovery time of the absorber (τ_{abs}) should be less than that of the gain (τ_g), i.e. absorber should recover faster than the gain section [9]:

$$\tau_g > \tau_{abs}$$

where τ is the recovery time of the carrier.

This condition imposes that the loss should remain greater than the gain everywhere except the net gain window. The fast recovery of loss will stop the stimulated emission on the trailing edge of the pulse. The QW saturable absorbers have recovery time >50 ps, which is long comparing to the cavity round trip time (which is of order of several ps). In order to satisfy the third condition of mode locking (faster recovery of SA), several techniques such as proton bombardment, ion implantation and split-contacts techniques are commonly used [8]. In this work, the split-contacts technique was used to reduce the absorber recovery time. The p-contact of the semiconductor laser was then split into two sections, i.e. gain section and SA section (this is normally 2-4% of the cavity length) as shown in Figure 3.7 (left). For passive mode locking operation, the gain is forward biased, while the SA is reverse biased. The absorption recovery times in reverse biased AlGaInAs QW material was measured using the pump-probe method by a colleague Richard P. Green, and the results are shown in Figure 3.7 (right) [10].
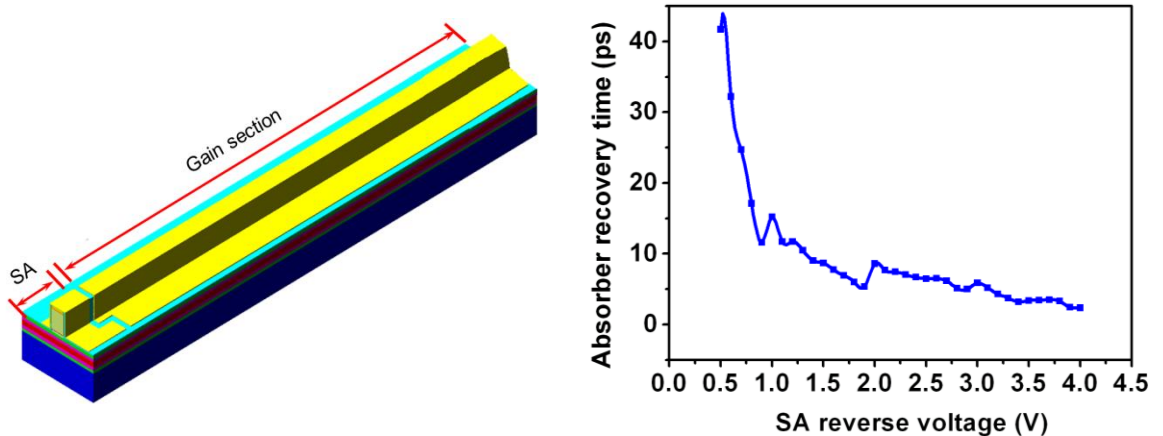
Figure 3.7: (Left) Schematic of a MLL and (right) measured absorption recovery time of AlInGaAs as a function of SA reverse voltage [10].

Figure 3.7 shows that absorber recovery times were below 5 ps for SA reverse bias of above 3 V. Absorption recovery time was lowest (2.5 ps) at 4 V SA reverse voltage. The carrier recovery time of the SA strongly effects the stability and pulse quality of mode locked lasers [11].

3.4.2.2   Saturable Absorber Dynamics

To properly investigate the mode locking regimes and short pulse generation in SMLLs, the interplay between the recovery time of SA, and non-linear saturation in both gain and absorber sections play a fundamental role [11, 12].
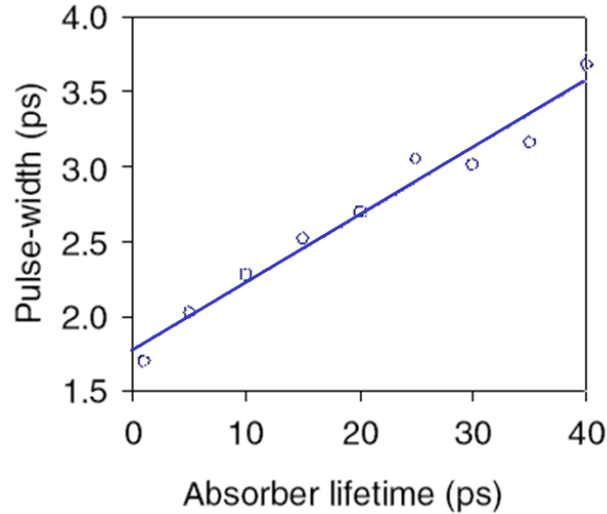
Figure 3.8: Plot showing the dependence of pulse duration on the SA lifetime [12].

From Figure 3.8, it is clear that the pulse duration decreases with decreasing carrier lifetime in the SA section. The pulse circulating in the laser cavity is continuously re-shaped due to the combination of pulse shortening and pulse broadening mechanisms in the gain and absorber sections of the laser. As explained in the previous section, the pulse shortening is due to time dependent gain and loss. The net gain window contributes to the pulse shortening in the laser cavity. Fast non-linearities such as spectral hole burning (SHB) and dynamic carrier heating also plays an important role in mode locking performance and pulse properties of the mode locked lasers [12, 13]. When the pulse width of a laser is larger than 1 ps, the gain and the absorber dynamics are mainly related to total carrier density [12]. However, when the pulse width inside the laser is less than 1 ps, ultra-fast carrier dynamics contribute to pulse broadening. These ultra fast non-linearities are due to dynamic deviation of energy distribution of holes and electrons [13]. These effects are briefly discussed in Section 3.10. Moreover, these ultra-fast non-linearities of gain and absorption will be accompanied by fast refractive index non-linearities adding a fast component to the slow self phase modulation (SPM), which is caused by changes in carrier density [13].

3.4.3   Hybrid Mode Locking

As the name suggests, hybrid mode locking is the combination of both active and passive mode locking. In this scheme, short optical pulses are produced in the same way as in passive mode locked lasers and then synchronized optically or electrically to control the pulse timing. The injection of a stable external signal to the hybrid mode locked lasers aids in stability of the pulses and reduction of the jitter [14]. The external electrical/optical signal could control the laser source and encoding of the input data [15] in telecommunications. Hybrid mode locking takes the best of active and passive mode locking i.e. the combination of short pulse generation properties of passively mode locked lasers and small timing jitter and stable operation properties of actively mode locked lasers [16]. Hybrid mode locking has applications in data communication systems, where synchronization of pulses is required.

3.5   Semiconductor Optical Amplifiers

SOAs are optoelectronic devices which can directly amplify the input optical signals. The SOAs are very similar in operation to semiconductor lasers but without (or negligibly small) optical feedback from the facets. SOAs are normally based on a p-n double-heterojunction, which provides optical as well as carrier confinement. In the p-n junction, holes from the p-side and electrons from the n-side of the device are injected into the active region, which is made of lower band gap semiconductor material than the cladding layers. These holes and electrons recombine in the active region and results in the optical gain for propagating light in the waveguide. The optical gain of the input signal is due to the stimulated emission of photons. The basic structure of an SOA is shown in Figure 3.9. An optical signal is injected into waveguide of an SOA, during propagation in the waveguide, the optical signal experiences amplification. The optical gain is achieved by electric current injection into the active region. Based on the material used, SOAs are classified into two main groups, i.e. bulk SOAs and quantum well SOAs [17]. The active region of the bulk SOAs is simply a direct bandgap material, whereas the active region of the quantum well (QW) SOAs is normally based on separate confinement heterostructure (SCH) and consists of QWs and barriers. SOAs with multiple quantum wells (MQWs) in the active region provide higher gain to TE mode. This polarization dependence of the optical gain in MQW-SOAs could be significantly reduced by introducing tensile strain in the active region [18]. In addition, the MQW-SOAs

have small modal overlap with the active region (low optical confinement), which results in higher saturation output power [19].
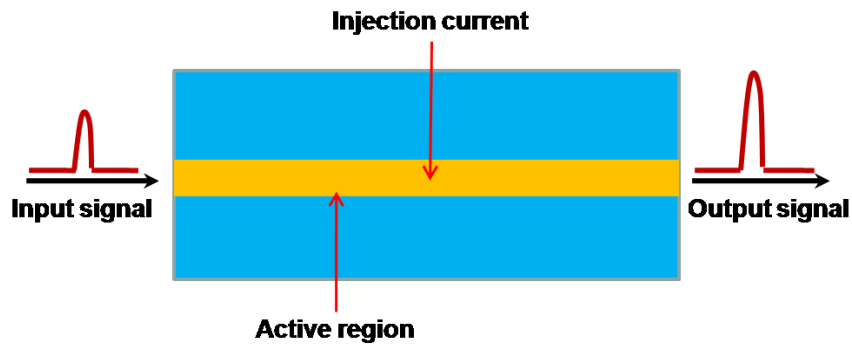
Figure 3.9: Schematic of an SOA.

Optical components including SOAs are of main interest in data transmission due to increasing data traffic and wide use of fibre optics. The use of SOAs in the systems enables signal processing in the optical domain without converting the signal to electrical domain. SOAs can be used as in-line optical amplifiers in the optical systems instead of regenerators to compensate for fibre losses. SOAs are attractive for in-line amplification due characteristics like compatibility with single mode fibres and high optical gain. In addition, SOAs can be also used as power boosters in the systems, for example, to compensate for splitting losses in the optical distribution networks [17]. Comparing to its fibre counterparts, SOAs are compact, low cost, electrically pumped and have a large optical bandwidth. Moreover, the semiconductor technology offers flexibility in choosing the gain peak wavelength simply by choosing the material composition of the active region. SOAs are generally made of III-V semiconductor alloys such as GaAs, InP and different combination of these materials. For operating wavelength of around 1550 nm, InGaAsP/InP and AlGaInAs/InP epitaxial materials are commonly used. Another advantage of SOAs is that it can be easily integrated with other optical components to make complex functionalities photonic integrated circuits (PICs). Due to the higher TE gain and higher saturation output powers, the MQW-SOAs are attractive candidates for monolithic integration with semiconductor lasers for increasing the output power of the lasers.

3.6   Optical Feedback

SOAs are classified into two main categories, Fabry-Perot SOAs (FP-SOAs) and Travelling wave SOAs (TW-SOAs). In FP-SOAs, the reflections from the input and output facets are

significant. The input optical signal undergoes many passes through the amplifier which results in resonant amplification of the Fabry-Perot modes. This kind of amplifiers gives a large optical gain at wavelengths corresponding to the cavity modes while the optical gain at wavelengths other than the cavity modes is small. Figure 3.10 (left) shows modulation in the output spectrum of an FP-SOA. This modulation of the optical gain in the amplifiers is undesirable and limits the use of FP-SOAs in optical networks [20]. The FP-SOA requires critical frequency matching of the input optical signal and the cavity modes.

TW-SOAs, in contrast have negligibly small reflections from both the facets. The input optical signal is amplified during a single pass in the amplifier. Further, TW-SOAs give a broad output optical spectrum. In terms of performance, TW-SOAs are superior to the FP-SOAs due to their large gain bandwidth, increased signal gain saturation and reduced noise figure [21]. Furthermore, TW-SOAs are less sensitive to the fluctuations in injected current, temperature and input signal polarization, as compared to the FP-SOAs [17]. Figure 3.10 (left) shows the optical spectrum of an FP-SOA. The Figure shows gain ripples (shown in the inset), which are due to the reflections from the facets. To achieve the travelling wave operation of SOAs, the output facet reflectivity must be reduced in order to suppress the cavity effects. In most practical TW-SOAs, very small gain ripples are normally observed in the gain spectra, as shown in Figure 3.10 (right). These gain ripples are due to residual reflections from the facets. The optical feedback from the facets must be carefully reduced, because high facet reflectivity has detrimental effects on the performance of SOAs.
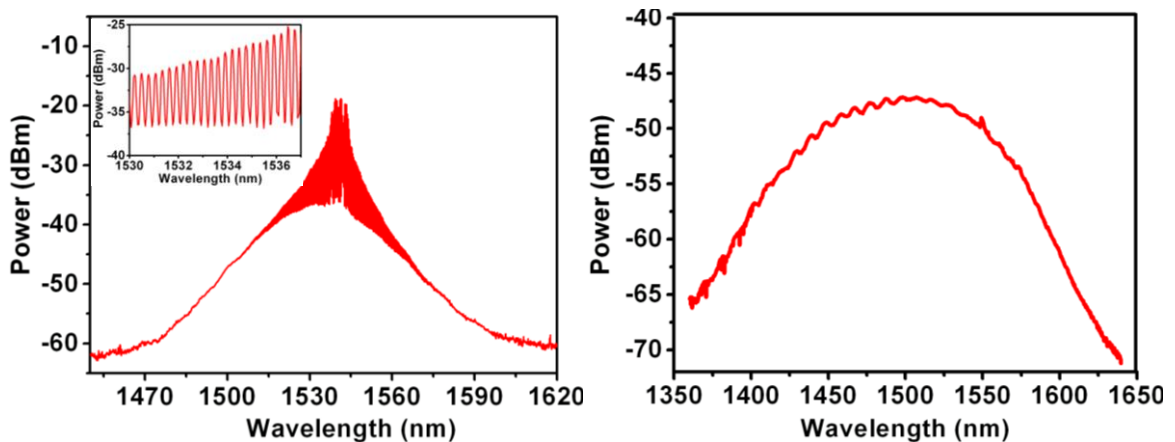
Figure 3.10: (Left) Optical spectrum of an FP-SOA (inset) showing gain ripples due to the facet reflections and (Right) optical spectrum of a TW-SOA with negligibly small facet reflectivity.

Lower facet reflectivity (generally $< 10^{-5}$) is required to obtain higher gain, large gain bandwidth, increased saturation output power and superior noise performance. In this work, our discussion will be limited only to discuss the theory related to the TW-SOA operation.

3.7   Reduction of Facet Reflectivity

For an ideal TW-SOA, the reflectivity from the facets should be zero. However, in practice the TW-SOAs show some cavity effects, which is due to the residual reflectivity of the facets. One of the most critical aspects of TW-SOA design is the reduction of facets reflectivity. As shown in Figure 3.10 (right), the gain spectrum of the TW-SOA shows small gain ripple, which indicate low residual facet reflectivity. The gain ripples (ΔG) are defined as, the ratio between the resonant and non-resonant gain of the amplifier [21].

$$\Delta G = \left[\frac{1 + \sqrt{R1R2}\ Gs}{1 - \sqrt{R1R2}\ Gs}\right]^2$$

Equation 3.7

where R_1 and R_2 are the facet reflectivities and G_s is the single pass amplifier gain.

For ideal TW-SOAs, both $R_1=R_2=0$, and in this case $\Delta G=0$ dB, i.e. no gain ripple occur. For practical TW-SOAs, the gain ripple should be less than 3 dB. Figure 3.11: shows the calculated gain ripple versus reflectivity for optical gain value of 10 dB and 20 dB. When $\sqrt{R1R2}\ Gs < 0.17$, then $\Delta G < 3dB$ and SOA would be TW-SOA. The required facet reflectivity $R\ (=\sqrt{R1R2}\ )$, which depends on the signal gain ripple (ΔG) and single-pass gain (G_s), is given by:

$$R = \frac{1}{Gs}\left[\frac{\sqrt{\Delta G} - 1}{\sqrt{\Delta G} + 1}\right]$$

Equation 3.8
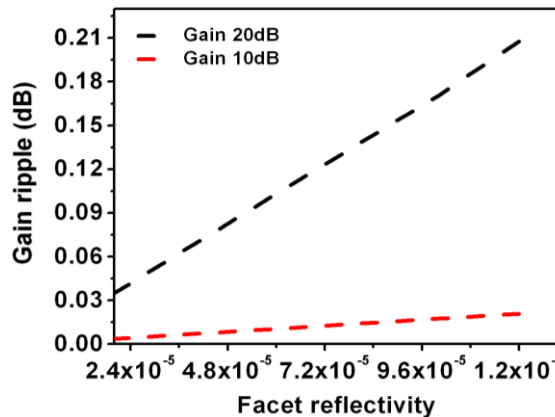
Figure 3.11: Calculated gain ripples vs. facet reflectivity for chip gain of 10 dB and 20 dB.

Different techniques can be employed to reduce the facets reflectivity of the SOAs for achieving TW operation. These techniques include, anti-reflections (AR) coatings [22], angle facet structures [17], and window facet structures [23]. The angled facets structures were used in this work to reduce the SOAs output facets reflectivity.

3.7.1 Antireflection Coatings

The AR coatings are widely used for reducing the facets reflectivity of the cleaved facets SOAs. Many dielectric materials, including SiO, SiN, SiO_2 and PbO- SiO_2 can be used as AR coating films on semiconductor-air interface of SOAs [24]. The refractive index of the AR coating should lie between that of the semiconductor device and air. If a plane wave of wavelength λ is incident on a material of refractive index n_s, then the optimal conditions for refractive index (n_f) and thickness (d_f) of a single AR coating for lowest reflectivity are [17]:

$$n_f = \sqrt{n_s}$$
$$d_f = \frac{\lambda}{4n_f}$$

Equation 3.9

The above conditions of the film thickness and refractive index for lowest facet reflectivity are only valid for simple plane waves at normal incidence. However, guided waves are different from simple plane waves due to guided nature of the modes. Further, these conditions apply only to a particular wavelength. A single AR coating layer is not suitable for entire gain bandwidth of an SOA. For wide band applications, multi-layers of dielectric AR coating can be used. Due to the critical nature of the AR coatings, alternate techniques for reduction in facet reflectivity of SOAs in this work were investigated.

3.7.2 Angled Facet Structures

Another way to reduce the output facet reflectivity is to angle waveguide to the cleaved facet during the device fabrication. Tilting the waveguide at some angle to the cleavage plane reduces the coupling between incident and reflected fields, which leads to decrease in the effective reflectivity of the facets. The tilted facets structures have been investigated for fabrication of superluminescent diodes (SLDs), external-cavity mode locked laser diodes and TW-SOAs [25]. A Schematic of the tilted facets SOA is shown in Figure 3.12.
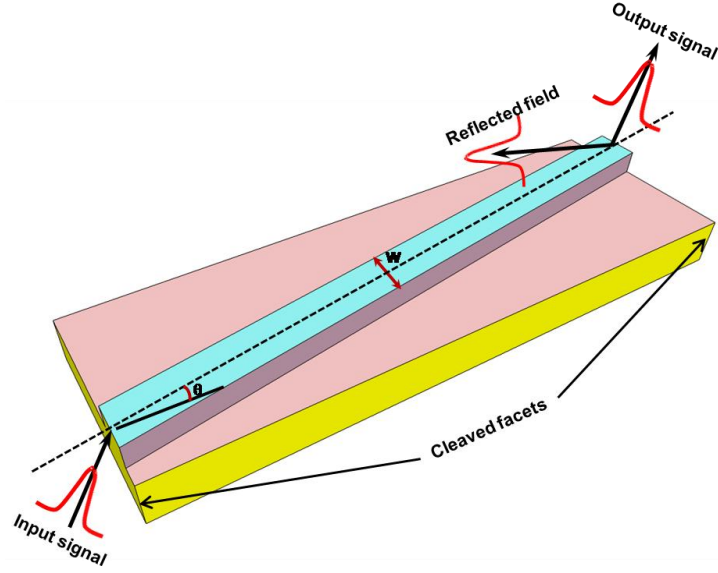
Figure 3.12: Schematic of a TW-SOA with titled waveguide.

Assuming Gaussian distribution of the incident and reflected transverse electric (TE) mode, the effective reflectivity $(R_{eff}(\theta))$ of an angled facet waveguide is given by [21]:

$$R_{eff}(\theta) = R_f(\theta)e^{\left[-\left(\frac{2\pi n_2 w\theta}{\lambda}\right)^2\right]}$$

where
$$k = \frac{2\pi n_2}{\lambda}$$

$$R_{eff}(\theta) = R_f(\theta)e^{[-(k_{cl}w\theta)^2]}$$

Equation 3.10

where $R_f(\theta)$ is the Fresnel reflectivity, θ is the angle of the waveguide, w is Gaussian mode spot size. The Fresnel reflectivity, R_f of a TE plane wave at tilted semiconductor-air interface is given by [17]:

$$R_f(\theta) = \frac{n_1 cos\theta - \sqrt{1 - n_1{}^2 sin^2\theta}}{n_1 cos\theta + \sqrt{1 - n_1{}^2 sin^2\theta}}$$

Equation 3.11

where n_1 and n_2 are the effective refractive indices of the active and cladding layers, respectively. Using Equation 3.10, the effective facet reflectivity is calculated as shown in Figure 3.13. The figure shows that the effective reflectivity of the facets decreases with increasing the facet tilt angles (θ). Increase in the facet angle is limited by the asymmetry of the far-field.
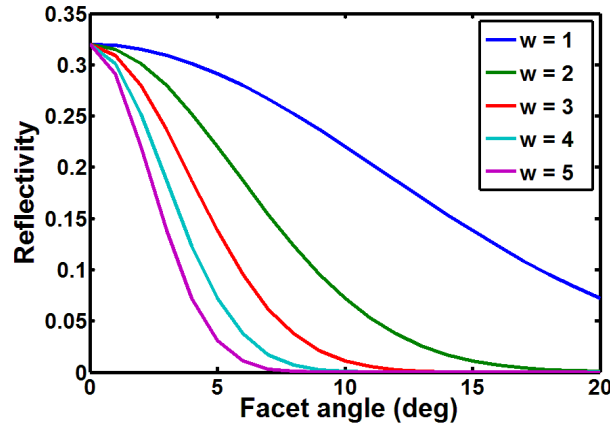
Figure 3.13: Facet reflectivity versus facet angle with an initial reflectivity of 0.32, for mode FWHM sizes

from 1 μm to 5 μm.

The figure also shows the dependence of the effective reflectivity on effective mode width (w). For a given tilt angle, an increase in mode spot size reduces the overlap integral between incident and reflected fields and therefore reduces the facets effective reflectivity.

As will be discussed in Chapter 6, (Section 6.2), this technique was used in this work to reduce the output facet reflectivity of SOAs. Comparing to standard epitaxial structures, the epitaxial structure used in this work consists of an optimized 0.160 μm thick FRL in the n-cladding, which will be described in Chapter 4 (Section 4.5). The FRL increases the spot size in the vertical direction. This increase in the spot size results in an additional reduction in the facets effective reflectivity of SOAs.

3.8 ASE Spectra and Optical Gain

Optical gain, ASE spectra and saturation output power are considered to be among the most important characteristics of SOAs. The ASE of SOAs provides important information about the device. In SOAs, ASE is produced due to the combination of spontaneous and stimulated emission of photons. Spontaneous emission produce photons, a fraction of these photons are coupled into the waveguide and get amplified by the stimulated emission. The ASE output of an SOA has a wide optical bandwidth due to spontaneously emitted photons and high intensity due to optical amplification by the stimulated emission. The ASE provides information about the optical gain, optical bandwidth, gain peak and residual facet reflections.

ASE adds noise to the signals amplified by the SOAs and also depletes charge carriers, which limit the maximum small signal gain of the device. ASE spectra measurement is the fastest

and easiest way to measure the optical characteristics of SOAs. An increase in the injection current to the SOAs results in increase in spontaneous emission, and hence higher gain. The ASE output power also increases with increasing the device length due to the increase of the gain. An increase in injection current causes a blue shift of the peak wavelength due to the band filling effect [26].

Another important parameter of SOAs is the optical gain. Optical gain is the ratio of output power (P_{out}) to the input power (P_{in}) of an SOA. When an optical signal passes through the active region of an SOA, the intensity (I) of the input signal grows more or less exponentially along the length of the SOA. However, when the intensity of the input signal reaches to the saturation intensity level of the device, the growth rate of the input signal decreases. This effect is shown in Figure 3.14. The gain saturation is caused by depletion of carrier density in the active region because of increase in stimulated emission. The highest achievable gain in SOAs is called small signal gain (SSG). The SSG increases with an increase in the injection current, at high current densities the SSG saturates.
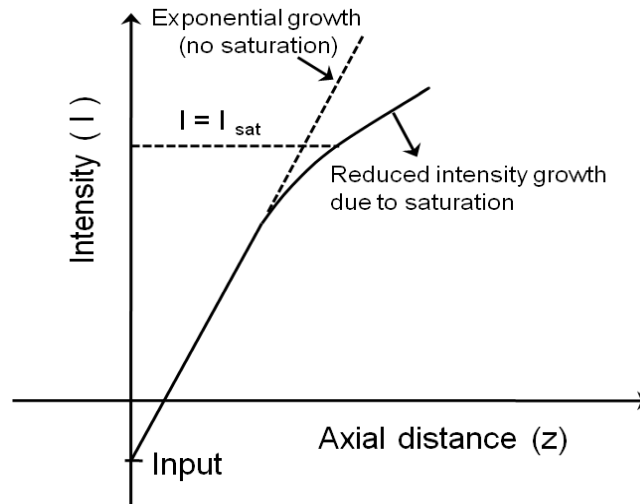
Figure 3.14 Intensity saturation as a function of distance along a TW-SOA [27].

Mainly two factors contribute to the SSG saturation at high injection currents, i.e. increased Auger recombination and increased ASE. The Auger recombination is a dominant recombination mechanism and is proportional to the cube of carrier density (n^3) [28]. Saturation characteristics of the SOAs are also dependent on the input signal wavelength. For shorter input wavelengths, the SOAs are more easily saturated than the longer input wavelengths, this effect is due to band filling [29].

The basic differential equation governing the growth of signal intensity inside the active region of SOAs is [17]:

$$\frac{dI}{dZ} = \left(\frac{\Gamma g_o}{1 + \dfrac{I}{I_{sat}}} - \alpha \right) I$$

<div align="right">*Equation 3.12*</div>

where g_o is the unsaturated material gain co-efficient, Γ is the optical confinement factor, I_{sat} is the saturation intensity of the signal, which is the optical intensity required to reduce the gain co-efficient by 3 dB. The value of I_{sat} is given by [17]:

$$I_{sat} = \frac{h\upsilon}{a_1 \tau}$$

where a_1 is the differential gain and τ is the carrier lifetime.

Integrating Equation 3.12 from input facet to output facet of SOA gives:

$$I_{out} e^{\left(\frac{I_{out} - I_{in}}{I_{sat}} \right)} = I_{in} e^{((\Gamma g_o - \alpha)L)}$$

<div align="right">*Equation 3.13*</div>

Small signal gain ($I << I_{sat}$) can be obtained from Equation 3.13.

$$I_{out} = I_{in} e^{((\Gamma g_o - \alpha)L)}$$

$$G_o = \frac{I_{out}}{I_{in}} = e^{((\Gamma g_o - \alpha)L)}$$

<div align="right">*Equation 3.14*</div>

Equation 3.14 gives the small signal (unsaturated) gain of the device. It is clear from Equation 3.14 that the optical gain can be increased by increasing the device length, optical confinement factor, material gain, and by decreasing the internal loss. In fact, the value of optical gain depends on I_{in} and I_{out} as well, because intensity changes along length z of the amplifier. Putting $\alpha = 0$, i.e. no linear losses in Equation 3.13 and re-arranging gives [27]:

$$\ln\left(\frac{I_{out}}{I_{in}} \right) + \left(\frac{I_{out} - I_{in}}{I_{sat}} \right) = \ln G_o$$

<div align="right">*Equation 3.15*</div>

where $G_o = exp\ (\Gamma g_o L)$ is the small signal gain. Equation 3.15 can also be written as:

$$G = \frac{I_{out}}{I_{in}} = G_o \cdot e^{\left[-\left(\frac{I_{out} - I_{in}}{I_{sat}} \right) \right]}$$

<div align="right">*Equation 3.16*</div>

Equation 3.16 shows that saturated gain "G" at a given value of I_{in} (or I_{out}) is reduced below the unsaturated gain, G_o.

3.9   Saturation Output Power

For low output power, the optical gain of an SOA is equal to the SSG. However, for large output power, the optical gain of an SOA starts to decrease mainly due to depletion of carrier density. Saturation output power (P_{sat}) is the value of output power at which the gain of SOAs reduces by 3 dB from unsaturated value of gain. Generally, P_{sat} indicates the upper limit of linear operation of SOAs. In system applications, the SOA operation in saturated regime causes cross-talk of input signals.
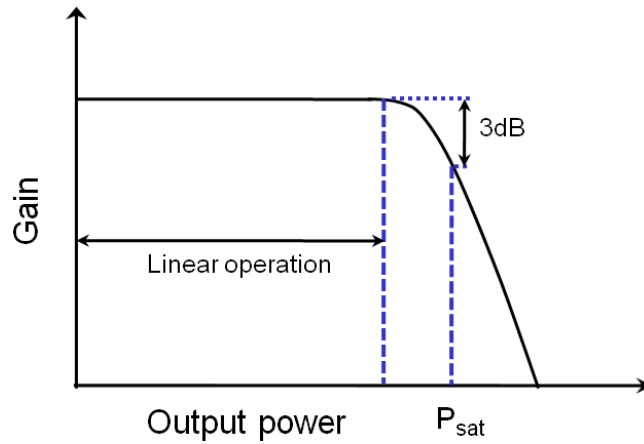
Figure 3.15: Typical saturation characteristics of an SOA.

Thus the value of P_{sat} of the SOAs is desired to be as large as possible. Mathematically, value of P_{sat} is given by [17]:

$$P_{sat} = \frac{AI_{sat}}{\Gamma}$$

Equation 3.17

where I_{sat} is the saturation intensity of the SOA and A/Γ is the modal cross-sectional area. Equation 3.17 shows that one way of improving P_{sat} is increasing I_{sat}. As discussed earlier, I_{sat} can be improved by reducing differential gain (a_1), or the carrier lifetime (τ). The carrier lifetime can be reduced by injecting higher current densities. However, high injection carrier density leads to more significant gain resonance effects and also causes blue shift of the operating wavelength. The differential gain in MQW-SOAs is much lower than the bulk-material SOAs, which is the main reason for higher P_{sat} of the MQW-SOAs [17]. Another way

of improving P_{sat} is increasing A/Γ, i.e. increasing the modal cross-sectional area. In the MQW epitaxial material design for SOAs, reduction in Γ could be achieved by reducing the number of QWs in the gain medium. Results reported in [30] showed that an increase in P_{sat} by decreasing the number of QWs in the active region. The novel epitaxial structure used in this work contain active region with 3 QWs in tandem with appropriate waveguide design to increase the spot size of the guided mode and hence A/Γ. This would result in an improved P_{sat} for SOAs based on this epitaxial structure.

3.10   Dynamic Effects on Pulse Amplification

SOAs are mostly used in the telecommunication systems for amplification of modulated signals. The injected charged carriers produce electron and hole pairs, which provide optical gain to the input pulse. SOAs are capable of amplifying optical pulses as short as few pico-seconds without any distortion. The processes which determine the amplification of optical pulses and gain variations after propagation of an optical pulse in SOAs are classified as the inter-band processes and intraband processes.

3.10.1 Inter-band Processes

The inter-band processes are generally slow processes (few hundred picoseconds), they depends on recovery of the carriers density. In SOAs, inter-band processes are dominant when long (few picoseconds) optical pulses are used as input signals. To investigate the inter-band processes during pulses amplification in the SOAs, carrier lifetime is an important parameter. This is due to the fact that gain response time of the SOAs is associated to its carrier lifetime. Various carrier recombination mechanisms that influence the carrier lifetime in the SOAs are defect recombination, surface carriers recombination, spontaneous emission recombination and Auger recombination. The carrier recombination in the absence of stimulated emission is given by [3]:

$$R_{(N)} = A_{nr}n + B_{(n)}n^2 + Cn^3$$

Equation 3.18

where A is coefficient for unimolecular recombination caused by the defects or trapping sites, B is the coefficient for radiative (bimolecular) spontaneous recombination and C is the coefficient for Auger recombination. The spontaneous carrier lifetime may be approximated by [3]:

$$\tau = \frac{1}{\frac{\partial R}{\partial N}} = \left(A_{nr} + 2B_{(n)}n + 3Cn^2\right)^{-1}$$

<div align="right">*Equation 3.19*</div>

The plot of the carrier lifetime versus the carrier density for AlGaInAs material is shown in Figure 3.16. Carriers lifetime is calculated using Equation 3.19, with $A_{nr} = 7 \times 10^7 \ s^{-1}$, $B_n = 1.5 \times 10^{-10} \ cm^3 s^{-1}$ and $C = 1.4 \times 10^{-28} \ cm^6 s^{-1}$ [31].
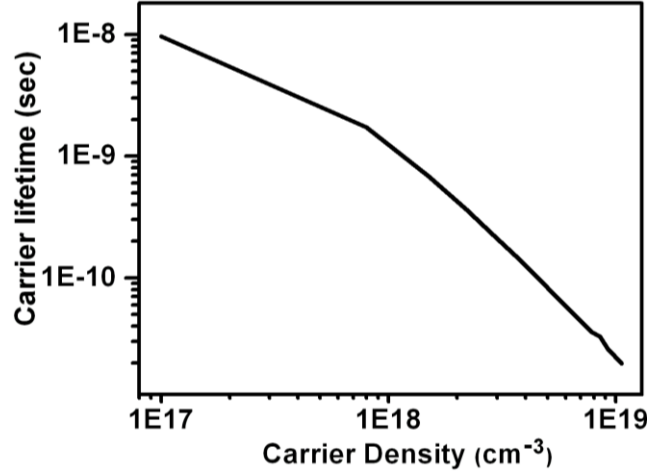
Figure 3.16: Calculated carrier lifetime vs. carrier density of AlGaInAs epitaxial material.

For carrier density of around $2 \times 10^{18} \ cm^{-3}$, the calculated carrier lifetime (τ) is 460 ps. This carrier lifetime is much larger than pulse duration of an isolated pulse, which is generally few picoseconds. This means that the gain of the amplifier will react relatively quickly to the changes in the input signal. Generally, when the repetition rate (T_r) of input pulse is greater than $1/\tau$, the pulses are amplified with negligible distortion because the gain does not recover to its unsaturated value between the pulses. However, if the input pulse repetition rate is of order of $1/\tau$, then the carrier density reach to steady value between the two consecutive pulses, which leads to pulses distortion and pattern effects. These effects on input pulses during pulse amplification are deleterious for linear amplification. In the erbium doped fiber amplifiers (EDFA), the fluorescence lifetime of Erbium is quite long (~10 ms) as compared to SOAs. The long carrier lifetime in EDFAs causes lower distortion of the input pulses for repetition rate down to kHz [32].

As given in Chapter 2 (Equation 2.1), the pulse saturation energy of a semiconductor gain medium depends on the photon energy ($h\upsilon$), the modal cross-sectional area (A), the optical confinement factor (Γ) and the differential gain (dg / dN) [33].

If the energy (E) of an input pulse is less than or comparable to E_{sat}, then the pulse can be amplified without any significant distortions. However, if the energy of the input pulse is larger than the saturation energy of the gain medium, the gain significantly reduces due to the gain saturation. The gain saturation induced non-linearities lead to temporal gain difference between the leading and trailing edge of the pulse and causes pulse broadening. In saturation regime, the pulse broadening as well as pulse compression, depending on operating condition and input pulse shape, has been theoretically explained and experimentally observed [34]. During propagation in the SOA, the leading edge of an input pulse saturates the gain medium of SOA and thus reduces the gain available for the trailing edge of the pulse. This difference of the gain for the leading and trailing edges of the input pulse normally causes pulse broadening. Similarly, pulse compression is due to slight trimming of the trailing edge of the pulse due to gain saturation.

The gain saturation in the SOAs also causes changes in the refractive index, which shifts the pulse spectrum towards longer wavelengths. The carrier density in the SOAs changes as the input pulse propagates through the SOA. The time dependent changes in the carrier density cause changes in effective index, which are responsible for self-phase modulation (SPM) [21]. The induced phase shifts due to SPM on the leading and trailing edges of the input pulses are different and hence the pulses at output of the amplifier get chirped.

3.10.2 Intra-band Processes

Intra-band carrier dynamics becomes more important when very short optical pulses (sub-picosecond) are injected into the SOAs. Intra-band effects changes the distribution of electrons in CB and holes in the VB. The following non-linear effects influence the gain dynamics of short input pulses to the SOAs:

- Spectral hole burning (SHB)
- Two-photon absorption (TPA)
- Carrier heating (CH)

When a short optical pulse enters the SOA, it causes reduction (holes) in the carrier distribution at particular photon energy. This process is called spectral hole burning (SHB). In SHB process, the carrier distribution is deviated from Fermi-distribution and the time (τ_{SHD}) needed to restore the Fermi-distribution by scattering process is around 70-200 femto-seconds [35]. SHB modulates the occupation probability of the carriers within a band, which leads to

fast gain modulation. Carrier heating (CH) process increase temperature of carrier distribution, which decreases the optical gain. The CH is mainly caused due to stimulated emission and free carriers absorption. The carrier distribution cools down to lattice temperature by emitting phonons. The CH recovery time (τ_{CH}) is in range from several hundred femtoseconds to few picoseconds [36]. Two photons absorption (TPA) also contribute to the carriers heating. The TPA excites carriers to higher energy states inside both the CB and VB. The hot carriers in the higher energy states give their excess energy to the carrier distribution through carriers-carriers scattering and causes heating the carrier distribution. Through phonons emission, the carrier distribution cools down to the lattice temperature. The TPA process is strongly dependent on the input pulse intensity.

Analysis of the intra-band processes and their effects on input pulses is reported in [33, 37]. The detailed analysis of intra-band processes and its effects on amplification of input pulses is out of scope of this work.

3.11   Pulse Amplification and Integration of SOA with SMLL

As mentioned earlier, SMLLs are capable of generating short optical pulses with high repetition rates. An interesting feature of the SMLLs is the potential for monolithic integration with other optoelectronic components. A simple and easy-to-implement approach for achieving high output power in SMLLs is the use of an integrated SOA to amplify the output pulses of the SMLL. Different effects on pico-second optical pulses, as they propagate through the SOAs are detailed in [38, 39]. As explained in Section 3.10, the shape of an optical pulse propagating through an SOA is determined by the inter-band and intra-band processes. The experimental results reported in [40] showed that the integrated SOA at the output of a SMLL has negligible negative effects on the output pulse quality, whereas it boost the output power of the SMLL.

In order to monolithically integrate a SMLL with an SOA at the output, intra-cavity reflectors are required to define the laser cavity. The intra-cavity reflectors could be obtained by using either deep etched slots or DBRs. In this work, due to ease of fabrication, surface etched DBRs were integrated with the SMLL to provide optical feedback.

3.12   Mode Locked Lasers Integrated with DBR Gratings

As mentioned in the last section, the DBRs in this work were used to provide optical feedback in the laser cavity of the monolithically integrated SMLL with an SOA. The DBR provide frequency dependent optical feedback inside the cavity. The lasers integrated with DBRs provide single frequency operation and wavelength tunability by injecting current to the DBR section of the laser. A DBR mirror is normally formed by etching the semiconductor material in a periodic fashion during device fabrication stage. The corrugation formed due to the etching of semiconductor material provides periodic perturbation of refractive index inside the cavity, which provides optical feedback in the cavity. Gratings are based on the concept that many reflections from the gratings corrugations can interfere constructively and results in large net reflection. The Schematic of surface etched DBR gratings is shown in Figure 3.17.
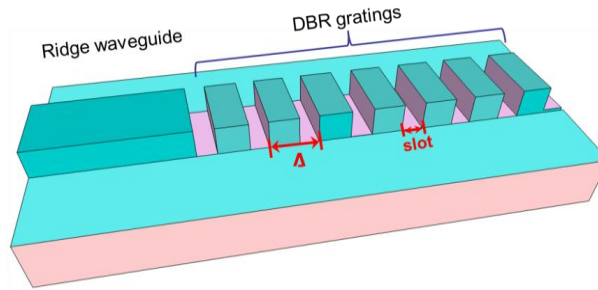
Figure 3.17: Schematic of a ridge waveguide and surface etched DBR gratings.

The gratings period (Λ) should be an integral multiple of half wavelength in the laser medium [3]:

$$2\Lambda = \frac{m\lambda_m}{n_{eff}}$$

Equation 3.20

where *m* is the gratings order, λ_m/n_{eff} is the wavelength inside the laser medium and n_{eff} is the effective index of the guided mode. The wavelength of operation can be selected by selecting appropriate period of the gratings. The fraction of the optical power reflected by DBR gratings depends on the total length of the gratings, depth of the gratings corrugation and thickness of wave guiding layer. Different orders of DBR gratings (i.e. different m values in Equation 3.20) can be selected. However, due to the fabrication tolerances, 2nd and 3rd order gratings are normally fabricated. The DBRs are indispensable for SMLLs due to its features like controlling the spectral bandwidth, centre wavelength and additional tuning of peak

wavelength and pulse repetition rates [41]. As discussed in Section 3.3.3, the spectral bandwidth of the SMLLs is inversely related to its temporal pulse width. The reflection bandwidth of the DBR gratings limits the 3 dB bandwidth of the optical spectra (typically < 1 nm) of the DBR-SMLLs. This imposes a lower limit on the pulse duration of the DBR-SMLLs for transform limited output.

The transform limited time-bandwidth product (TBP) of the pulses emitted from SMLLs is [8]:

$$TBP = \Delta\upsilon\Delta\tau$$

where $\Delta\upsilon$ is the spectral bandwidth of the locked modes and $\Delta\tau$ is FWHM of the temporal pulse. The TBP depends on the pulse shape. For $sech^2$ shaped pulses, the transform limited TBP is 0.315, for Gaussian shaped pulses 0.441 and 0.142 for Lorentzian shaped pulses.

3.13   Chapter Summary

In this chapter, the basic background theory related to the SMLLs and SOAs was described. This chapter began by introducing the semiconductor lasers with various techniques for producing optical pulses in semiconductor lasers. Mode locking is the most efficient and cost effective technique for producing short and stable pulses in semiconductor lasers. Effects related to pulse shortening and broadening in SMLLs were discussed.

This was followed by introducing the structure, operating principles and characteristics of SOAs. Optical gain, inter-band and intra-band processes in SOAs and their effects on optical pulses amplification in the SOAs were briefly discussed. SOAs were described to be an attractive choice for monolithic integration with the mode locked lasers. For integrated devices, as presented in Chapter 6, DBRs were required to define the cavity of the MLLs. Finally, the SMLLs integrated with DBRs were briefly introduced in this chapter.

3.14   References

1.   N. Holonyak, *The semiconductor laser: a thirty-five-year perspective.* Proceedings of the IEEE, 1997. 85(11).

2.   Guiseppe Tandoi, *Monolithic High Power Mode Locked GaAs/AlGaAs Quantum Well Lasers*, in *School of Engineering*. 2011, University of Glasgow: Glasgow.

3.   G. P. Agrawal and N. K. Dutta, *Long- Wavelength Semiconductor Lasers* 1986, New York: Van Nostrand Reinhold.

4.   P. P.Vasil'ev, *Ultrashort pulse generation in diode-lasers.* Optical and Quantum Electronics, 1992. 24: p. 801-824.

5.   P. Ho, et al., *Picosecond pulse generation with a cw GaAlAs laser diode.* Applied Physics Letters, 1978. 33(3): p. 241-242.

6.   Amnon Yariv, *Quantum Electronics*. 3rd ed. 1988: John Wiley & Sons.

7.   J.Wilson and J.F.B. Hawkes, *Optoelectronics-An Introduction.* 1989: Prentice Hall

8.   Steven McMaster, *Monolithically Integrated Mode-Locked Ring Lasers and Mach-Zehnder Interferometers in AlGaInAs*, in Department of Electronics and Electrical Engineering. 2010: Glasgow.

9.   G. New, *Pulse evaluation in mode-locked quasi-continuous lasers.* IEEE Journal of Quantum Electronics, 1974. 10(2): p. 115-124.

10.   R. Green, et al., *Fast saturable absorption and 10 GHz wavelength conversion in Al-quaternary multiple quantum wells.* Optics. Express, 2011. 19: p. 9737-9743.

11.   Julien Javaloyes and Salvador Balle, *Mode Locking in Semicoductor Fabry-Perot Lasers.* IEEE Journal of Quantum Electronics, 2010. 46(7): p. 1023-1030.

12.   K A Williams, M G Thompson, and I H White, *Long-waveglength monolithic mode locked diode lasers.* New Journal of Physics, 2004. 6:179.

13.   E.A. Avrutin, J.H. Marsh, and E.L. Portnoi, *Monolithic and multi-GigaHertz mode-locked semiconductor lasers: Constructions, experiments, models and applications.* IEE Proc.-Optoelectron., 2000. 147(4): p. 251-278.

14.   G Fiol, et al., *1.3 μm range 40 GHz quantum dot mode-locked laser under continuous wave light injection or optical feedback.* Semicond. Sci. Technol., 2011. 26(1).

15.   Bilal. A. Khawaja and Martin J. Cryan, *Wireless hybrid mode locked lasers for next generation radio over fiber systems.* Journal of light wave Technology, 2010. 28(16): p. 2268-2276.

16.   Takeshi Hoshida, et al., *Subharmonic hybrid mode locking of a monolithic semiconductor laser.* IEEE Journal of Selected topics in Quantum Electronics, 1996. 2(3).

17.   Micheal J. Connelly, *Semiconductor Optical Amplifiers*. 2002, New York: Kluwer Academic Publishers.

18.   Prakash Koonath, et al., *Polarization-Insensitive Quantum-Well Semiconductor Optical Amplifiers.* IEEE Journal of Quantum Electronics, 2002. 38(9).

19.   S. Tanaka, et al. *A High Saturation Output Power (+22 dBm) Polarization Insensitive Semiconductor Optical Amplifier*. in *Lasers and Electro-Optics Society, (LEOS),*. 2005.

20.   Dutta, N.K. and Q. Wang, *Semiconductor Optical Amplifiers*. 2006, Singapore: World Scientific Publishing.

21.   Tadashi Saitoh and Takaaki Mukai, *"Traveling Wave Semiconductor Lasers Amplifiers" in Coherence, Amplification, and Quantum effects in Semiconductor Lasers, *. 1991, USA: John Wiley and Sons, Inc. p.257-322.

22.   T. Saitoh, T. Mikai, and O. Mikami, *Theoretical analysis and fabrication of anti-reflection coatings on laser diode facets.* J. Lightwave Technol., 1985. 3: p. 288-293.

23.   Anthony E Kelly, *Optimization of Semiconductor Optical Amplifiers for Optical Networks*. 1999, University of Strathclyde: Glasgow.

24.   Available online, *http://www.rp-photonics.com/anti_reflection_coatings.html*.

25.   Alphonse, G.A., et al., *High-power superluminescent diodes.* IEEE Journal of Quantum Electronics, 1988. 24(12): p. 2454-2457.

26.   Mitsuo Fukuda, *Optical semiconductor devices*. 1999, USA: John Wiley and Sons.

27.   A. E. Siegman, *LASERS*. 1986, Oxford: Oxford University Press.

28.   Lorenzo Occhi, *Semiconductor Optical Amplifiers made of Ridge Waveguide Bulk InGaAsP/InP: Experimental Characterization and Numerical modelling of Gain, Phase and Noise* in *Eidgenössische Technische Hochschule Zürich*. 2002: Zurich.

29.   K. Inoue, T. Mukai, and T. Saitoh, *Gain Saturation Dependence on Signal Wavelength in a Travelling-Wave Laser Amplifier.* Electron Lett., 1987. 23: p. 328-329.

30.   Ken Morito, et al., *A Broad-Band MQW Semiconductor Optical Amplifier With High Saturation Output Power and Low Noise Figure.* IEEE Photonics Technology Letters, 2005. 17(5).

31.   J. Minch, et al., *Theory and experiment of In$_{1-x}$Ga$_x$As$_y$P$_{1-y}$ and In$_{1-x-y}$Ga$_x$Al$_y$As long-wavelength strained quantum-well lasers.* IEEE Journal of Quantum Electronics, 1999. 35(5): p. 771-782.

32.   Ivan P. Kaminow, Tingye Li, and Alan W. Willner, *Optical Fiber Telecommunications V B*. 2008.

33.   Govind P. Agrawal and N. Anders Olsson, *Self-Phase Modulation and Spectral Braodening of Optical Pulses in Semiconductor Laser Amplifiers.* IEEE Journal of Quantum Electronics, 1989. 25(11): p. 2297-2305.

34.   H. Ghafouri-Shiraz, Peh Wei Tan, and T. Aruga, *Picosecond Pulse Amplification in Tapered-Waveguide Laser-Diode Amplifiers.* IEEE Journal of Selected Topics in Quantum Electronics, 1997. 3(2): p. 210-218.

35.   Roland Peter Schreieck, *Ultrafast Dynamics in InGaAsP/InP Optical Amplifiers and Mode Locked Laser Diodes*, in *SWISS FEDERAL INSTITUTE OF TECHNOLOGY*. 2001: ZURICH.

36.   Ali Rostami, Hamed Baghban, and Reza Maram, *Nanostructure Semiconductor Optical Amplifiers*. 2011.

37.   K Hussain, S K Varshney, and P K Datta, *Intraband effects on ultrafast pulse propagation in semiconductor optical amplier.* PRAMANA Journal of Physics, 2010. Vol. 75(5): p. 1011-1016.

38.   A. M. Clarke, et al., *Investigation of Pulse Pedestal and Dynamic Chirp Formation on Picosecond Pulses After Propagation Through an SOA.* IEEE Photonics Technology Letters, 2005. 17(9).

39.   T. Saitoh and T. Mukai, Gain *Saturation Characteristics of Traveling-Wave Semiconductor Laser Amplifiers in Short Optical Pulse Amplification.* IEEE Journal of Quantum Electronics, 1990. 26(12): p. 2086-2094.

40.   Brain R. Koch, et al., *Monolithic Mode-Locked Laser and Optical Amplifier for Regenerative Pulsed Optical Clock Recovery.* IEEE Photonics Technology Letters, 2007. 19(9).

41.   Lianping Hou, et al., *Monolithic 40-GHz Passively Mode-Locked AlGaInAs–InP 1.55.* IEEE Photonics Technology Letters, 2010. 22(20): p. 1503-1505.

Chapter 4

Material Design and Fabrication Technology

4.1   Introduction

In this chapter basic introduction to the quantum well lasers and their properties along with the design of the epitaxial structure used for device fabrication in this work are described. This is followed by the fabrication tools and processes used in this research work. Main fabrication processes such as e-beam lithography, e-beam resists, dry etching of Silica and AlGaInAs/InP epitaxial material are described. Fabrication of the sub-micron surface etched distributed Bragg reflectors (DBRs) was the most challenging part of this work. Processes such as e-beam dose and dry etching were optimized for realization of sub-micron structured DBRs. Later, metal depositions with the recipes for p-type and n-type metallisation are discussed. The simulation and characterisation results of the ridge waveguide lasers are presented. Finally, the performance analysis of the p-ohmic contacts is presented.

4.2 Quantum Well Lasers

The first semiconductor laser demonstrated in 1962 was based on a simple GaAs p-n junction. Later on, a huge research started on III-V semiconductor binaries (InAs, InP), ternaries (InGaAs, InAsP, AlGaAs, InGaP) and quaternaries (AlGaAsP, InGaAsP, AlGaInP) for the

fabrication of semiconductor lasers. Due to the development of the epitaxial growth methods, the present day lasers consist of a very thin active region typically ~ 10 nm, called quantum well (QW). The electrons and holes confined in the QW show quantum size effects, which results in quantized energy levels in the conduction band (CB) and valence band (VB). Lasing action occurs on the transition between the lowest CB sub-band and highest VB sub-band. Since the active region of the QW is very thin, the generated photons are not effectively confined within the active region. To get round to this problem, semiconductor materials with multiple QWs (MQW) active region can be used. The optical confinement factor, which is the fraction of the optical mode overlapping with the active region, is larger for lasers with MQWs than the lasers with a single QW. The optical confinement factor could be further increased by surrounding the QWs with a larger band-gap material, called separate confinement heterostructure (SCH) [1]. The SCH improves the electrons confinement by confining the charge carriers to the active region and also improve the optical confinement by taking the benefit of increased refractive index with increasing band-gap of the material. Under high electrical injection into the active region, population inversion occurs which leads to the optical gain in the device. The emission wavelength of the device depends on the semiconductor material used.

4.3   Strained Quantum Well Lasers

Both the transverse electric (TE) and the transverse magnetic (TM) modes are supported by the waveguide of the semiconductor lasers. The transition of electrons from the CB both to the heavy-hole VB and the light-hole VB results in the emission of TE polarized output. Whereas the transition of electrons from CB to the light-hole VB gives the TM polarized output. In the lattice matched III-V QW lasers, the heavy-hole VB and the light-hole VB are degenerate (i.e. occupy the same energy (E) and momentum (k) space) and thus mostly emits TE polarized output [2]. Strain can be introduced in the QWs at the time of wafer growth by introducing lattice mismatch between the wells and the adjacent barrier layers, which reduces the degeneracy of the heavy and the light hole VB. Compressive strain in the QWs reduce the effective hole mass and yields more TE gain, whereas tensile strain in the QWs cause an increase in the effective hole mass and yields more TM gain [3, 4].
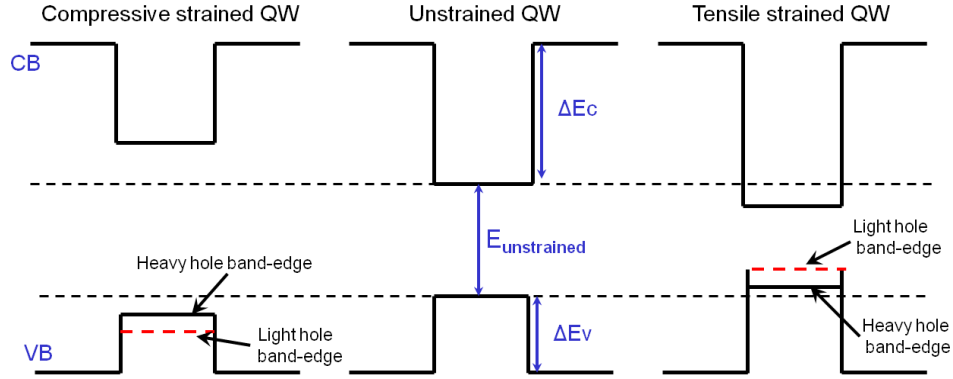
Figure 4.1: Band edge profile showing heavy holes and light holes band edge for compressive, unstrained and tensile strained QWs [5, 6].

As shown in Figure 4.1, the heavy-hole VB edge of the compressively strained QW is closer to the CB than the light-holes VB and thus it favours TE polarized emission. On the other hand, the tensile strain shifts the light-hole VB closer to the CB than the heavy-hole VB, and thus enhances the TM polarized emission.

4.4   Properties of AlGaInAs/InP MQW Structures

As mentioned earlier, the operating wavelength of the semiconductor lasers depends on the material structure used for fabrication of the devices. Devices operating at longer wavelengths (~1550 nm) are normally based on the GaInAsP or AlGaInAs material systems. The GaInAsP material system has largely been superseded by AlGaInAs material due to its improved temperature performance. The temperature performance, however, is determined by the CB offset. As the operating temperature of the lasers increases, the vertical electrons leakage increases as well. This reduces the number of carriers available for lasing. This effect limits the device operation at higher temperatures and also leads to an increase in the threshold currents. The AlGaInAs material system exhibits a larger CB discontinuity ($\Delta E_c = 0.72\Delta E_g$) and smaller VB discontinuity as compared to GaInAsP ($\Delta E_c = 0.40\Delta E_g$), which makes it more suitable for the fabrication of semiconductor lasers [7]. The increased CB discontinuity of the AlGaInAs material improves the electron confinement in the CB. This provides a strong barrier, which reduces the carriers leakage from the active region, and thus allows better performance at higher temperatures [6]. The decrease in the VB discontinuity allows more uniform holes injection in the VB, which is attractive property, especially for the fabrication of semiconductor mode-locked lasers. The decrease in the VB discontinuity helps to alleviate the

holes pile-up in the saturable absorbers. Thus higher saturation intensity is expected, which would increase the range of the saturable absorber reverse voltages, required for mode locking [7].

4.5   Design of 3-QW AlGaInAs/InP Material

The MQW material system used for device fabrication in this work was designed by Dr. Lianping Hou and grown by IQE Ltd. The material structure was based on the standard commercially available laser diodes wafer structure, with some modifications. Comparing to the commercially available epitaxial material, the number of QWs in the modified epitaxial structure were reduced from five to three and a far-field reduction layer (also called optical trap layer) and a spacer layer were inserted in the lower cladding of the structure. Figure 4.2 shows the layer structure of the modified epitaxial material.

Layer	Material	Repeat	Mole Fraction (x)	Mole Fraction (y)	Strain (ppm)	Thickness (µm)	CV Level (cm-3)
18	GaIn(x)As		0.53		0	0.2	1.5E19
17	GaIn(x)AsP		0.71	0.62	0	0.05	3.0E18
16	InP					0.1	1.5E18
15	InP					1.5	1.0E18
14	GaIn(x)AsP		0.85	0.33	0	0.02	1.0E18
13	InP					0.05	7.0E17
12	[Al(x)Ga]In(y)As		0.9	0.53	0	0.06	4.0E17
11	[Al(x)Ga]In(y)As		0.720 to 0.90	0.53	0	0.06	
10	[Al(x)Ga]In(y)As		0.44	0.49	–3000	0.01	
9	[Al(x)Ga]In(y)As	3	0.24	0.71	12000	0.006	
8	[Al(x)Ga]In(y)As	3	0.44	0.49	–3000	0.01	
7	[Al(x)Ga]In(y)As		0.900 to 0.720	0.53	0	0.06	
6	[Al(x)Ga]In(y)As		0.9	0.53	0	0.06	1.0E18
5	[Al(x)Ga]In(y)As		0.86 0to 0.900	0.53	0	0.01	1.0E18
4	InP					0.75	1.0E18
3	GaIn(x)AsP		0.85	0.33	0	0.16	1.0E18
2	InP					1.5	1.0E18
1	InP					0.3	3.0E18
Substrate							

Figure 4.2: Layer table of the epitaxial structure with 3-QWs active region.

The 1550 nm AlGaInAs/InP MQW structure consists of three 6 nm thick compressive strained (+ 1.2%) AlGaInAs QWs and four 10 nm thick tensile strained AlGaInAs barriers. The

MQWs and the barrier layers are sandwiched between the two 60 nm thick graded index separate confinement heterostructure (GRIN-SCH) AlGaInAs layers. Above and below the GRIN-SCH layers, there are 60 nm thick p-AlGaInAs and n-AlGaInAs layers respectively. Further, the structure consists of a 160 nm thick 1.1Q far-field reduction layer and a 0.75 μm thick n-InP spacer layer. Zinc and Silicon are used as p-type and n-type dopants respectively. The energy band diagram of the CB of the epitaxial layers is shown in Figure 4.3. More details of this epitaxial structure can be found in [8]. The heavily doped 0.2 μm thick p+-InGaAs contact layer does not play part in the wave-guiding due to its larger distance from the active region.

In this epitaxial structure, the number of QWs were reduced to three, which decreases the optical confinement factor and hence dg/dN. This will lead to higher gain saturation energy as given by Equation 2.1. Another important modification to the commercially available epitaxial structure is the far-field reduction layer (FRL), inserted in the lower n-cladding layer. The FRL expands the optical near-field in the vertical direction towards the n-cladding layer side.
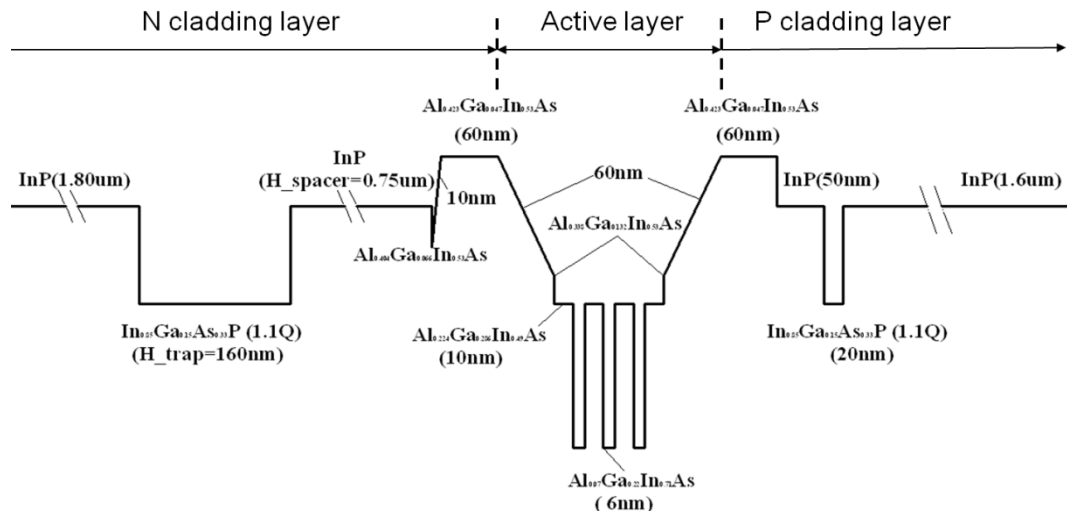
Figure 4.3: Conduction band diagram of 3-QW epitaxial structure.

The FRL pulls the optical mode towards the lower cladding layer causing a reduction in the optical overlap with the p-doped layers. This repositioning of the optical mode reduces the losses resulting from the free carrier absorption, which is higher in the p-doped layer than the n-doped layer and is the main contributor to the internal optical losses [9]. Another main advantage of the FRL is the suppression of the higher order transverse mode lasing. Repositioning of the optical mode towards the n-cladding layer decreases the Γ_{QW} and hence

the lasing threshold current increases. This effect is stronger for higher order modes, which will experience more losses compared to the fundamental mode and hence all the higher order modes will be suppressed [10]. By varying the width of the FRL, the beam divergence and the optical overlap of the modes with the active region can be controlled. The results of simulations done by Dr. Lianping Hou for the optimized FRL thickness (0.16 µm) and spacer layer thickness (0.75 µm) are shown in Figure 4.4. The simulation results for the same epitaxial structure reported in [11] shows that if the FRL is made too thick, the fundamental mode coupling to the FRL increases. This leads to reduction in the Γ_{QW} value of the fundamental mode and an extra peak appears in the near-field pattern.
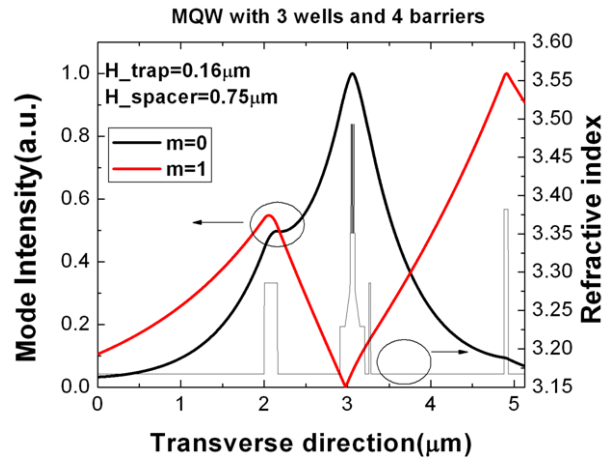
Figure 4.4: Simulation results: Optical intensity for the fundamental and first order modes in the epitaxial structure [11].

The insertion of the FRL and the reduction of number of QWs in the epitaxial structure will cause an increase in the spot size A/Γ, while maintaining the fundamental transverse mode. It is anticipated that this novel epitaxial structure will cause an increase in the output power and reduction in the far-field pattern, internal losses, timing jitter and pulse width of the semiconductor mode-locked lasers.

4.6 Electron Beam Lithography (EBL)

Lithography in semiconductor device fabrication is the transfer of a pattern onto a semiconductor material surface. Lithography processes make use of thin layers of polymers or sensitized resin called resists. There are two main kinds of resists, positive resists and negative resists. During lithography, selective areas of the resists are activated by a specific energy

source such as light (photolithography), electron beams (electron beam lithography), ion beam (ion beam lithography) or x-rays (x-ray lithography). For positive resist, the resist from exposed areas is removed with the development of the sample, whereas for negative resists, the resist from the un-exposed areas is removed with the development of the sample. Figure 4.5 shows the negative and positive resists, respectively, after the exposure and development process.
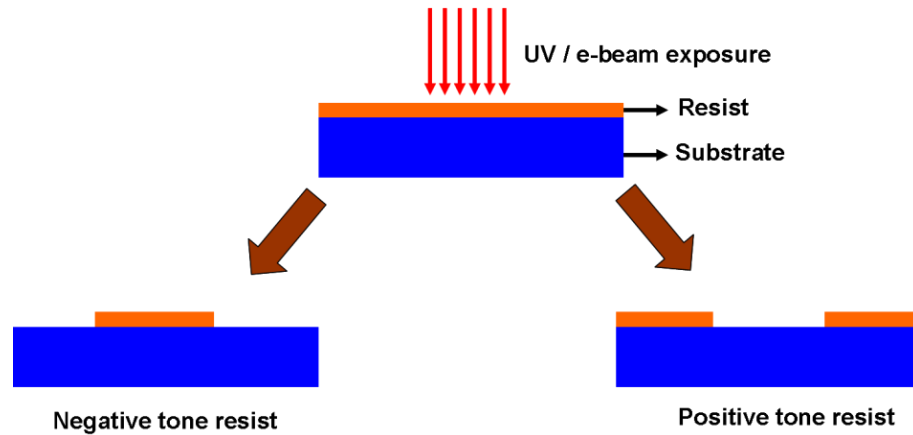
Figure 4.5: Negative and positive resists after exposure and development process.

Photolithography uses ultraviolet light (UV) for resist exposure and is widely used for the fabrication of large features (few microns resolution) in the microelectronics industry [12]. The minimum feature size achievable using any lithography tool is defined by the wavelength (typically 200-500 nm) used in the resist exposure process. The resolution of photolithography is limited by the diffraction limit of the UV light source used for exposure of photoresist. Photolithography was used in this work only to fabricate patterns for the transmission line measurements (minimum feature size of 200 μm). An alternative to photolithography is Electron Beam Lithography (EBL). The characteristics of the EBL like high resolution, large depth of the field and easy pattern modification makes it more attractive. The EBL does not require generating a mask. The resolution of the EBL is of order of few nanometres.

Due to small dimensions of devices required in this research work, EBL was mostly used. A Vestec Vector Beam 6 UHR-EWF electron beam (e-beam) tool was used for the pattern definition in both the positive and negative resists. This EBL tool uses 50 or 100 keV electrons beam and is able to produce a spot size of 4 nm width and resolution of 0.5 nm [13]. In EBL, resist is directly exposed using a focussed beam of energetic electrons, while in photolithography, light from UV source goes through a mask and the image is projected onto

the substrate. The main components in a typical e-beam column are the electron gun, lenses, beam deflectors, aperture for defining e-beam and electron detector. Electrons are thermoionically produced on the surface and then accelerated by applying a high voltage. The beam of electrons is manipulated by a series of electromagnets, which are computer controlled. When the e-beam is focussed on an area of the substrate coated with a resist, the high energy electrons break the resist polymers into fragments, which results in a greater solubility of the resist polymers. These can be removed using a suitable developer solvent.

Figure 4.6: Process flow of pattern transfer by the EBL process.

The minimum width of the e-beam (spot size) is 3 to 4 nm. The pattern is exposed as a set of points and the distance between the two exposed points is defined by the beam step size (BSS). The BSS is an integral multiple of the resolution, i.e. BSS = VRU x resolution, where VRU stands for variable resolution unit. Figure 4.7 shows a schematic, which illustrates the BSS, VRU and resolution. The patterns were designed in the L-edit and a software called CATS (Computer Aided Transcription) was used for fracturing the regions to be exposed, in small areas (trapezia). The small fractured areas are positioned on a periodic grid with the period of grid corresponding to resolution [14]. In this work, resolution of 1.25 nm was used for all patterns.
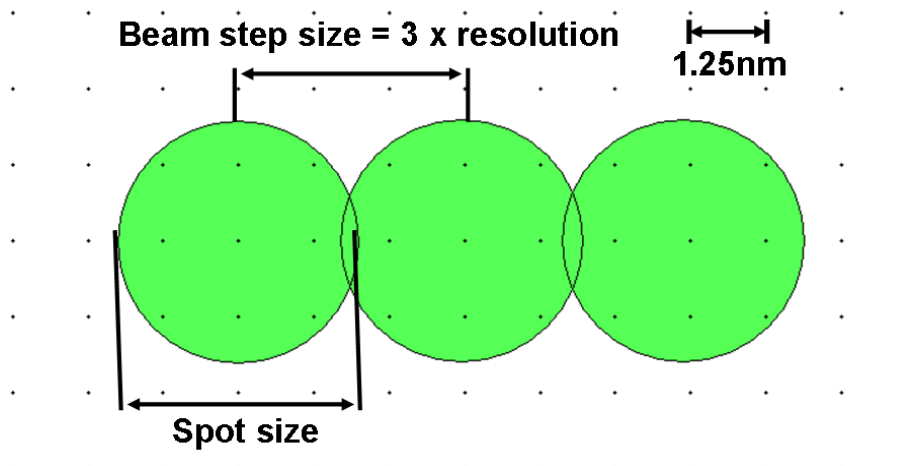
Figure 4.7: Schematic illustrating electron beam spot size, step size, resolution and VRU [13].

4.7 Proximity Effect

The resolution of EBL is limited by the scattering of electrons in the resist and substrate. Typically, the EBL tool uses electron beams with the electrons energy 50-100 eV. For such high energy electrons, the mean free path in the resist is more than the thickness of the resist, so electrons can easily penetrate through the resist and up to some extent in the substrate. During penetration through the resist and the substrate, the electrons undergo electron-solid interaction. As a result of electron-solid interaction, two types of scattering may take place, i.e. forward scattering (inelastic collision) and backward scattering (elastic collision) as shown in Figure 4.8. Forward scattering is due to the collision of incident electrons with electrons from atoms of the resist and substrate, which may create secondary electrons. Backscattering is due to collision/interaction of incident electrons with positively charged nucleus, which causes large changes in the direction of incident electrons. Upon interaction of electrons with the nucleus, the electrons are deflected at large angles as shown in Figure 4.8 [15].
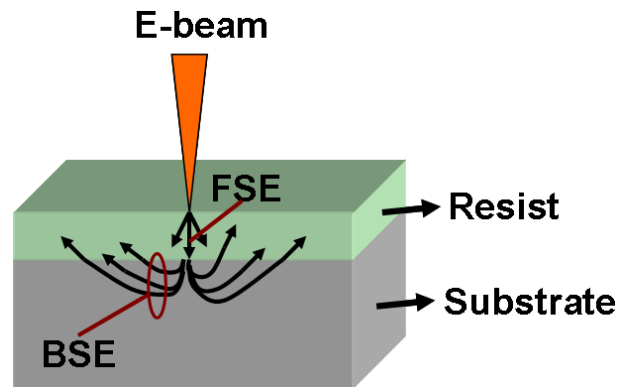
Figure 4.8: Schematic illustrating forward and backward scattering of electrons in resist and substrate.

In Figure 4.8, the forward scattered electrons (*FSE*) as well as backward scattered electrons (*BSE*) are shown. As a result of the scattering of electrons, the exposure region is widened, the corners of a desired pattern get rounded and the gap spaces between the features are modified. To write small features using EBL, these electrons scattering effects must be minimised to get the required dimensions of the features. The available EBL facility has the ability to reduce the proximity effects by modulating the exposure dose according to the density of the pattern. Applying proximity correction during fracturing adjusts the dose of each pattern and thus minimizes the proximity effects. The proximity effects can be further minimized by taking the following measures:

(1)   Optimize e-beam exposure parameters: accelerating voltage, spot size, beam step size, exposure dose.

(2)   Optimize the mask design.

(3)   Use thin resist coatings (for small features).

4.8 Electron Beam Lithography Resists

E-beam resists can be either of the two types, i.e. positive resist or negative resist. Generally, resists are required to have high sensitivity, good adhesion, film uniformity, thermal stability and high etch resistance. The quality of the resist layer plays a fundamental role in the pattern writing using the EBL. To obtain smooth profile of the resist layers, a spinner is used. A few drops of the resist are placed on the substrate and the substrate is spun for set time duration at a specified speed. Normally the spin speed used is 2000-5000 rpm. The thickness of the resist coating is a function of the spin speed and duration. The minimum exposure dose of the e-beam required to fully dissolve (positive resists) or totally unaffected (negative resists) the exposed areas is called nominal dose [12]. In this work, Poly-Methyl Methacrylate (PMMA) was used as a positive e-beam resist and Hydrogen Silsesquioxane (HSQ) was used as a negative e-beam resist. E-beam parameters like beam current, dose and VRU need to be optimized for the set of resist conditions used.

4.8.1   PMMA

PMMA is a high resolution positive e-beam resist. Normally, e-beam exposure doses ranging from 100 to 500μC/cm^2 are used for PMMA. The developer for exposed PMMA is a solution with different concentrations of Methyl Iso-Butyl Ketone (MIBK) and Isopropyl alcohol (IPA). Bi-layers of the PMMA facilitate metal lift off, so it is widely used when metal lift-off is required.

In this work, PMMA was used for defining alignment markers, opening contact windows and p-contact patterns definition. Bi-layers of PMMA were used for the processes that require metal lift off, i.e. definition of alignment markers and p-contact pad. Bi-layer PMMA (normally, 15% 2010 with molecular weight of 100k & 4% 2041 with molecular weight of 410k) gives a total thickness of around 1310 nm, which is sufficient for safe metal lift-off. Firstly, a layer 1200 nm thick of lower molecular weight PMMA (15% 2010) was spun over

the substrate at 5000 rpm for 60 seconds. Then the sample was baked in 180ºC oven for 30 minutes in order to evaporate any residual solvents from the resist and make stronger adhesion with the substrate. This was followed by spinning another PMMA layer (110 nm thick) of higher molecular weight (PMMA 4% 2041) and baked in 180ºC oven for 90 minutes. The lower molecular weight resist layer (PMMA 15% 2010) is more sensitive to the development than the higher molecular weight resist (PMMA 4% 2041). This leads to the production of under cuts in the features and enhances metal lift-off.

Tri-layer PMMA was used in this work for contact window opening on the top of the ridge waveguide structures. The etch selectivity of the PMMA versus SiO_2, using CHF_3 and Argon is around 1:2 [16]. Therefore, to get safe RIE dry etching of 600-700 nm thick SiO_2 for contact window opening, tri-layer PMMA was used. A layer of PMMA (15% 2010) was spun on the sample at 5000 rpm for 60 seconds and baked in 180ºC oven for 30 minutes. The same procedure was followed for the second layer of PMMA. A third layer of PMMA 4% 2041 was spun at 5000 rpm for 60 seconds and baked in 180ºC oven for 90 minutes. These three layers of PMMA give a total resist thickness of ~ 2500 nm.

4.8.2   HSQ

Hydrogen Silsesquioxane (HSQ) is a negative e-beam resist with high resolution and high dry etch resistance for etching III-V semiconductor materials [17]. The molecular structure of HSQ consists of Hydrogen, Silicon and Oxygen (H-Si-O) bonds. The molecules of HSQ are arranged in a cage structure [18]. In these molecules, Si-O bonds are more stable than those Si-H bonds. The less stable Si-H bonds dissociate and adopt a structure similar to silica structure when they get energy from e-beam in the exposure process [17].

In this work, HSQ was used for definition of ridge waveguide structures and DBR mirrors and also for planarization of ridge waveguides. One advantage of using HSQ is that it was used as negative e-beam resist and after the development, the unexposed areas forms SiO_2 pattern, which was used for subsequent dry etching of the material. Thus, the use of HSQ avoids PECVD deposition of silica, which is used as a hard mask for dry etching of material. Deposition of silica usually causes damage to the substrate [17] and roughens the side walls. HSQ is a negative tone resist and only the waveguides and DBR structures are exposed, which substantially reduces the e-beam exposure time. The HSQ (100% concentration) was spun on the substrate at 2000 rpm for 1 minute, which gives film thickness of around 550 nm. The

sample was baked at 91.5ºC for 15 minutes. A series of dose tests were carried out to find best e-beam exposure dose for defining the 2.5 μm wide ridge and the 180 nm wide slots of the DBR mirror. Figure 4.9 show the SEM picture of the DBR and ridge waveguide written in HSQ mask. This figure shows smooth and sharp side walls of the ridge waveguides with the required slot width of the DBR. The e-beam exposure parameters used for these patterns were: e-beam dose 390 μC/cm^2, VRU 5, spot size 9 nm (Spot size > VRU x resolution), beam current 3.9 nA and proximity correction file "*radRIElag_17prox.pec*". After e-beam exposure, the sample was developed in Tetra-Methyl-Ammonium Hydroxide (TMAH) solution for 30 seconds at 23ºC. The sample was then rinsed in two beakers of RO water, each for 30 seconds. Then, finally the sample was transferred to a beaker of IPA, rinsed for 30 seconds and then blow dried with a nitrogen gun. A surface profileometer (Dek-Tak) was used to measure the film thickness after the development process.
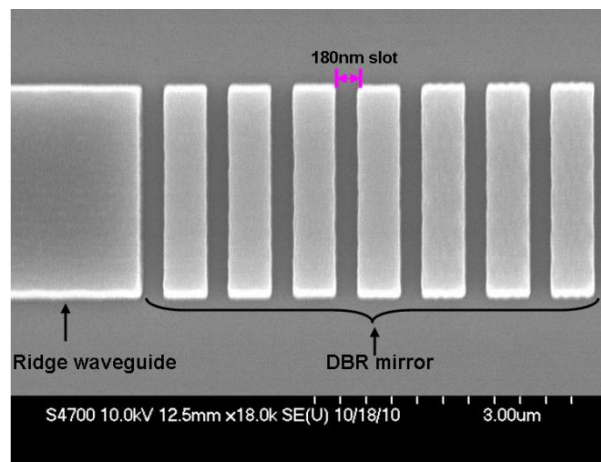
Figure 4.9: SEM picture of the ridge waveguide and DBR gratings in the HSQ mask.

4.9 Silica Deposition

Silica (SiO$_2$) films were used in this work as electrical insulation layers and an optical buffer layer for the fabrication of devices. Silica is a good electrical insulator and allows electrical carriers injection to be restricted to a specific region (contact window) and therefore reduces current leakage at the edges of waveguides. The low dielectric constant makes the silica a suitable choice to be used as a buffer layer between the waveguide and metal contacts [19]. In this work, silica films were deposited on the substrates using a Plasmalab 80Plus tool, which use plasma enhanced chemical vapour deposition (PECVD) process for film deposition. The PECVD deposited silica gives almost uniform film thickness on flat surfaces as well as on

vertical side walls. In addition to this, PECVD silica deposition gives good surface adhesion and high growth rates.

In this process, plasma is generated by the RF (AC) frequency source between the two electrodes. The region between the two electrodes contains the reacting gases. The plasma decomposes precursor gases in a high vacuum environment. The adsorbed species on the surface of the substrate undergoes chemical reactions and form silica film. The silica film thickness, uniformity and deposition rate depends on the PECVD process parameters. The process parameters used for deposition of silica in this work are the same as reported by a colleague [19].

Parameter	Value		
Gas	SiH_4	N_2O	N_2
Flow (sccm)	9	710	171
Power (W)	10		
Pressure (mT)	1010		
Temperature (ºC)	300		

Table 4.1: PECVD silica deposition process parameters.

The process summarized in Table 4.1 was used for silica deposition. The RF generated plasma provides energy to the SiH_4 and N_2O to decompose and form SiO_2 and by-products. N_2 is used to strike and maintain the plasma in the chamber.

4.10 Dry Etching

Dry etching techniques involve energetic ion beam or plasma-driven chemical reactions to remove selected parts of a semiconductor material. Dry etching is widely used in semiconductor fabrication processes, especially for small structures, due to its properties like high resolution, anisotropic etching (no undercuts) and better dimensions control. Dry etching can be physical or chemical in nature. Physical dry etching processes involve momentum transfer from high energy moving ions to the atoms of the target materials to physically knock out the atoms of the material. Widely used physical etching involves ion-milling and sputtering. In chemical etching, the plasma contains chemically reactive ions, electrons and free radicals such as Chlorine or Fluorine. Free radicals are atoms that have unpaired electrons

and hence they are highly reactive. These reactive species reacts at the surface of the target material. Typically, Chemical etching involves the following three main steps [20]:

- Absorption of reactive species on target material surface.
- Occurrence of chemical reaction.
- Desorption of by-products.

Figure 4.10 shows the basic steps involved in the RIE dry etching process [21]. Pure chemical etching results in high isotropic side wall profiles and is not suitable for etching of small features like DBR gratings. Both the chemical and physical etching can be utilized simultaneously to get high level of anisotropic etched profiles. In this process, the material to be etched is placed in a gas discharge chamber so that it is subjected simultaneously to both high energy ions bombardment and highly reactive chemical species. This process is known as reactive ion etching (RIE). The RIE etching process combines both physical and chemical etching, i.e. plasma generated non-reactive and reactive ions. High energy non reactive ions bombardment weakens the surface chemical bonds of the target material and increase the rate of chemical reaction [20]. High energy non-reactive ions also contribute to desorption of the chemical reaction by-products.
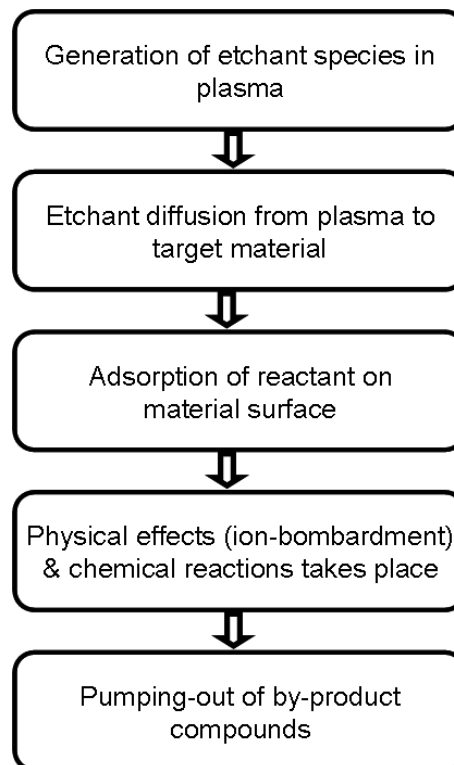
Figure 4.10: Process flow of RIE etching process.

Further, the high energy ions travel perpendicular to the target material surface resulting in anisotropic etching of the side walls. This RIE process results in etch rates, which are much higher than the sum of both chemical and physical etches.

4.10.1 RIE Etching of AlGaInAs/InP

Ridge waveguides and gratings structures were defined in a 550 nm thick HSQ layer, using EBL. After the development and exposure of the sample, an HSQ hard bake process was performed to increase hard mask (HSQ) resistance to RIE dry etching. The hard-bake process was based on O_2 plasma treatment of the sample in plasma asher for 15 minutes at an RF power of 80 Watts. This process has no effect on air-slot to grating-tooth ratio and resulted in negligible (below 1%) reduction in HSQ thickness. This process was developed by a colleague, Dr Rafal Dylewicz and reported in [22]. The HSQ mask layer was utilized to simultaneously etch the ridge waveguides and gratings structures. In the past, two different chemistries have been used in RIE dry etching of the InP material system. They include halogen related chemistries, mostly based on Chlorine (Cl) and Bromine (Br) gasses and hydro-carbon related chemistries, based on CH_4/H_2 and C_2H_6. Chlorine based dry etching of the InP material systems have high etch rates and results in better sidewall profiles. However, it has the following disadvantages:

- Produces corrosive and toxic by-products.

- High temperature (150-200 ℃) is required to remove low volatile etch by-products.

- Low volatility of some etch by-products causes rough etched surfaces.

- Higher erosion of masking material.

The use of hydro-carbon related chemistry to etch the InP based semiconductor materials was first time proposed by Hayes et al. in 1989 [23]. The drawbacks associated with methane based etching include chamber contamination, which requires periodic cleaning of chamber. Methane based chemistries are quite useful when vertical side wall profiles and lower waveguide undercuts are required. The hydrocarbon by-products of the Methane forms polymers, which reduces the waveguide undercut and protect the ridges sidewalls from etch induced damage [16]. Furthermore, Methane-hydrogen (CH_4/H_2) plasma can also be used for other materials like InGaAsP, InGaAs and GaAs. However, the etch rates may vary for

different materials. For CH_4/H_2 based etching, the following main chemical reactions occur in the chamber:

$$e^- + CH_4 \longrightarrow CH_3 + H + e^-$$
$$e^- + H_2 \longrightarrow 2H + e^-$$
$$3CH_3 + 3H + InP \longrightarrow In(CH_3)_3 + PH_3$$
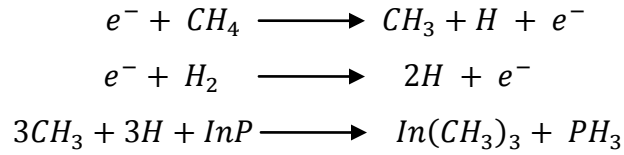
Equation 4.1

The dependence of the etch rate on the process parameters is given below [24]:

- Increasing RF power causes increase in etch rate due to increase in physical and chemical RIE etching. Too high RF power causes unwanted surface roughness.

- Increasing the chamber pressure causes increase in etch rate and also polymer deposition rate.

- Increasing gas flow rate results in increased etch rates and polymer deposition.

- The dependence of etch rate on process temperature is negligible.

The main issue related to this type of etching is the formation of hydrocarbon polymers on the material surface, which limits the etching rate. To address this issue, Oxygen (O_2) is added to the chamber, which helps in removal of hydrocarbon polymers and also produces vertical etched sidewall profiles. A vertical profile of etched side walls largely depends on mask erosion during etching of the sample.

K. Shinoda et al. [25] reported that highly selective etching of InGaAlAs/InP material can be achieved using $CH_4/H_2/O_2$. During RIE dry etch process, the presence of O_2 in $CH_4/H_2/O_2$ oxidizes the Aluminium (Al) containing dry etch stop layer, forming Aluminium oxide (Al_2O_3) film. The Al_2O_3 film prevents etching of the core layer and therefore, strongly decreases the etching rate of the sample. This reduction of etch rate due to formation of Al_2O_3 can be utilized for over etching of the sample.

According to epilayer structure, given Section 4.5, an optimized etch depth of around 1.92 μm was required for the devices fabricated in this work. A device schematic with etched ridge waveguide and grating structures is shown in Figure 4.11. For etching the AlGaInAs/InP material system in this work, a ET340 (RIE) machine was used with the standard process parameters, suggested by the dry-etch laboratory technicians. These parameters are given in Table 4.2.
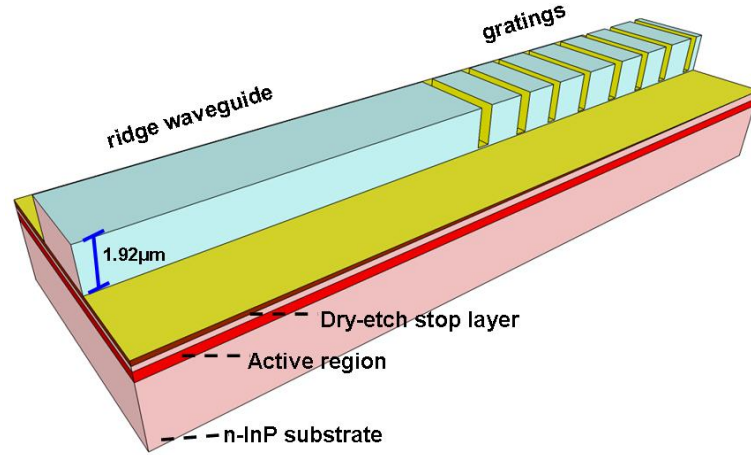
Figure 4.11: Schematic of a 1.92 μm etched ridge waveguide and surface etched gratings.

The ridge waveguide height of these devices was measured with a Dektak stylus profileometer. An interferometer tool was used for end point detection. The interferometer tool uses an in-situ laser, which is focused on the sample area to be etched and the reflected beam from sample surface is measured. The reflected beam is plotted as a function of etching time during etching process. The recorded trace of the interferometer forms cycles which corresponds to the reflectivity from each epitaxial layer being etched. Figure 4.12 (left) shows the recorded interferometeric traces of AlGaInAs/InP material during etching. As shown in the figure, the interferometeric cycles suddenly changes when the epitaxial layers above the dry-etch stop layer are completely etched. This is due to the oxidation of the Al containing dry-etch stop layer in the presence of O_2, which reduces the etch rate of the sample. An etch depth of 1.92 μm was achieved in 39 minutes using the process parameters given in Table 4.2. This gives an etch rate of 49 nm/minute. The sample was allowed to be over-etched for 3 minutes to reduce the RIE lag effects in the DBR gratings.

Gas flow($CH_4/H_2/O_2$) (sccm)	Pressure (mTorr)	RF power (W)	Temperature (ºC)	Process time (minutes)
6/54/0.16	30	50	20	45

Table 4.2: Process parameters for AlGaInAs/InP etch.

Figure 4.12 (right) shows the SEM image of etched ridge waveguide and surface etched gratings structure using $CH_4/H_2/O_2$ RIE dry etching. From this figure, it is clear that the etched gratings have almost vertical side walls with a negligibly small RIE lag effect.
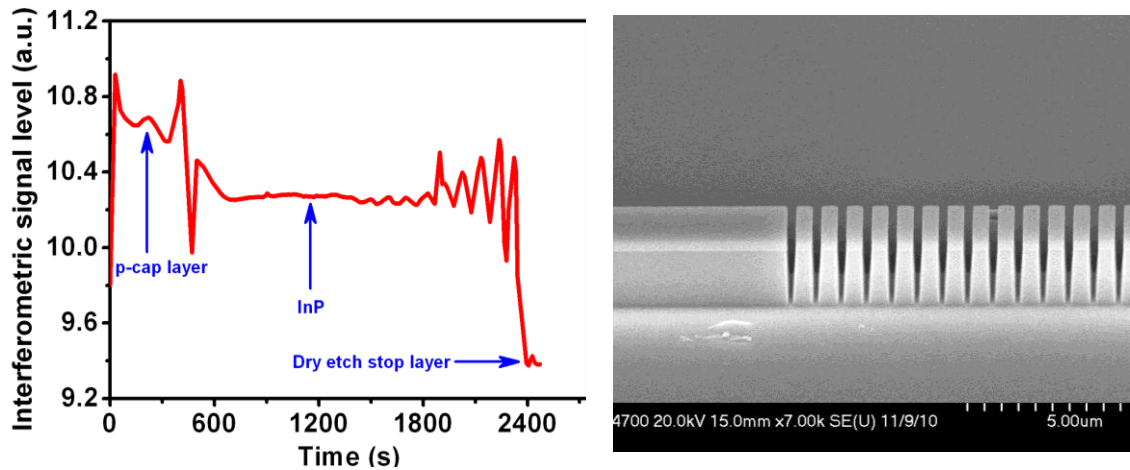
Figure 4.12: (Left) Interferometeric trace of AlGaInAs/InP material etching with ET340 machine and (Right) SEM picture of dry etched ridge waveguide and grating structures.

4.10.2 RIE Etching of SiO$_2$

SiO$_2$ etching is one of the most developed processes in the microelectronics industry. RIE (chemical-physical etching) is the most commonly used dry etch technique for etching of SiO$_2$ layers due to its properties of high anisotropic etch, high etch rates and good selectivity. The degree of etch selectivity and anisotropy depends on process parameters such as type of gases used, process pressure, radio frequency (RF) power and gas flow rates. At a given process pressure and gas flow, higher RF powers gives higher ion density and results in higher etch rates. An increase in the process pressure also causes increase in the etch rates [26]. In this work, a Plasmalab80 plus machine was used for opening the contact window in SiO$_2$ film, on the top of the ridge waveguides. Freon (CHF$_3$) and Argon (Ar) gases were used for the etching, which gives nearly vertical side-walls of the etched features. Noble gas such as Ar (a heavy gas) is added to the chamber to stabilize the plasma and help in the cooling process. The addition of Ar to CHF$_3$ significantly changes the population of reactive species in plasma, causing the etching process to be dominated by the high energy ions and thus increases the etch rate with anisotropic etched side wall profiles.

Before starting the etch run of SiO$_2$, the sample was descumed in the same machine (plasmalab80 plus) to remove any micro-masking of resists from the patterned areas, which would affect the etching of the SiO$_2$. Process parameters used for this purpose are given in Table 4.3.

Gas (Oxygen) flow (sccm)	Pressure (mTorr)	RF power (W)	Temperature (ºC)	Process time (minutes)
10	50	10	20	2

Table 4.3: Process parameters used for resist micro-mask removal.

The main chemical reactions occurring in the RIE dry etching of SiO_2 using CHF_3 and Ar are [27]:

$$e^- + CHF_3 \longrightarrow 3F + CH + e^-$$
$$4F + SiO_2 \longrightarrow SiF_4 + O_2$$
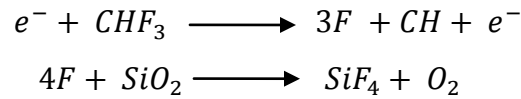
Equation 4.2

CHF_3 and Ar used in this etching process do not etch the underlying material (substrate). However, slow etching (~2-3 nm/min) of the material underneath the SiO_2 takes place after complete etching of SiO_2. This etching of the material is purely due to the sputtering of high energy ions. Process parameters used for etching SiO_2 in Plasmalab80 plus tool were optimised by the dry etch laboratory technicians. These are given in Table 4.4. The Interferometer traces were monitored during the etching process for end point detection.

Gas flow(CHF_3/Ar) (sccm)	Pressure (mTorr)	RF power (W)	Temperature (ºC)	Process time (minutes)
25/18	30	200	20	28

Table 4.4: Process parameters used for SiO_2 etch**.**

The 600 nm thick silica from the top of the ridge waveguide structures was etched in 21 minutes, which gives an etch rate of ~ 29 nm/min. The sample was over-etched for 7 minutes in order to make sure that no silica particles remain in the contact window areas.

4.11 Photoresist Removal: Plasma ashing

The removal of the photoresist mask from the sample after processes like RIE etching is one of the most commonly performed processes in device fabrication. Plasma etching of the sample results in cross linking of the resist structures, which is quite challenging to remove

with hot acetone. Conventionally, two wet chemical techniques are available for this purpose, which are as follows:

- Use of oxidizing agents such as $H_2O_2:H_2SO_4$.

- Use of chlorinated hydrocarbon mixtures such as Chlorobenzene, and Trichloroethylene.

In either case, mechanical scrubbing is often required for the removal of some residual resist particles from the sample. Furthermore, both of these wet chemical processes use corrosive chemicals. A good alternative to wet chemical processes is the use of plasma for photoresist removal. In this method, resist covered sample is placed in a chamber with an oxygen plasma, generated using RF power [20]. The energetic species of the plasma causes oxidation or burning of the resist film and thus causes removal of the photoresist. The rate of the resist removal using this technique depends on the process parameters like gas pressure, gas flow rate, applied RF power and sample temperature. Plasma ashing of the sample can be continued until the complete removal of resist as this kind of plasma ashing has no adverse effects on the underlying material of the sample.

In this work, the plasmalab80 plus (RIE) machine was used for the removal of PMMA film using plasma ashing, after the dry etch run to remove the 600 nm thick silica. The process parameters used are given in Table 4.5.

Gas (Oxygen) flow (sccm)	Pressure (mTorr)	RF power (W)	Process time (minutes)
50	50	100	15

Table 4.5: Process parameters used for plasma ashing of PMMA film.

4.12 Waveguide Planarization

The device fabrication in this work requires 1.92 µm high ridge waveguides for single mode operation. The deposition of metal electrodes is also required for current injection at the final stage of the device fabrication. The semiconductor material etching and the contact window opening (SiO$_2$ etching) results in a non-planar sample as it gets near the stage of the metal deposition. The loss of planarity causes non-uniform metallisation on the top, bottom and sidewalls of the ridge waveguides. For the devices with ridge height of 1.92 µm, and also

containing curved waveguides, it is not possible to metalise the whole sample uniformly with the e-beam metal evaporation. One way to get round to this problem is to use sputtered metal, however, sputtering causes resist lift-off problems. Furthermore, with sputtering there is a chance that the bottom of the ridge waveguides will not be adequately coated.

Figure 4.13 shows an SEM picture of a 2 µm wide and 1.9 µm deep etched waveguide with 33nmTi/33nmPt/240nmAu metallisation. The SEM picture shows uniform metal coating at the top and bottom parts of the ridge waveguide, whereas there is no metal coating on the ridge waveguides side-walls. Most of the fabricated ridge waveguide lasers, similar to the one shown in Figure 4.13 give open circuit, while others devices on the same chip with non-uniform metallisation on the side walls tend to fail when high injection current was applied to the device. This effect was supposedly to be due to the weak points of metallisation on the side walls of the ridges. This problem of the non-uniform metal coatings can be tackled using the planarization technique prior to the contact metallisation.
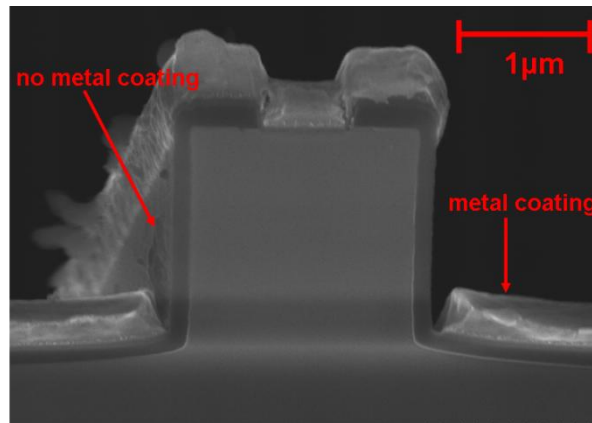
Figure 4.13: SEM picture of a metallised 1.9 µm high ridge waveguide facet.

In this work, HSQ and SiO_2 were used for planarization of ridge waveguides. Before the metal deposition, a layer of 300 nm thick PECVD silica was deposited on the sample, which was followed by 450 nm thick HSQ. To make the HSQ hard and stable, the sample was heated at 180ºC in oven for 90 minutes. Another 100 nm thick PECVD silica layer is deposited on the top. This gives total SiO_2 thickness of around 500-550 nm on the top of the ridge waveguides and around 850 nm at the bottom of the ridges, respectively. This process results in quasi-planarized ridge waveguides, which allows uniform metal coating and improved metal lift-off. Figure 4.14 shows an SEM image of a planarized ridge waveguide with contact window defined in the silica and coated with the p-contact metallisation.
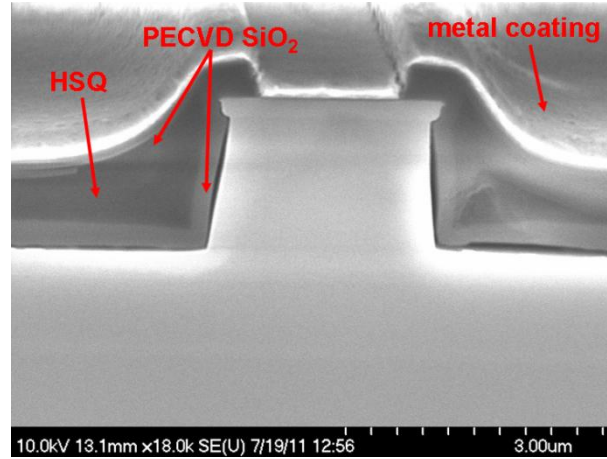
Figure 4.14: SEM picture of planarized and metallised 1.92 μm high ridge waveguide facet.

The small gaps between silica film and the semiconductor material shown in the SEM picture, was most likely induced during the cleaving of the device. Planarization of the ridge waveguides also offers a certain degree of protection to the ridge waveguides. For DBR lasers, the planarization of the ridge waveguides and DBR gratings results in reduced scattering losses due to the filling of gratings grooves with silica.

4.13 Contacts and Metallisation

Ohmic contacts play a major role in the performance of all semiconductor devices and particularly in high power lasers, which require high injection current density. When a metal and a semiconductor come into contact with each other, at thermal equilibrium, the fermi levels of the two materials are aligned at the same energy level [4]. Due to the difference between the work function of the contacted metal-semiconductor, potential barriers are formed which causes asymmetric flow of the carriers. The built-in potential at the metal-semiconductor interface is simply the difference between the work function of the metal and semiconductor. More details of this can be found in [21]. The height of the barrier, Φ_b, is the difference between the metal work function and the semiconductor electron affinity, which is given as:

$$\Phi_b = (\Phi_m - \chi)$$

Equation 4.3

where Φ_m is the work function of the metal and χ is the electron affinity of electrons.

The value of specific resistance for a heavily doped contact is given as [21]:

$$R_c \sim e^{\left[\Phi_b / \sqrt{N_D}\right]}$$

where N_D is doping concentration of the semiconductor.

Equation 4.4 shows that the specific contact resistance (Rc) strongly depends on the doping concentration (N_D). Figure 4.15 (left) shows that for lightly doped semiconductors, depletion region is wider and there is only thermionic emission of electrons across the barrier. Figure 4.15 (right) shows that for a heavily doped semiconductor, there is small depletion width and the quantum mechanical tunnelling of electrons through the barrier take place, which establishes an ohmic contact. Thus to make ohmic contacts in the devices, the material structure used in this work contains a heavily doped (1.5 x 10^{19} cm^{-3}) Zinc GaInAs layer for the p-type contact and a Silicon doped (3 x 10^{18} cm^{-3}) InP for n-type contact.
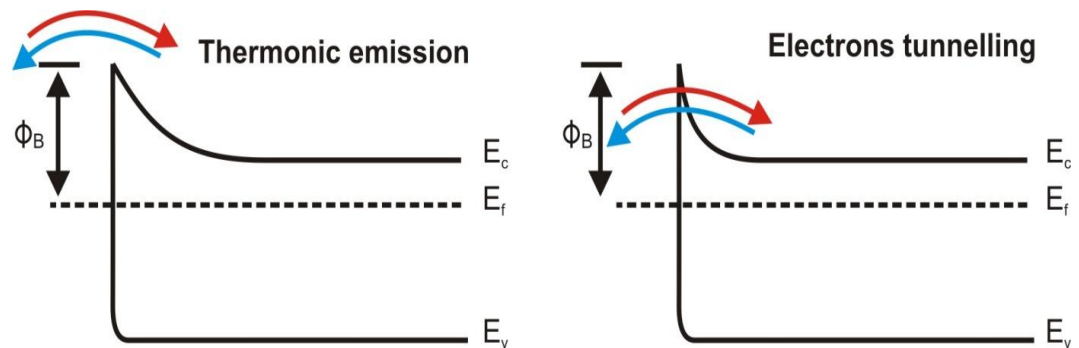
Figure 4.15: (Left) Schottky Rectifying contact: Lightly doped p-contact layer and (Right) Schottky Tunnelling Ohmic contact: Heavily doped p-contact layer [28].

Before the p-contact metallisation, the sample was treated with 1:2 mixture of hydrochloric acid (*HCl*) and water for 1 minute in order to remove the built-up oxide layer. PlassysII, a metal deposition tool was used to evaporate 33 nm Titanium (*Ti*), 33 nm Platinum (*Pt)* and 240 nm thick Gold (*Au*) on the sample for p-type contact pad. *Ti* was used because it is a reactive metal and readily oxidizes, further its adhesion properties with silica makes it a suitable choice for the p-contact coating. A layer of *Pt* (33 nm thick) was used as diffusion barrier layer, preventing the diffusion of Au into semiconductor material. A layer of 240 nm thick *Au* was used for p-contact coating due to its better sheet conductivity [4]. Similarly, for the n-contact metallisation, 14 nm Gold (*Au*), 14 nm Germanium (*Ge*), 14 nm Gold, 11 nm Nickel (*Ni*) and 240 nm Gold was deposited on the n-type InP substrate after thinning and de-oxidization of the sample in 1:2 mixture of hydrochloric acid (*HCl*) and water. Finally the

sample was annealed at 380ºC for 60 seconds in Rapid Thermal Annealing (RTA) machine to reduce the contact resistance of the device.

4.14   Ridge Waveguide Analysis

Fabry-Perot (FP) lasers with different cavity lengths were fabricated in order to characterise the novel epitaxial material, discussed in Section 4.5. The ridge waveguides of the lasers were defined using electron beam lithography and etched using $CH_4/H_2/O_2$ RIE dry etching. The waveguides were planarized using PECVD SiO_2 and HSQ, as explained in Section 4.8. A contact window was etched through the dielectric film on the top of the ridge waveguides to allow current injection to the device. The p and n metal ohmic contacts were evaporated using e-beam metal evaporators. Finally, the sample was annealed to reduce the contact resistance, cleaved into individual bars and tested.

4.14.1 Waveguide Design

The width and the height of the ridge waveguides should be designed to ensure single transverse mode operation. The 3-D simulations using beam propagation method (BPM) commercial mode solver called BEAMPROP were performed to design a ridge waveguide supporting only a fundamental transverse mode.
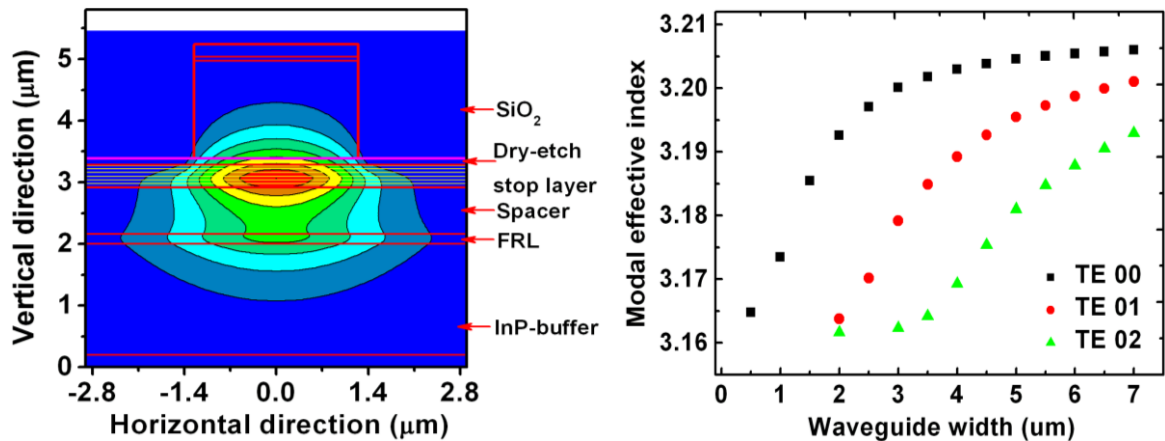
Figure 4.16: Simulation results: (Left) fundamental mode of the ridge waveguide, the red lines indicate different layers of the epitaxial structure and (Right) Modal effective index versus waveguide width for fundamental, first order and second order modes.

Figure 4.16 (left) shows the computed fundamental TE mode of a 2.5 μm wide and 1.92 μm high ridge waveguide. The SiO_2 used for planarization of the ridge waveguides was taken into

account in the simulations. The effective modal index for the fundamental, first order and second order TE modes as a function of waveguide width for 1.92 μm high ridges was computed as shown in Figure 4.16 (right). The fundamental transverse mode cuts-off at the waveguide width of 2 μm. All the higher order modes below the cut-off waveguide width are not supported by the waveguide.

4.14.2 Device Results

The ridge waveguide lasers with ridge width of 2.5 μm and height of 1.92 μm were fabricated for single mode operation of the devices. The fabricated devices were mounted p-side up on brass sub-mounts using conductive epoxy and placed on a copper heat sink with the temperature controlled at 20°C. Continuous wave (*CW*) current conditions were used for characterisation of these devices. The cavity lengths (*L*) of the lasers used to characterise the material were 1200 μm, 1700 μm and 2200 μm. The light-current (*L-I*) characteristics were measured for each device and the external quantum efficiency (η_{ext}) was calculated from the slope of the *L-I* curve. The internal quantum efficiency (η_{int}) was obtained by plotting *1/ ηext*, versus *L* as shown in Figure 4.17. From the intercept of the linear fit of the data shown in the plot, η_{int} was calculated to be 86 %. The internal losses (α_i) were calculated using Equation 4.5 [29]:

$$\frac{1}{\eta_{ext}} = \frac{1}{\eta_{int}} + \frac{\alpha_i}{\eta_{int} ln\,(R)}\,L$$

Equation 4.5

For 1200 μm long lasers, the internal losses were calculated to be 4.8/cm. The threshold current density for infinite length (J_∞) was obtained from the plot of *ln (Jth)* versus *1/L*, using Equation 4.6:

$$ln(J_{th}) = ln(J_\infty) + \frac{L_0}{L}$$

Equation 4.6

From the linear fit of the data shown in Figure 4.17, and using Equation 4.6, the value of J_∞ was found to be 550 A/cm^2. The results obtained in this Section compare well with results obtained from ridge waveguide lasers based on Aluminium quaternary epitaxial structure, reported in [30] and shows that the material is of good quality.
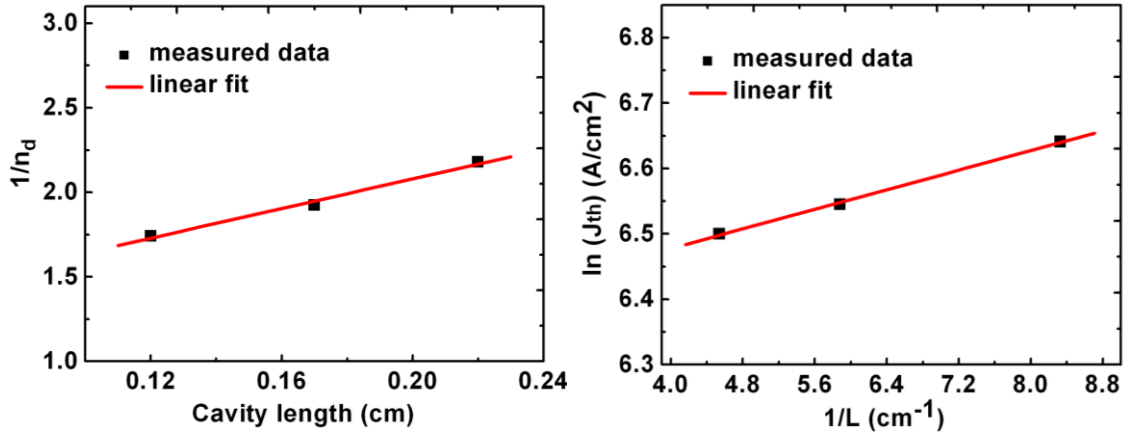
Figure 4.17: (Left) Plot of $1/\eta_{ext}$ versus L, η_{int} calculated from the y-intercept of this plot and (Right) plot of ln (J_{th}) versus $1/L$, J_∞ is calculated from the y-intercept of this plot.

4.14.3 Far-field Results

The angular spread of a laser mode is indicated by the far-field pattern and thus quite important in determining the coupling efficiency and coupling tolerance between a laser and a single-mode fiber. Conventional epitaxial structures results in large beam divergence angle and asymmetric profiles of the far-field patterns [10]. As explained earlier, to reduce the divergence angles, a FRL was inserted in the n-cladding layer of the modified epitaxial structure, which expands the near-field in the vertical direction towards the n-cladding layer side. The increase in the near field pattern in the vertical direction causes reduction in the corresponding far-field through Fourier transformation. The modelling of the farfield pattern for the 3-QW devices was performed using 3-D beam propagation method (BPM) simulations. The simulated far-field pattern of the 3-QW device is shown in Figure 4.18.
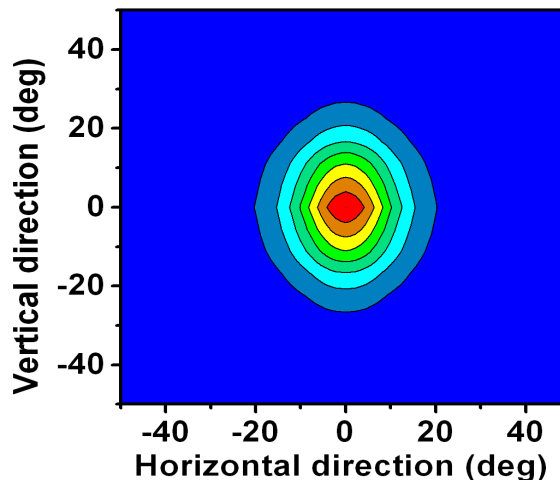
Figure 4.18: Far-field simulated using the 3-D *BPM* simulation.

The simulation results shows that for 1.92 μm high and 2.5 μm wide ridge waveguides, the divergence angle in the horizontal direction is 22°, while that in vertical direction is 28°.

After the fabrication and mounting the ridge waveguide lasers, the far-field pattern was measured at around 5 mm away from the device facet. The experimental set-up used to measure the farfield of these devices is shown in Figure 4.19. As shown in the figure, the device was mounted on a *Cu* heat sink with the temperature controlled at 20°C and devices driven with CW current.
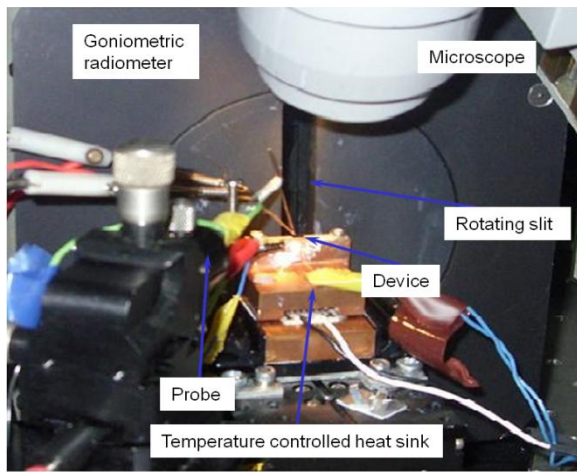
Figure 4.19: Schematic of far-field measurement setup.

The devices were placed in front of the rotating slit so that the light emitted from the device is collected and the beam intensity as function of angular position was measured. The 2-D picture of measured far-field is shown in Figure 4.20. This Figure shows that the output is centred, single moded and nearly symmetric.
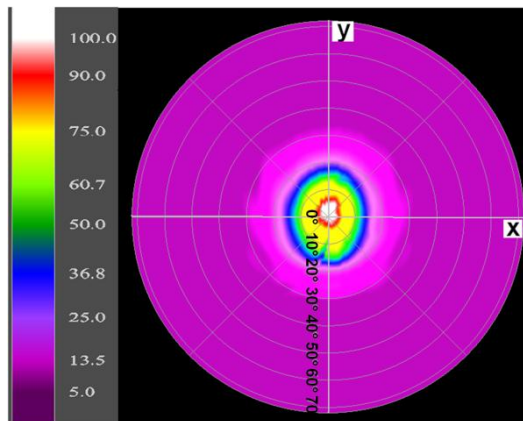
Figure 4.20: 2-D picture of the measured far-field pattern at I_{gain} = 70 mA. The intensity scale is shown on the left.

The measured results of the far-field profiles in the horizontal and vertical directions for different injection currents are given in Figure 4.21. These results show that the divergence angles in the horizontal and vertical direction are 22° and 26°, respectively, which are consistent with the simulation results. Comparing to the devices based on conventional epitaxial structures, given in Chapter 5, the reduction of the divergence angle in vertical direction is due to the improved waveguide design. The small features observed in Figure 4.21 (right) at around -20° is due to the measurement equipment·
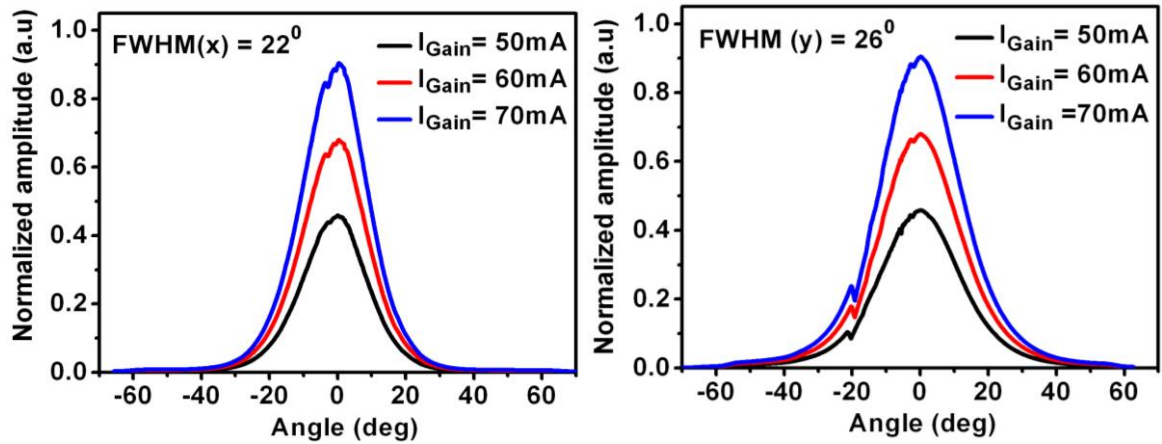
Figure 4.21:.Measured far-field patterns in (left) horizontal and (right) vertical directions for different gain currents·

4.15   Contact Performance Analysis using Transfer Length Method

In order to assess the performance of the p-type ohmic contacts, the transfer length method (TLM), also known as transmission line method was used. The patterns for the TLM measurements were planar contacts on the semiconductor material with the contacts width (W) and varying gaps (x) between the consecutive contact pads. The contact pads for TLM measurements were prepared using photolithography and a metal contact pad (33 nm Ti/33 nm Pt/240 nm Au) was evaporated. Finally, the sample was annealed at 380°C for 60 seconds.

The TLM pattern had five contact pads, each 800 μm long and 200 μm wide. The gap between the two consecutive pads was (left to right) 12.2 μm, 17.2 μm, 22.2 μm and 27.2 μm as shown in Figure 4.22. The samples were measured using four-probe technique, where the voltage is applied across the contact pads and the current flow from one contact to another is measured. The resistance *(R)* between the two consecutive contact pads is given by [4]:

$$R = 2\,R_c + \frac{R_{sh}}{W}\,x$$

where R_C is the contact resistance, R_{sh} is the semiconductor sheet resistance, and x is the width of the gap between two contact pads.
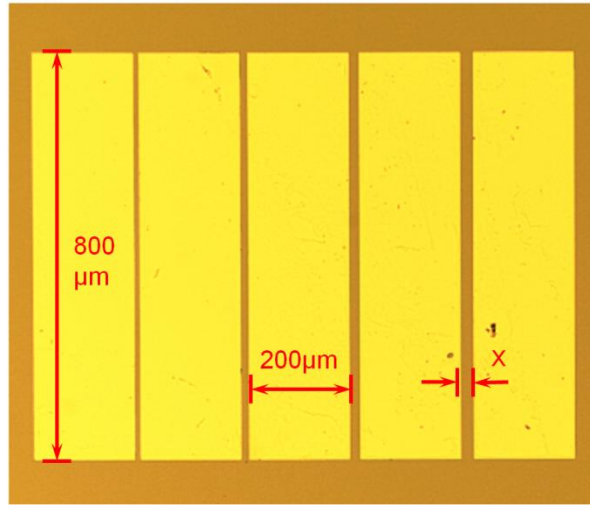
Figure 4.22:.Optical microscope image of the fabricated TLM patterns.

Contact resistance can be calculated by measuring the total resistance of the two separate ohmic contacts and excluding the sheet resistance of the semiconductor material. The R_C can be found from the y-intercept of the resistance versus contacts gap plot. Similarly, the slope of the resistance versus contacts gap plot is equal to $\frac{R_{sh}}{W}$, therefore one can determine the R_{sh} which is assumed to be the same between and under the contact pads. The transfer length (L_t) is given by [31]:

$$L_t = \frac{R_c W}{R_{sh}}$$

The specific contact resistance indicate the resistance of the metal-semiconductor interface and is given by:

$$\rho_c = R_{sh} L_t^2$$

Figure 4.23 shows the plot of resistance and pad separation of different contact pads of the *TLM* patterns.
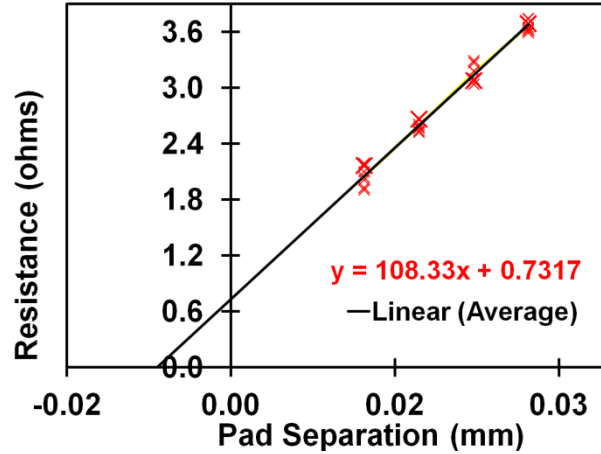
Figure 4.23:.Measured resistance versus contact pad separation of TLM patterns.

From the linear extrapolation of the data points shown in Figure 4.23, the following parameters were calculated.

Contact resistance R_c (Ω)	Sheet resistance R_{sh} (Ω)	Transfer length L_t (mm)	Specific resistance ρ_c(Ωmm^2)
3.658 x 10^{-01}	8.666 x 10^{+01}	3.377 x 10^{-03}	9.884 x 10^{-04}

Table 4.6: TLM measurement results.

The results shown in Table 4.6 compares well with results reported in [4], and therefore indicate that these p-type ohmic contacts are suitable for devices in this research work.

4.16   Chapter Summary

This chapter briefly discussed the basic introduction of the QW lasers and the properties of AlGaInAs/InP MQW epitaxial material. The design of the epitaxial material used for fabrication of devices in this work was explained. This material was based on the standard commercially available five QW active region AlGaInAs epitaxial material. The number of number of QWs in the active region were reduced from five to three and an optimized FRL layer was inserted in the n-cladding layer, which results in increased mode spot size and thus reduced far-field. The comparison of results obtained from the devices based on both five and three QW active region materials is given in the Chapter 5. The fabrication tools and techniques employed in this work were presented. Basic parameters of the e-beam lithography with the properties of positive and negative resists were discussed. The importance of

proximity correction for writing sub-micron features such as DBR gratings was briefly discussed. To reduce HSQ mask erosion during the dry etching process, an HSQ hard-bake process was performed in the presence of O_2 plasma. Next, the dry etch techniques used in this work were discussed. Recipes used for RIE dry etching of SiO_2 and AlGaInAs/InP material were presented. Ridge waveguide planarization technique using SiO_2 and HSQ was used for uniform p-metal coating. Using the well controlled fabrication tools and the optimized process parameters, devices with sub-micron features like the DBR grating were successfully fabricated.

Simulations and measurement results obtained from the ridge waveguide lasers were presented. Several material parameters such as internal efficiency, internal losses and infinite threshold current density were calculated. There parameters demonstrate that the material is of good quality. The simulated and measured far-field pattern of the device based on the three QW material structure showed reduced divergence angles as compared to the device based conventional epitaxial structure.

4.17   References

1.   G. P. Agrawal and N. K. Dutta, *Long-wavelength semiconductor lasers*, Van Nostrand Reinhold, New York, 1986.

2.   Prakash Koonath, et al., *Polarization-Insensitive Quantum-Well Semiconductor Optical Amplifiers.* IEEE Journal of Quantum Electronics, 2002. 38(9).

3.   Friedrich Bachmann, Peter Loosen, and Reinhart Poprawe, eds. *High power diode lasers; Technology and applications*. 2007, Springer.

4.   Steven McMaster, *Monolithically Integrated Mode-Locked Ring Lasers and Mach-Zehnder Interferometers in AlGaInAs*, in Department of Electronics and Electrical Engineering. 2010, University of Glasgow: UK.

5.   Michael J. Conelly, *Semiconductor Optical Amplifiers*. 2002: Kluwer Academic Publishers, New York.

6.   S. Selmic.; T. Chou.; J. Sih.; B. Kirk, A.M., ; J. Butler,; D. Bour,; and G. Evans, *Design and characterization of 1.3-um AlGaInAs-InP multiple-quantum-well lasers.* IEEE Journal of Selected Topics in Quantum Electronics. 2001. 7(2): p. 340-349.

7.   Lianping Hou, et al., *Subpicosecond Pulse Generation at Quasi-40-GHz Using a Passively Mode-Locked AlGaInAs–InP 1.55 Strained Quantum-Well Laser.* IEEE Photonics Technology Letters, 21(23): p. 1731-1733.

8.   Lianping Hou, et al., *Low divergence angle and low jitter 40 GHz AlGaInAs/InP 1.55 μm mode-locked lasers.* Optics Letters, 2011. 36(6): p. 966-968.

9.   D. Garbuzov, et al., *1.5um wavelength, SCH-MOW InGaAsP/lnP broadened-waveguide laser diodes with low internal loss and high output power.* Electronics Letters, 1996. 32(78).

10.   Bocang Qiu, et al., *Design and Fabrication of Low Beam Divergence and High Kink-free Power Lasers.* IEEE Journal of Quantum Electronics, 2005. 41(9): p. 1124-1130.

11.   Lianping Hou, et al., *AlGaInAs/InP Monolithically integrated DFB Laser Array.* Journnal of Quantum Electronics, 2011. 48(2): p. 137-143.

12.   Razeghi. M, *Technology of Quantum Devices*. 2010: Springer.

13.   Stephen Thomas, *Electron beam lithography course notes.* 2008 University of Glasgow, UK.

14.   Giuseppe Tandoi, *Monolithic High Power Mode Locked GaAs/AlGaAs Quantum Well Lasers*, in School of Engineering. 2011, University of Glasgow: UK.

15.   Ren, L., *Proximity effect in electron beam lithography.* 7th International Conference on Solid-State and Integrated Circuits Technology 2004. vol.1: p. 579-582.

16.   Gabor Mezosi, *Semiconductor Ring Lasers for all-optical signal processing* in School of Engineering. 2010, University of Glasgow UK.

17.   L. O. Faolain, et al., *Fabrication of photonic crystals using a spin-coated hydrogen silsesquioxane hard mask*. vol. 24. 2006: AVS. 336-339.

18.   Chang-Chung Yang and Wen-Chang Chen, *The structures and properties of hydrogen silsesquioxane (HSQ) films produced by thermal curing.* Journal of Material Chemistry, 2002. 12. p.1138-1141.

19.   Antonio Samarelli, *Micro Ring Resonators in Silicon-on-Insulators*, in Department of Electronics and Electrical Engineering. 2011, UK: Glasgow.

20.   Sorab K. Ghandhi, *VLSI Fabrication Principals, Silicon and Gallium Arsenide*. 2nd Edition ed. 1994, New York John Wiley & Sons.

21.   S. M. Sze, *Semiconductor Devices-Physics and Technology*. 2002: John Wiley and Sons.

22.   R. Dylewicz, et al., *Fabrication of submicron-sized features in InP/InGaAsP/AlGaInAs quantum well heterostructures by optimized inductively coupled plasma etching with $Cl_2/Ar/N_2$ chemistry*. vol. 28: AVS. 882-890.

23.   T. R. Hayes, et al., *Reactive ion etching of InP using CH_4/H_2 mixtures: Mechanisms of etching and anisotropy.* Journal of Vacuum Science and Technology, 1989. 7(5): p. 1130-1140.

24.   David Larrson, *Fabrication and Characterization of low-noise monolithic mode-locked lasers.* 2006. Technical University of Denmark.

25.   Shinoda. K, Nakahara. K, and Uchiyama. H, *InGaAlAs/InP ridge-waveguide lasers fabricated by highly selective dry etching in $CH_4/H_2/O_2$ plasma*, in *International Conference on Indium Phosphide and Related Materials*. 2003.

26.   AK Paul, AK Dimri, and RP Bajpai, *Short Communication Plasma etching processes for the realization of micromechanical structures for MEMS. J. Indian Inst. Sci., 2001. 81: p. 669-674.

27.   D. J. Plummer, M. D. Deal, and P. B. Griffin, *Silicon VLSI Technology*. 2000: Prentice Hall.

28.   Professor   N   Cheung,   *Available   online: http://www-inst.eecs.berkeley.edu/~ee143/fa10/lectures/Lec_16.pdf*.

29.   L. A. Coldren and S. W. Corzine, *Diode Lasers and Photonic Integrated Circuits*: John Wiley and Sons, Inc.

30.   J. P. Sih, et al., *Performance of Ridge-Guide AlGaInAs Lasers*, in *SPIE vol. 3001*.

31.   H. H. Berger, *Contact resistance on diffused resistors*, in IEEE Solid state circuits conference. 1969.

Chapter 5

Mode Locked Lasers Results

5.1 Introduction

This chapter gives a detailed overview of the characterisation of mode locked lasers based on the standard 5-QW epitaxial material and the 3-QW epitaxial material with a far-field reduction layer in the n-cladding layer. This chapter begins by presenting the output power measurements of the devices based on the 5-QW and 3-QW epitaxial material, followed by an analysis of the mode locking performance. In Section 5.4, the modelling and the experimental measurement results of the distributed Bragg reflector (DBR) gratings are presented. In order to investigate the effect of DBR gratings on the performance of mode locked lasers, monolithically integrated mode locked DBR lasers were fabricated. Section 5.5 presents the results of the mode locked lasers integrated with the surface etched DBR gratings.

5.2 3-QW and 5-QW Material based Devices Comparison

As detailed in Chapter 4, the material structure chosen for fabrication of the devices in this work consists of 3 QWs active region with an optimised spacer and far-field reduction layer inserted in the n-cladding layer. The new epitaxial structure with the 3-QWs active region results in an increased spot size due to increase in A/Γ, and thus reducing the differential gain and beam divergence angles. The internal losses are also reduced due to a reduced overlap of

optical mode with the p-cladding layer. A comparison of the devices based on the standard 5-QWs and optimised 3-QWs laser materials is given in the following sections.

5.2.1 *L-I* Curves and Modal Gain

The most fundamental property of a semiconductor laser is the light-current (*L-I*) characteristic. From the *L-I* curve of a laser, the threshold current, the maximum output power and the slope efficiency can be determined. The *L-I* curves of Fabry-Perot (FP) lasers of the same cavity length (1100 µm) based on the 3-QW and 5-QW epitaxial structures are given in Figure 5.1. The figure shows that the values of threshold currents for both kinds of devices are similar, around 25 mA. The slope efficiency for the 3-QW material based FP laser is about 0.21 W/A, which is much higher than the one obtained for 5-QW material based FP lasers i.e. 0.14 W/A. From the 3-QW devices, 68 mW kink free output power is obtained, which is more than twice obtained from 5-QW laser (28 mW) of the same length.
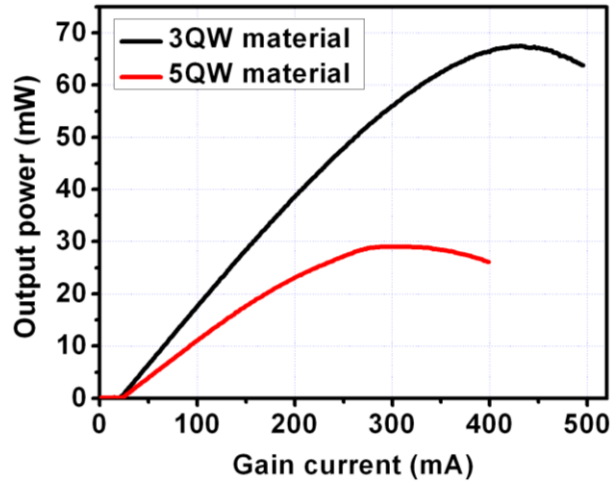
Figure 5.1: *L-I* curves comparison of the 3-QW and 5-QW materials based FP lasers.

The net modal gain of the lasers can be obtained by using well-known Hakki-Paoli gain measurement technique [1], in which the ratio of maximum intensity and minimum intensity of the amplified spontaneous emission (ASE) gives the net modal gain by using:

$$G_{net} = \Gamma g - \alpha_i = \frac{1}{L} ln\left(\frac{\gamma - 1}{\gamma + 1}\right) + \frac{1}{2L} ln\left(\frac{1}{R_1 R_2}\right)$$

Equation 5.1

where Γ is the optical confinement factor, α_i is the internal losses, $\gamma = \sqrt{\frac{I_{max}}{I_{min}}}$, L is the total length of the cavity, R_1, R_2 are mirror facet reflectivities.

The net modal gain spectra of both the 3-QW and 5-QW material based devices are given in Figure 5.2. From the net modal gain spectra, the value of α_i for the 3-QW material based devices was found to be ~ 8 cm^{-1} whereas, for the 5-QW material based devices, the value of α_i was ~ 14 cm^{-1}. The calculated value of internal losses for the 3-QW devices was 8.4 cm^{-1} [2], which shows a close agreement of the calculated and measured values. The internal losses of the devices depend on the optical confinment factor (Γ) and absorption co-efficient (k) of the optical mode in the p-cladding, active and the n-cladding layers, respectively. The values of absorption co-efficients at operating wavelength of 1.55 μm for the strained QWs material are: $k_p = 22$ cm^{-1} for the p-doping of 8.6 x 10^{17} cm^{-3}, $k_{QW} = 35$ cm^{-1} for compressively strained QWs and $k_n = 1$ cm^{-1} for the n-doping of 10^{18} cm^{-3} [3]. The higher value of k indicates that the optical absorption in the p-cladding layer is much higher than the n-cladding layer. The insertion of the 0.75 μm spacer layer and 0.16 μm far-field reduction layer in the n-cladding layer of the 3-QW epitaxial structure reduces the optical overlap with the p-cladding layer and leads to reduction in the internal losses.
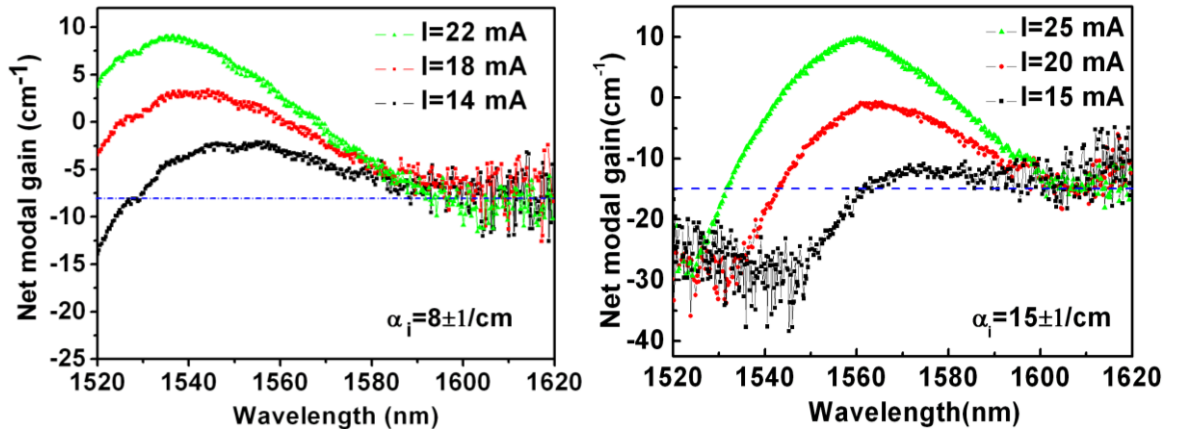
Figure 5.2: Net modal gain comparison of (Left) 3-QW and (Right) 5-QW material based FP lasers.

5.2.2   Near-field and Far-field Patterns

The optical intensity distribution pattern of light in the waveguide of the laser is known as the near-field pattern. In ridge waveguide lasers, normally the near-field pattern is large in the direction parallel to the active layer plane, while being short along the axis perpendicular to the active layer plane. The index step due to the ridge waveguide determines the near-field pattern in the direction parallel to the active layer plane, whereas in the direction perpendicular to the active layer plane, the near-field pattern is determined by the thickness and composition of different epitaxial layers used in the wafer structure design [4]. The far-field pattern is

considered to be the diffracted pattern of the near-field pattern, if the near-field pattern is regarded as a slit [5]. With the increase in the slit size, the size of the diffracted pattern decreases. The far-field indicates the angular spread of the laser mode and thus quite important in determining the coupling efficiency of the laser and the fiber. To simulate the near field pattern and far-field pattern of the 3-QW and 5-QW active region based lasers, respectively, 3-D beam propagation simulations were carried out with commercially available software, BeamPROP.
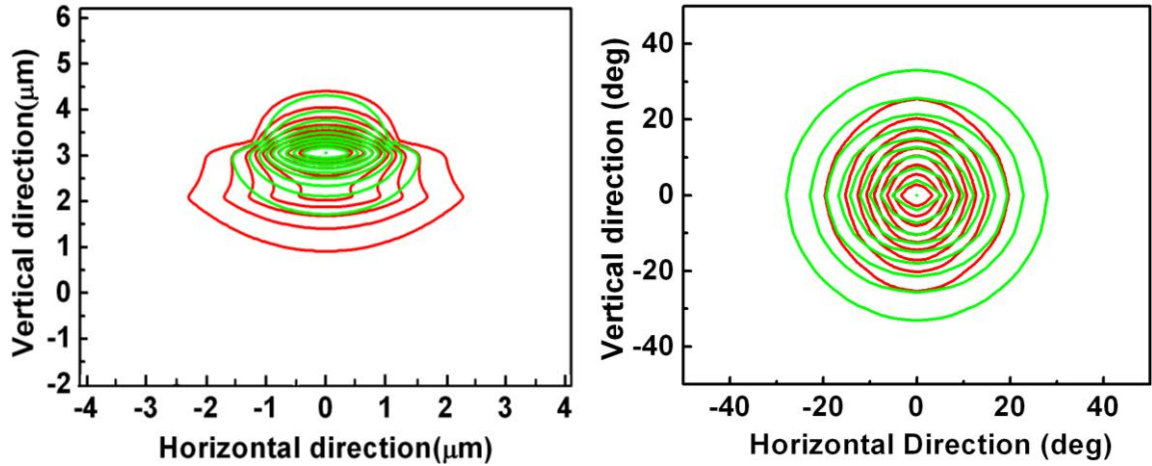
Figure 5.3: Simulation results: (Left) near field pattern of the 3-QW (red lines) and 5-QW (green lines) laser. (right) far-field pattern of the 3-QW (red lines) and 5-QW (green lines) laser. Each line from the centre represents 12% decrease in the intensity.

The simulated near-field of the 3-QW device (red lines) given in Figure 5.3, is larger than that of the 5-QW device (green lines), where each line from the centre represents a 12% decrease in the intensity. The increase of the near-field of the 3-QW devices is due to the waveguide design as discussed in Chapter 4 (Section 4.5). Due to the insertion of the far-field reduction layer in the n-cladding layer, the near-field pattern is expanded towards the n-cladding layer. From the figure, the simulation results of the far-field of the 3-QW device (red lines) in the horizontal direction is 22°, while in the vertical direction it is 28°, and the far-field pattern of the 5-QW device (green lines) is 29° and 34° in the horizontal and vertical directions, respectively.

The measured far-field of the FP lasers based on 3-QWs and 5-QWs, respectively, are shown in Figure 5.4. The far-field of these devices was measured by using the same experimental setup shown in Chapter 4 (Section 4.14.3). The divergence angle for 3-QW devices in the horizontal direction is 23° and in the vertical direction its value is 26°, whereas for 5 QW

devices, the far-field in horizontal direction is 34° and in vertical direction it is 35°. The reduction in divergence angles of the devices based on the 3-QW material as compared to the devices on the 5-QWs material, is due to the epitaxial structure with FRL in the n-cladding layer [6]. The simulation and the measurement results of the far-field are slightly different which is likely to be due to the trapezoidal like shape of the ridge waveguides as shown in the SEM picture of the ridge structures, given in Chapter 4 (Figure 4.14).
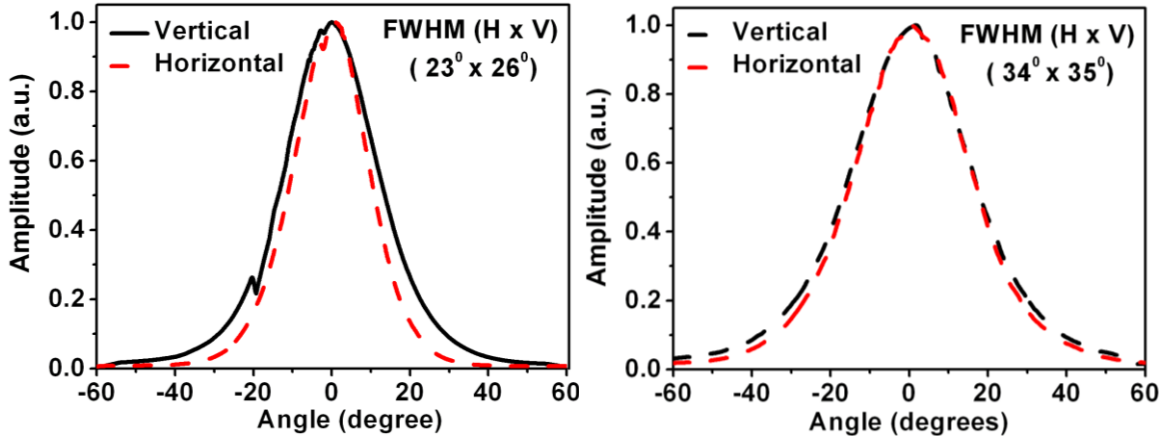
Figure 5.4: Measured far field patterns of (Left) 3-QW FP laser and (Right) 5-QW FP lasers in the horizontal and vertical directions respectively.

5.3 Characterisation of Mode Locked Lasers

As discussed in Chapter 3, passively mode locked lasers (MLLs) with the gain and saturable absorber section were characterized by forward biasing the gain section, and reverse biasing the absorber section. DC probes were used for injection of current and voltage to the gain and the absorber sections, respectively. A thermo-electric cooler (TEC) was used to control the temperature of the copper heat sink at a constant temperature of 20°C. Furthermore, thermo-conductive paste was applied in the interface between the brass sub-mount and the copper heat sink to improve the thermal conductivity between the devices and the heat sink. The output light from the device was collected using a single mode lensed fibre, which was connected to the measurement equipment via an optical isolator. The total length of these devices were 1080 µm, with a 1040 µm long gain section, 25 µm long saturable absorber (SA) section, and 15 µm wide gap between these two sections.
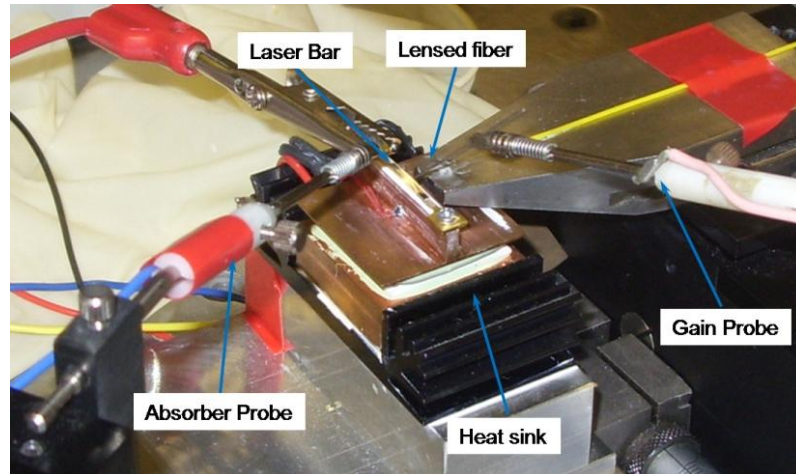
Figure 5.5: Photograph of mode locked lasers mounted on a copper heat sink for testing.

The mode locking performance of these devices was fully characterised in three main steps: measurement of the optical spectra, the RF spectra, and second harmonic generation (SHG) intensity autocorrelation. The results from each of these measurements with the experimental setups will be explained in the following sections.

5.3.1   Optical Spectra Measurements

To measure the optical spectra of these devices, the output light from the MLLs was coupled into an optical spectrum analyser (OSA) through a single mode lensed fiber. An inline optical isolator was used to prevent any back reflections into the cavity. The schematic of optical spectra measurement setup is shown in Figure 5.6.

Figure 5.6: Schematic of experimental setup for optical spectra measurements.

Typically in the mode locking regime of a laser, the 3 dB bandwidth of the optical spectrum broadens due to several longitudinal modes contributing to the output of the laser. The mode spacing of the cavity modes can be determined from high resolution measurement of the optical spectra. Normally, for MLLs operating near 1.55 μm wavelength, the mode spacing is around 0.32 nm for repetition frequency of around 40 GHz.
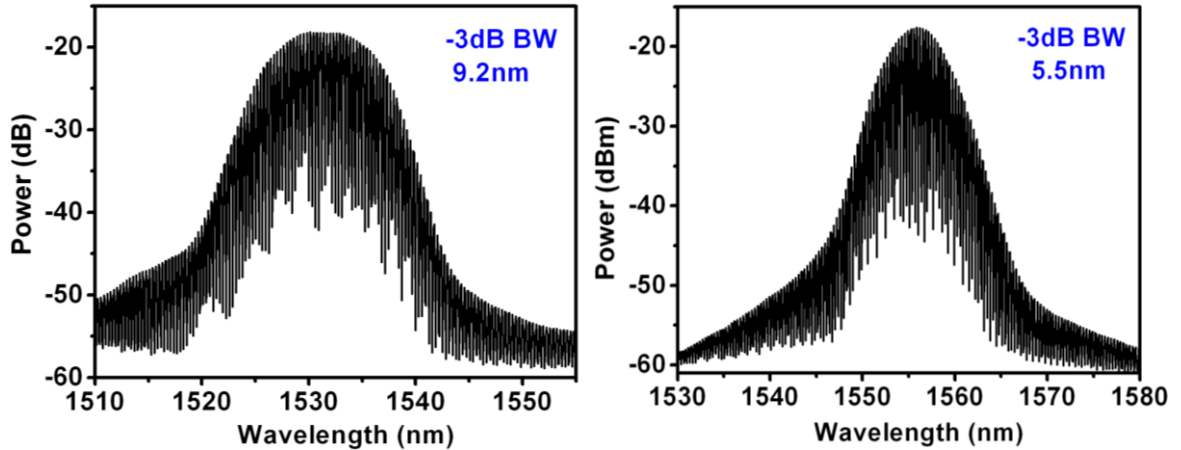
Figure 5.7: Measured optical spectra under the mode locking conditions from (Left) 3-QW MLLs at I_g = 60 mA and V_{SA} = -3 V and (Right) 5-QW MLLs at I_g = 72 mA and V_{SA} = -3 V.

The optical spectra of the 3-QW and 5-QW MLLs, respectively under the optimal mode locked conditions are shown in Figure 5.7. The optical spectrum was measured with a resolution bandwidth of 0.06 nm, which was limited by the optical spectrum analyser. The 3 dB bandwidth of the optical spectrum of 3-QW MLL is 9.2 nm, with the peak wavelength at 1532 nm, while that of the 5-QW MLL is 5.5 nm, with the peak wavelength centred at 1556 nm. The difference in the peak wavelength of the devices fabricated using the 3 and 5 QW materials is likely to be due to the growth of the wafers at different times, resulting in inconsistencies in the epitaxial layer heights and material doping. In both cases the optical spectrum is symmetrical with the mode spacing of around 0.32 nm, which corresponds to around 40 GHz pulse repetition frequency. The 3 dB bandwidth of the optical spectrum indicates the number of modes locked in phase and is inversely related to the temporal pulse width from the device. For transform limited output, a ~ 67 % larger 3 dB spectral bandwidth of the 3-QW MLLs suggests narrower optical pulses compared to 5-QW MLLs. However, due to additional chirp on the shorter pulses, the pulse duration of the pulses emitted from the 3-QW MLLs would not be 67 % shorter than that obtained from the 5-QW MLLs [7].

5.3.2   RF Spectra Measurements

The radio frequency (RF) spectrum of the MLLs confirms the mode locking operation of the devices. The RF spectrum shows the repetition rate of the mode locked laser, which is determined by the round trip time in the cavity. The RF spectrum provides information of mode locking, repetition frequency stability and timing jitter. The RF spectra of the devices in this work were measured by coupling the laser output through a lensed fiber into an inline

optical isolator and high frequency photodetector, which was connected to an RF spectrum analyser. The schematic of the experimental setup used for measuring the RF spectra is shown in Figure 5.8.
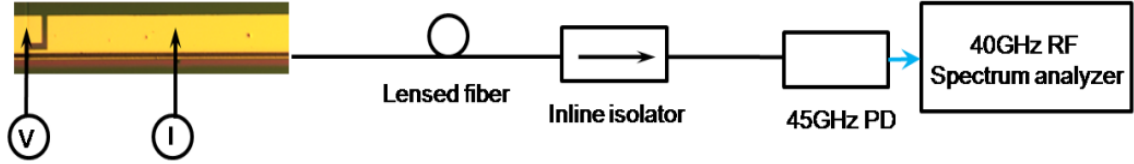
Figure 5.8: Schematic of experimental setup for RF spectra measurement of the MLLs.

A high frequency photodetector was used to convert the optical signal into an electrical signal. The bandwidth of the photodiode was 45 GHz. According to the literature, stable mode locked operation occurs when the peak of the RF spectrum at the fundamental frequency is at least 25 dB above the noise floor or the relaxation oscillation peak [8]. The devices are said to be self pulsating if the energy of the pulses are unstable. During self pulsation, the lasers usually emits broad temporal pulses with a repetition frequency less than cavity round trip repetition rate and is related to the carrier lifetime in the gain section of the device [9]. It is also possible that the MLL operates in a regime where both the self-pulsation and mode locking co-exists [10]. Therefore, the RF spectra of these devices were measured for both a wide span, i.e. 0-40 GHz (limited by RF spectrum analyser) and a 50 MHz span around the repetition frequency of the device. Figure 5.9 shows that for the 3-QW MLL and 5-QW MLL the fundamental frequency of mode locking is 39.75 GHz and 39.65 GHz, respectively. The RF peak of the 3-QW MLL and 5-QW MLL is 40 dB and 35 dB above the noise floor, respectively. The full range RF spectra of both the 3-QW and 5-QW MLL shows stable mode locking with no low frequency components. The 3 dB linewidth of the RF spectrum by fitting the Lorentzian fit for the 3-QW MLLs is found to be 130 kHz, whereas, for the 5-QW MLLs its value is 900 kHz. The narrower RF spectrum of the 3-QW MLLs as compared to the 5-QW MLLs is due to the reduced amplified spontaneous emission (ASE) coupling to the optical modes. [11]. This is caused by the low optical confinement factor due to reduced number of QWs in the active and lower internal losses of the cavity due to the repositioning of the optical mode.
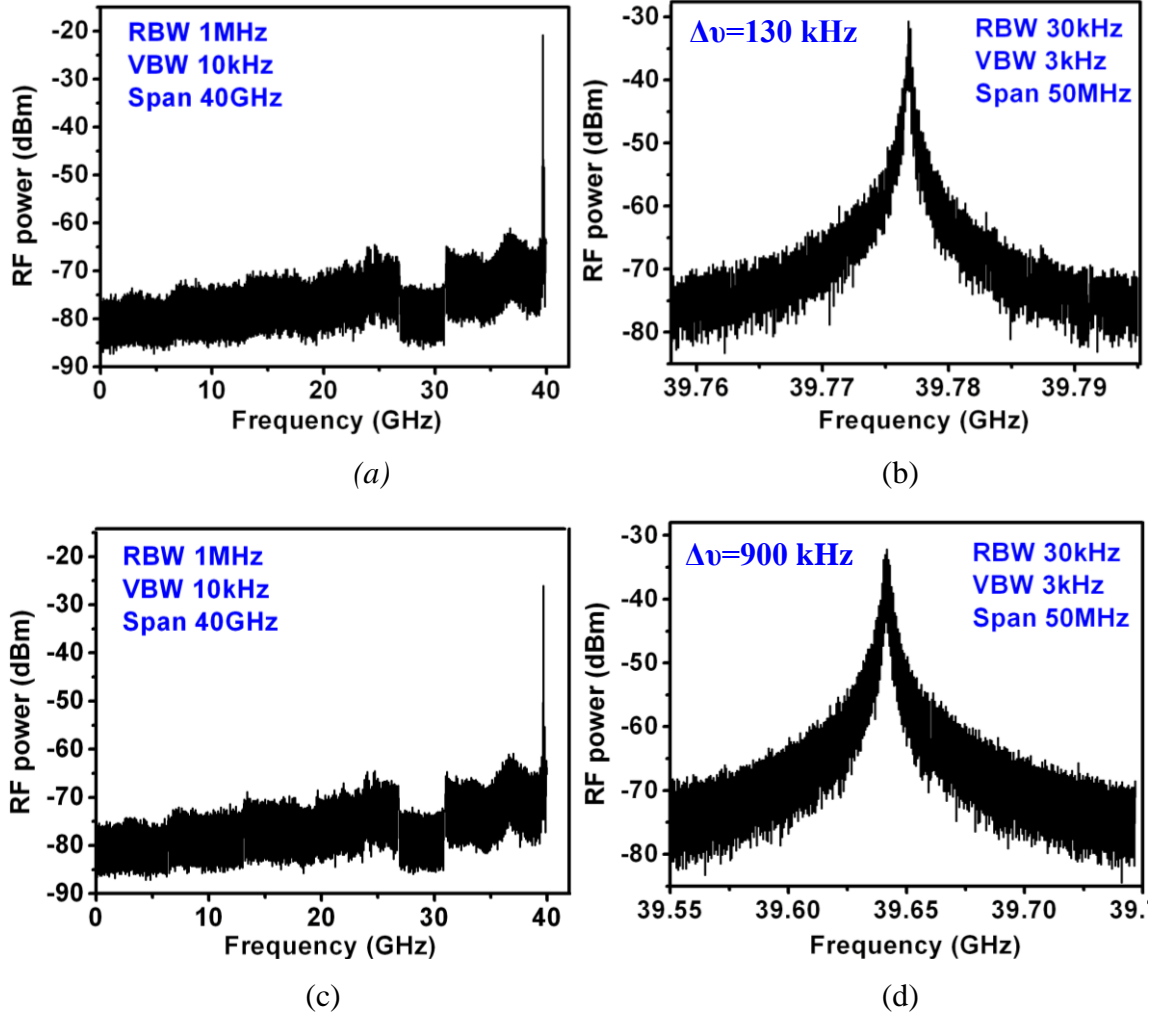
Figure 5.9: Measured RF spectra under the optimal mode locking conditions: (a) and (b) shows the full range and zoomed RF spectrum of the 3-QW MLL, respectively, for I_{gain} 60 mA and V_{SA} -3 V, whereas (c) and (d) show full range and zoomed RF spectrum of 5-QW MLL, respectively, for I_{gain} 72 mA and V_{SA} -3 V.

The timing jitter of the MLLs is related to the RF linewidth as described by the following relation [12]:

$$\delta_T^i(f_u, f_d) = \frac{T_R\sqrt{\Delta v_{RF}}}{2\pi^{3/2}} \sqrt{\frac{1}{f_d} - \frac{1}{f_u}}$$

Equation 5.2

where δ_T^i is the integrated root-mean square (RMS) timing jitter, T_R is the pulse train period, Δv_{RF} is the linewidth of the RF spectrum, f_u and f_d are the upper and lower frequencies of integration, respectively. The RMS timing jitter was calculated over an offset frequency range of 4 MHz to 80 MHz, the 3-QW MLLs gives an RMS jitter of 5.7 ps, which is considerably smaller than the 15 ps jitter, measured from the 5-QW MLLs.

5.3.3   Pulse Width Measurements

Pulse durations in the sub 10 ps range cannot be measured using the conventional photodetector-oscilloscopes, due to the limited available bandwidth of the electronics. The most common method for measuring the pulses < 10 ps is by using the non-linear intensity autocorrelation technique. The autocorrelation technique involves the interaction of a pulse with a delayed replica of itself in a non-linear media [13]. The schematic of measurement setup for characterizing optical pulses of a MLL is shown in Figure 5.10**.**
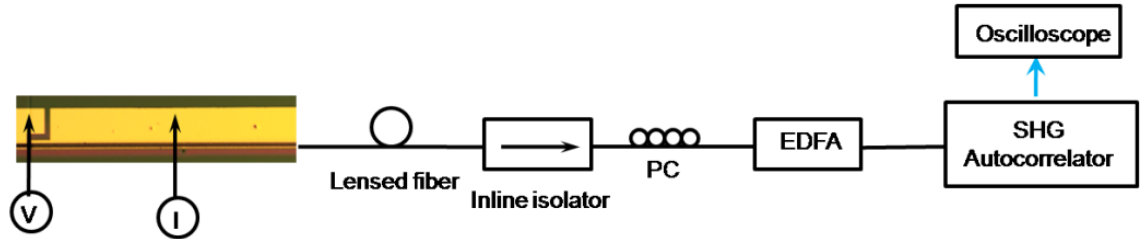
Figure 5.10: Schematic of experimental setup for optical pulse characterisation of MLLs.

The pulse train generated by the MLL was coupled from the device into a single mode fiber and through an optical isolator, a polarization controller, a dispersion shifted erbium doped fiber amplifier (EDFA) and then sent into a second harmonic generation (SHG) intensity autocorrelator. A dispersion shifted EDFA was used to minimize the pulse dispersion while propagating through the lengthy erbium doped fibre, which would otherwise obscure the actual pulse width emitted from the laser. A polarization controller adjusts the polarization of the pulse train while the EDFA increases the output power, which is required for the non-linear process in the SHG crystal [13].

The pulse train emitted from the laser is split into two beams and sent into the two arms of interferometer. One of the beams has a variable delay relative to the other. The original signals are filtered out and the SHG signal is detected using a photomultiplier tube (PMT).

Pulse shape	I(t)	$\Delta\tau/\Delta t_c$	$\Delta\tau\Delta\upsilon$ (TBP)
Gaussian	e^{-t^2}	0.7071	0.4413
Hyperbolic secant	$\text{sech}^2(t)$	0.6482	0.3148
Lorentzian	$[1+t^2]^{-2}$	0.5	0.142

Table 5.1: Table shows parameters for fittings of autocorrelation traces [13].

The intensity is recorded as a function of relative delay between the two arms of the interferometer. The intensity autocorrelation function depends on the actual pulse intensity shape and its delayed replica. The exact pulse duration and shape can be approximated by assuming a Gaussian, Lorentzian, or $sech^2$ intensity distribution, given in Table 5.1. The FWHM of the actual pulse (Δt) can be determined by deconvolving the measured FWHM of the autocorrelation trace (Δt_c), i.e. multiplying the $\Delta t/\Delta t_c$ factor of the assumed pulse shape. The autocorrelation traces of the 3-QW and 5-QW MLLs were recorded for bias conditions corresponding to the optimal mode locking regime.

(a)   (b)

(c)   (d)
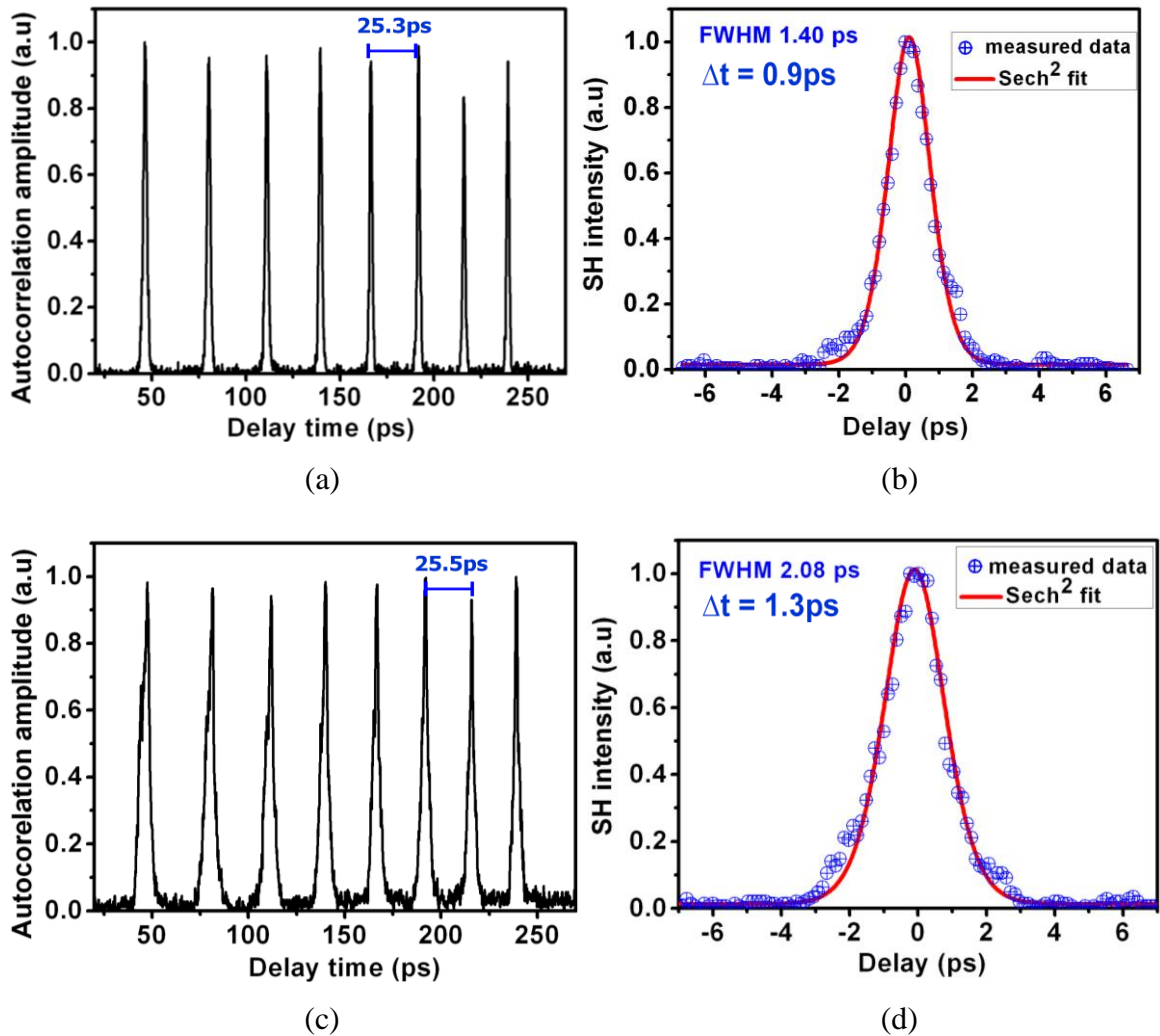
Figure 5.11: Measured AC traces under the optimal mode locking conditions: (a) and (b) shows the pulse train and a single pulse, respectively, of the 3-QW MLL for I_{gain} 60 mA and V_{SA} -3 V, whereas (c) and (d) shows the pulse train and a single pulse of the 5-QW MLL, respectively for I_{gain} 72 mA and V_{SA} -3 V.

Figure 5.11 shows the comparison of the pulse train and a single pulse emitted from the 3-QW and 5-QW MLLs, respectively. The spacing between the two pulses in the pulse train was

around 25.1 ps, which corresponds to the repetition rate of these devices i.e. ~ 39.7 GHz. The fitting for a singulated pulse of the measured autocorrelation traces was found to be $sech^2$. For the 3-QW MLL, the FWHM of the autocorrelation trace of isolated pulse was 1.40 ps, which deconvolve to 0.9 ps pulse duration. Similarly, for the 5-QW MLL the FWHM of the autocorrelation trace of isolated pulse was 2.08 ps, which gives a pulse duration of 1.3 ps. The shorter pulses (~ 31 % shorter) obtained from the 3-QW MLL as compared to the 5-QW MLL were due to the lower number of quantum wells in the active region of the 3-QW MLLs. The lower number of QWs in the active region reduces the differential gain (*dg/dN*), and thus leads to a higher gain saturation energy, which reduces pulse broadening due to self phase modulation in the gain medium [11]. This will be explained in more details later in this chapter.

Figure 5.12 shows the pulse width as a function of the gain current for different reverse voltages applied to the SA section of a 3-QW MLL. Typical trends for the pulse shortening and broadening were obtained, i.e. pulses broadening with increasing the gain injection current and shortening with increasing the absorber reverse voltage. The pulse broadening effect becomes more prominent at higher gain currents due to the higher pulse energies. The minimum pulse width was obtained at large reverse bias, where the absorber recovery time is shorter as detailed in Chapter 3 (Section 3.4.2.2).
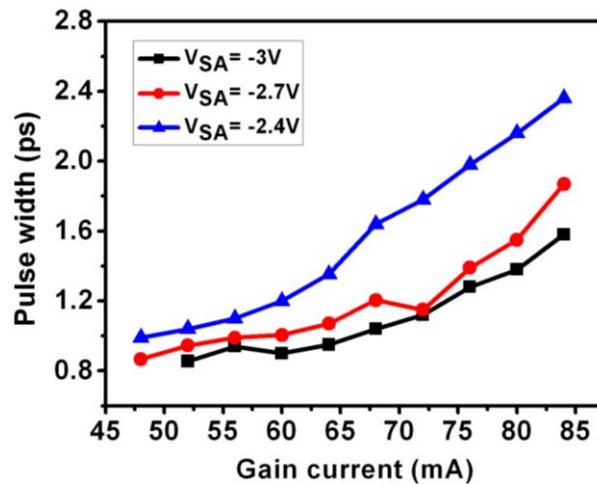
Figure 5.12: Measured SHG autocorrelation pulse width vs. I_{gain} at different values of absorber reverse voltages for the 3-QW MLL.

5.3.4   Mode Locking Maps of 3-QW and 5-QW SMLLs

Mode locking maps of the devices based on the 3-QW and 5-QW materials, with the same gain and SA length were made for comparison of the mode locking performance. Depending on the bias conditions of the gain and the SA sections, MLLs can operate in different regimes as indicated by different colours in Figure 5.13. In this figure, different operating regimes, i.e. CW emission (no mode locking), Q-switching, incomplete mode locking and optimal mode locking were classified on the basis of RF spectra peak-to-background ratio and extension ratio of the SHG autocorrelator pulses. The RF spectra in the range of 1-10 GHz were also recorded to identify the Q-switching operating regime. For a fixed value of SA reverse voltage, increasing the gain current causes an increase in pulse width and eventually causes the laser to switch to the CW emission regime.
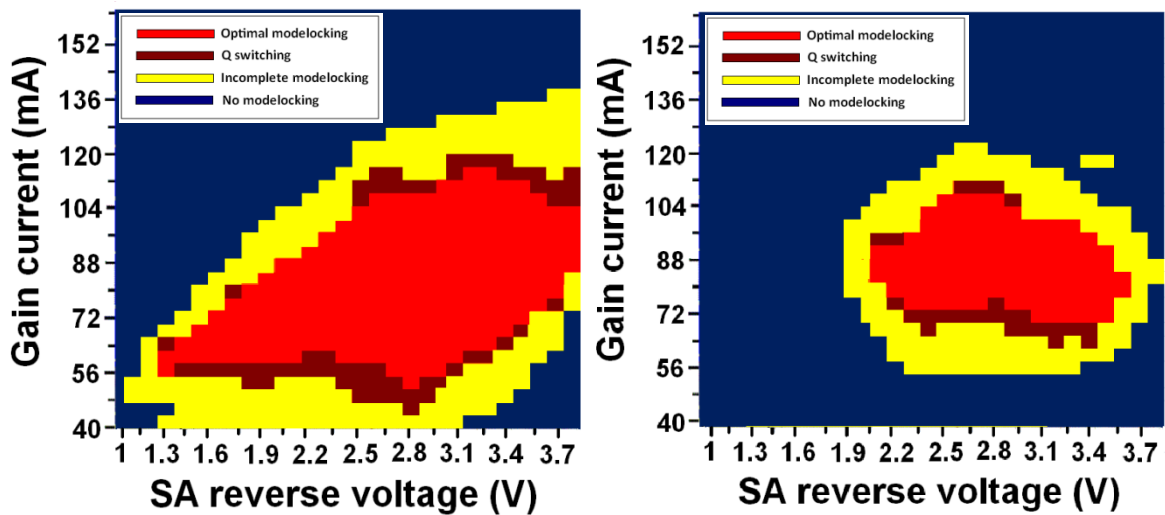
Figure 5.13: Mode locking map of the (Left) 3-QW and (Right) 5-QW MLLs for a range of bias conditions.

As mentioned earlier, the pulse energy increases with increase in the gain section current. With increase in the pulse energy, the required optimal SA reverse voltage also increases in order to increase the SA absorption and achieve the maximum pulse shortening per pass, which is required for the optimal mode locked operation [14]. The optimal mode locking in the MLLs is determined by the interplay between the saturable absorption, gain saturation and carrier lifetimes in the gain and the absorber sections [15]. As shown in Figure 5.13, for the 3-QW MLLs, stable mode locking was observed for gain currents ranging from 60 to 112 mA and the SA reverse voltages from 1.8 to 3.7 V. Similarly, for the 5-QW MLL, stable mode locking was observed for the gain current ranging from 70 to 108 mA and SA reverse voltages from 2.4 to 3.5 V. It can be assumed that the lower number of QWs leads to higher electric

field for a given SA reverse voltage, which suggests that stable mode locking can occur at lower SA reverse voltages. An important factor that determines the stability of the mode locking is the detuning of the energy gaps between the gain and the absorber sections. According to the work reported in [16, 17], stable mode locking is achieved if the gain and the absorber sections are spectrally aligned. The broader optical spectra of the 3-QW MLLs might result in band edge alignment of the gain and SA section for a wider range of bias conditions and therefore larger region of stable mode locking. The length of SA is also quite important in determining the range of stable mode locking. If the SA is too short, it is not sufficient to trigger the mode locking and conversely if it is too long, it results in increased losses, and in turn decreases the optical power in the cavity to modulate the SA [16]. For an optimized SA length, stable mode locking over a wide range of bias conditions exists. The larger mode locking region of the 3-QW MLLs can also be due to the optimised SA length.

According to the second condition for mode locking, given in Chapter 3 (Section 3.4.2), the saturation energies in the gain (E_g^{sat}) and the absorber (E_{abs}^{sat}) are quite important in determining the range of the stable mode locking of a MLL. The E_g^{sat} is strongly dependent on the number of QWs, with its value larger for the lower number of QWs due to the lower differential gain [18]. Compared to the 5-QW MLLs, the larger E_g^{sat} of the 3-QW MLLs results in less pulse broadening in the gain section, and thus a larger region of stable mode locking, as shown in the mode locking maps. This is consistent with the results reported in [18]. In the case of 5-QW MLLs, the lower value of E_g^{sat} leads to stronger pulse broadening in the gain section, and therefore the absorber is unable to compensate for the pulse broadening over a large range of bias conditions. This leads to a smaller region of stable mode locking.

5.4 Gratings Design, Simulations and Experimental Results

The most common way of fabricating DBR or DFB gratings requires regrowth of the epitaxial material, which increases the fabrication complexity and increases the risk of oxidation of the aluminium containing quaternary active layers. An alternative to this is the use of the surface etched gratings, which can be made by etching the semiconductor material above the active layer as shown in Figure 5.14. The following sections detail the simulations and the experimental results of the surface etched DBR gratings.
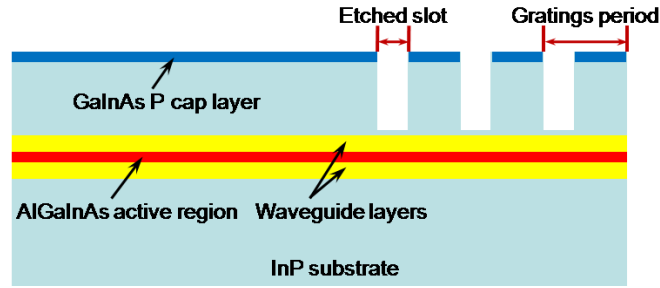
Figure 5.14: Schematic of the surface etched DBR gratings.

5.4.1   Simulation Results

DBR gratings with low optical losses and providing a reflectivity of around 25 % were required to obtain an acceptable value of threshold current and output power of the laser going into the SOA section of the MLL integrated with SOA. Therefore prior to fabrication, the gratings need to be numerically optimised to provide accurate wavelength control, lower optical losses, lower coupling losses to the substrate, and the desired repetition frequency of the device.

Due to the fabrication feasibility, a 3rd order DBR gratings were chosen for this work. The gratings were investigated with a two dimensional (2-D) simulation tool called CAMFR (Cavity Modelling Framework). The CAMFR simulation tool is based on EME (eigenmode Expansion) principle [19]. Simulation results using the CAMFR simulation tool, reported in [20] shows that the grating slot width affects the peak reflectivity, gratings losses and achievable etch depth. Narrow slots of the gratings provide low loss devices. Based on the simulation results reported in [20], the slot width of the gratings was selected to be 180 nm, which gives minimum possible losses and is a trade-off between reduced scattering losses and fabrication feasibility [20]. As explained in Chapter 4 (Section 4.5), the 60 nm thick $Al_{0.423}Ga_{0.047}In_{0.53}As$ layer behave as RIE dry etch stop layer to secure the gratings etch depth of 1.92 μm, while reducing the RIE lag effect in the gratings. The simulation results for 2.5 μm wide and 1.92 μm deep gratings show that reflectivity of < 25% can be obtained from ~ 150 μm long gratings, as shown in Figure 5.15. The simulated peak wavelength of the DBR gratings versus gratings periods is shown in the inset of Figure 5.15. An important parameter, which measures strength of the gratings is the coupling co-efficient of the gratings (κ), which is the amount of coupling between the forward and backward propagating waves. The coupling co-efficient of the gratings increases with increase in the index modulation.
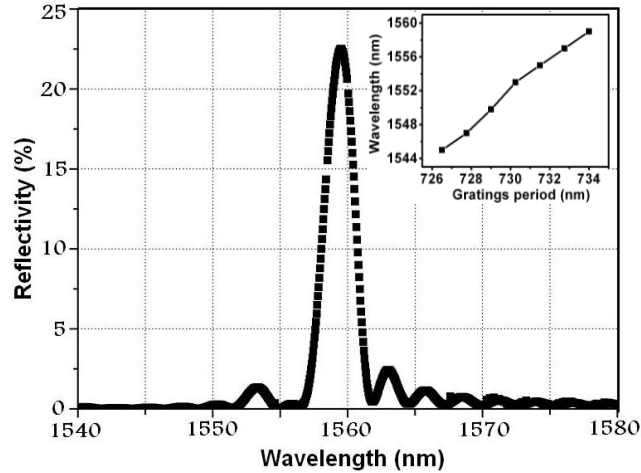
Figure 5.15: Simulated stop-band of DBR gratings for gratings period of 734 nm, whereas the inset shows the peak wavelength vs. gratings period.

The solution to the coupled mode equation gives a relationship between the DBR gratings reflectivity and the coupling co-efficient [4], which is given as:

$$R = tanh^2(\kappa L_g)$$

Equation 5.3

This shows that the reflection at Bragg wavelength increases with the index modulation and gratings length (L_g). Figure 5.16 (left) shows the Bragg reflection versus coupling co-efficient for 150 µm long gratings.
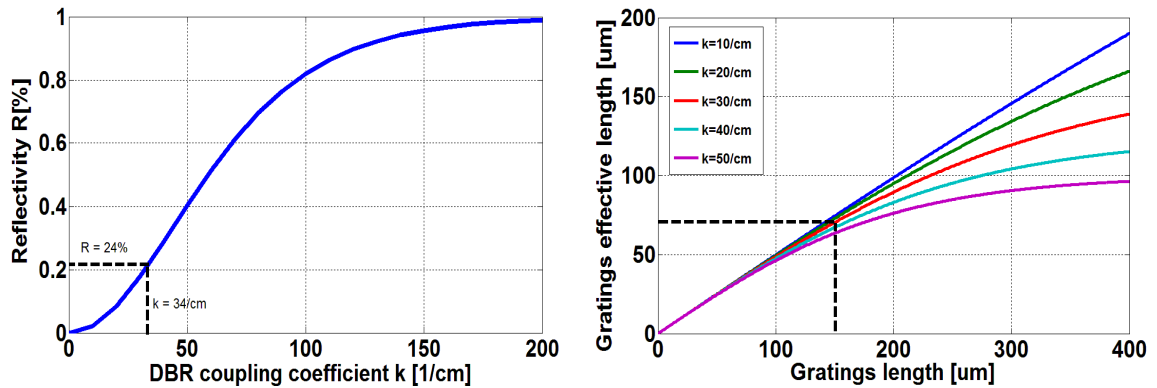
Figure 5.16: (Left) Calculated effective length of the gratings vs. gratings length for different values of coupling co-efficient, and (Right) the calculated gratings reflectivity vs. coupling co-efficient.

Figure 5.16 (left) shows that for peak reflectivity of around 25 %, the value of the coupling co-efficient is 34 cm^{-1}. Reflections from the gratings can be well approximated by a discrete mirror reflection with the magnitude of reflections equal to the sum of the reflections from each grating, and placed at a distance equal to effective length (L_{eff}). The light traversing the

gratings can only see the L_{eff} of the gratings. The effective length of the gratings is given as [21]:

$$L_{eff} = \frac{1}{2\kappa} tanh\ (\kappa L_g)$$

Equation 5.4

For weakly reflecting gratings, the *tanh(κL_g)* reduces to κL_g. The plot of L_{eff} versus L_g for different values of κ is shown in Figure 5.16 (right). This figure shows that for 150 μm long gratings with κ value of around 34/cm, the L_{eff} is 75 μm.

5.4.2   Experimental Results

In this Section the measurements results of the fabricated surface etched gratings are given. Surface etched gratings in this work were simultaneously defined with ridge waveguides using electron beam lithography and etched by RIE dry etching using $CH_4/H_2/O_2$ chemistry. Measurements were performed to determine the optical performance and important parameters of the gratings such as peak reflectivity wavelength, reflections stop band and coupling co-efficient.

5.4.2.1   Stop Band Measurements

The stop-band of the gratings determines the permitted wavelengths oscillations in the cavity and hence the optical spectrum. The bandwidth of the optical spectrum is of great importance for MLLs due to the inverse relationship of spectral bandwidth and temporal pulse width as detailed in Chapter 3 (Section 3.3.1). The stop-band of the gratings in this work was measured with optical back-reflection measurement. The measurement setup is shown in Figure 5.17. In these measurements, the light from a tunable laser was injected into the SOA facet of the device with a lensed optical fiber. The reflected light from the gratings was coupled to the optical spectrum analyser. The reflection spectrum of the gratings was obtained by scanning the laser output wavelength for a required range. In these measurements, the SOA section was biased at 100 mA to reduce the optical losses and get a clear reflection spectrum of the gratings.
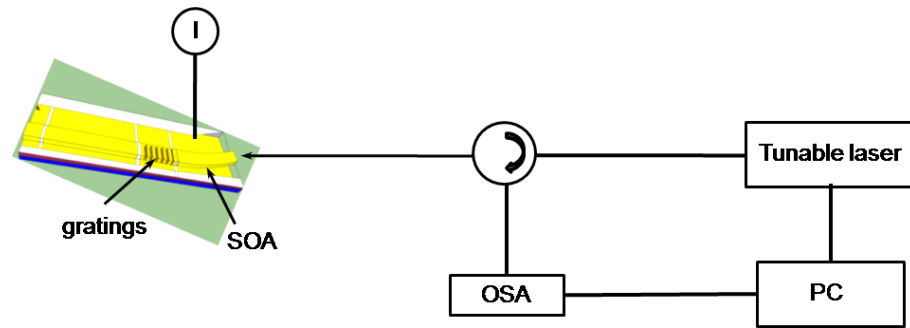
Figure 5.17: Experimental setup for measurement of gratings stop band.

The DBR section of the device was biased as 5 mA current. The measured gratings stop band for different gratings periods (Λ) is shown in Figure 5.18. The measured 3 dB bandwidth of the gratings stop-band was 1.9 nm. As shown in the figure, the measured peak reflectivity wavelength of the gratings for different periods suggests a close agreement between the simulated and measured results. Further, increasing the DBR section current from 0 to 5 mA causes ~ 2 nm blue shift in the reflection peak wavelength.
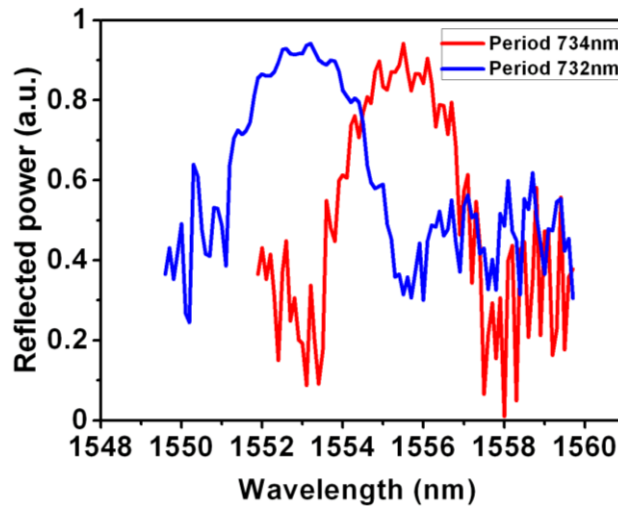
Figure 5.18: Measured stop-band of the gratings with the gratings period of 734 nm and 732 nm.

5.4.2.2   Reflectivity Measurements

Reflectivity of the DBR gratings was experimentally measured using the Hakki-Paoli technique, which involves the gain spectra analysis at sub-threshold injection current. The ASE spectrum from the cleaved facet of a DBR laser was captured at 22 mA injection current. For a comparison, the ASE spectrum from a Fabry-Perot (FP) laser was also captured under the same injection current density. Using the Hakki-Paoli gain measurement technique, the RG (R being the reflectivity and G the modal gain) products for both the DBR and FP lasers was

obtained from relative peaks, P_i, and adjacent valleys, V_i, in the spontaneous emission spectrum. The reflectivity of the gratings ($R_1'(\lambda)$) for each wavelength is calculated by using the relationship [22]:

$$R_1'(\lambda) = \left(\frac{\rho'(\lambda)}{\rho(\lambda)}\right)^2 . R_1(\lambda)$$

<div align="right">Equation 5.5</div>

where $\rho'(\lambda)$ is the RG product of the DBR laser, $\rho(\lambda)$ is the RG product of the FP laser, $R_1(\lambda)$ is the cleaved facet reflectivity of the FP laser and its value was assumed to be 0.32 for all the calculations.

The measured value of peak reflectivity of the gratings was found to be around 21-22 %, which is close to the numerically calculated value. Putting the value of measured reflectivity of the gratings in Equation 5.3 and Equation 5.4, the coupling coefficient of 30 cm^{-1} and gratings effective length of 70 µm was obtained. It was therefore deduced that the designed gratings are capable of achieving sufficient reflectivity for the devices in this research work.

5.5 Mode Locked DBR Lasers

The DBR gratings previously described were integrated with the MLLs. The ridge waveguides of the MLLs and the third order gratings (period-732 nm) were simultaneously defined by the electron beam lithography and a CH$_4$:H$_2$:O$_2$ RIE dry etching process in a single etching step. The gratings and the ridge structures were passivated using SiO$_2$ and HSQ. A schematic of the mode locked DBR laser is shown in Figure 5.19.
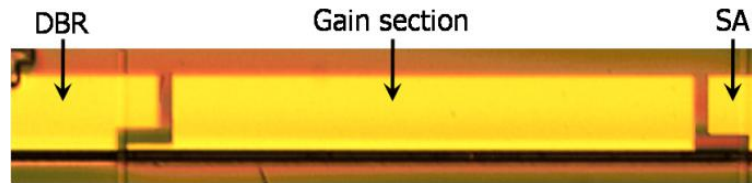
Figure 5.19: Schematic of a mode locked DBR laser.

These devices were based on the 3-QW active region epitaxial material. These devices consist of a 1085 µm long cavity, with a 30 µm long SA and 150 µm long DBR section. The ridge waveguides were 2.5 µm wide and 1.92 µm deep. The electrical isolation between the SA, gain and DBR section was achieved by dry etching the heavily doped (1.5 x 10^{-19}) p-cap layer. The measured electrical resistance between the two sections was more than 20 kΩ.

For these devices, the output power versus gain current, the optical spectra and the SHG intensity autocorrelation traces were measured. The RF spectra of these devices couldn't be measured due to the bandwidth limitation of the available RF spectrum analyser. However, the variation in repetition frequency of the MLL can be easily achieved by modifying the length of the cavity. The basic results of these devices are given in the following sections.

5.5.1   Optical Power Measurements

Optical power versus gain current for different absorber voltages were measured from the DBR facet of the device with the DBR section current fixed at 5 mA. The output power from the device was measured using a broad area Germanium based photodiode. These measurements were performed to assess the threshold currents and output power of the device under different bias conditions. As shown in Figure 5.20, the threshold current of the device increases, while the output power and the slope efficiency decreases with increase in absorber reverse voltage. The increase in the threshold and the reduction in slope efficiency with increase in the absorber reverse voltage are due to increase in interband and exciton absorption.
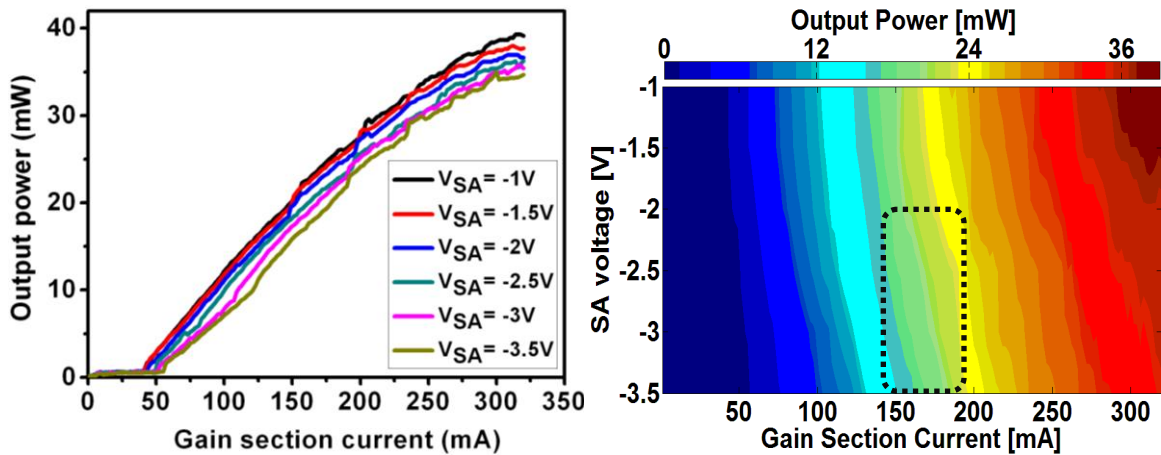
Figure 5.20: (Left) Output power vs. gain section current at different SA reverse voltages while I_{DBR} 5 mA. (Right) Output power map as a function of gain current and SA reverse voltages at I_{DBR} 5 mA. The black dotted rectangle indicates the region of mode locking.

The kinks observed in the *L-I* curves, especially at high reverse bias voltages are caused by the thermal detuning of the gain and the DBR section and are connected with a mode hop [23]. The output power corresponding to the mode locking regime of these devices is indicated by the region enclosed by the dotted rectangle in the output power map. The maximum output power corresponding to the mode locking regime of the device is around 24 mW. These

devices were measured only up to 320 mA gain section current and 3.5 V SA reverse voltage. Measurements at higher gain currents and reverse voltages were not carried out for the fear of degradation of the device before characterisation of the mode locking performance. Since the absorber section was only 30 μm long, it could be easily damaged at large reverse voltages. The photocurrent generated in the absorber section increases with increasing optical power in the cavity and the absorber reverse voltage. High photocurrent density generated in the absorber causes heating of the absorber section and band-gap shrinkage, which eventually causes catastrophic damage of the absorber section and hence the deterioration of the mode locking performance [24].

5.5.2   Optical Spectra Measurements

As shown in Figure 5.19, the DBR section of the device is a separate section and can be independently biased to tune the peak wavelength and the repetition frequency of the device.
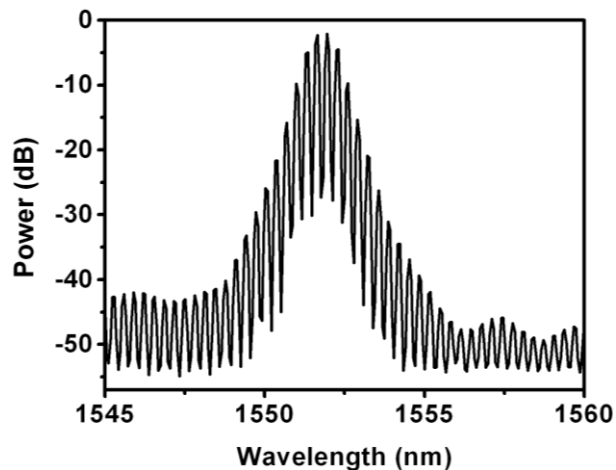
Figure 5.21: Measured optical spectrum at I_{gain}= 140 mA, I_{DBR} = 5 mA and V_{SA}= -3 V.

The optical spectrum was measured with a resolution bandwidth of 0.06 nm, which was limited by the optical spectrum analyser. The measured 3 dB bandwidth of the optical spectrum shown in Figure 5.21 is 1.2 nm, which is much smaller than that of the FP-laser (9.2 nm) shown in Figure 5.7. The mode spacing between the two consecutive cavity modes is 0.34 nm, which corresponds to around 43 GHz repetition frequency of the device.

At lower gain section currents, the device was lasing at peak wavelength of 1537 nm, whereas the gratings were designed for the peak wavelength of around 1554 nm. Therefore, due to the mismatch of the device peak wavelength and the gratings stop band at lower gain section currents, the reflections in the cavity were provided by the cleaved facets and a broad optical

spectrum (with 3 dB bandwidth of around 9 nm) was obtained. However, at higher gain section currents, the device lasing wavelength and the gratings stop band matched due to the red shifting of the gain peak. Under the wavelength matching conditions, the 3 dB bandwidth of the optical spectrum was reduced to 1.2 nm. In this case, the 3 dB bandwidth of the optical spectrum was determined by the reflection bandwidth of the DBR.

5.5.3   Pulse Width Measurements

The pulse width of these devices was measured using the SHG intensity autocorrelator with the measurement setup shown in the Section 5.3.3 (Figure 5.10). The measured autocorrelation pulse train and a single pulse of the device are shown in Figure 5.22.
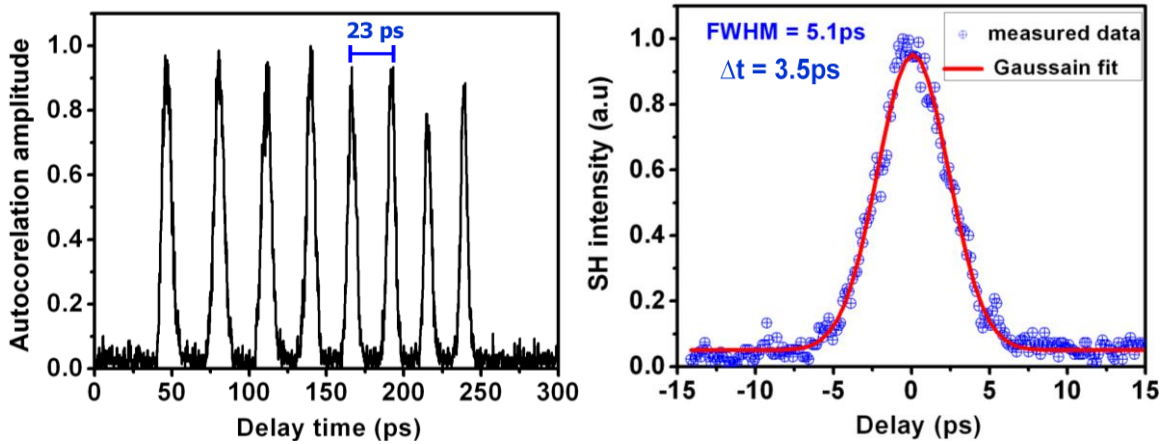
Figure 5.22: Measured autocorrelation pulse train (left) and a single pulse (right) at I_{gain}= 140 mA, I_{DBR} = 5 mA and V_{SA}= -3 V.

The period of the emitted pulse train was 23 ps, corresponding to a repetition rate of around 43 GHz, which is in accordance to the mode spacing of the measured optical spectrum. The best curve fitting for a single pulse was found to be the Gaussian fit. The full width half maximum (FWHM) of the single pulse was found to be 5.1 ps, which deconvolves to 3.5 ps pulse duration. Generally, the pulse width of the mode locked DBR lasers is several times higher than that of the FP laser. This is due to the inverse relationship between the pulse-width and the spectral width of the MLLs. The spectral width and hence the pulse width of a DBR-MLL is limited by the reflectivity bandwidth of the DBR gratings. The time bandwidth product (TBP) of the output is 0.52, which is larger than the transform limited value for the Gaussian pulses. The increase in the TBP is most likely due to the self-phase modulation in the gain section of the device [14].

5.6 Chapter Summary

The characterisation setups and the main results obtained from the devices based on the 3-QWs and 5-QWs active region devices were presented. Compared to the 5-QW material based devices, the 3-QW material based FP lasers showed around 126 % increase in the output average power, 43 % reduction in the optical losses and reduction in the divergence angles. Furthermore, compared to the 5-QW based MLLs, the 3-QW based MLLs showed 85 % reduction in the RF linewidth, and 31 % reduction in the pulse width with a broader region of the optimal mode locking. The optimised length of the SA was found to be 3 % of the cavity length.

The superior mode locking performance of the devices based on 3-QW epitaxial structure is due to the design of the epitaxial structure, which provides low waveguide losses and low optical confinement active region thus providing higher saturation energy of the gain medium. The low optical confinement of the active region results in lower ASE coupling coefficient and thus reduces the RF linewidth and the timing jitter. The simulations and experimental results shows that the insertion of far-field reduction layer in the n-cladding layer together with the improved waveguide design of the 3-QW material increases the mode spot size and thus reduces the far-field of the devices.

Numerical simulation results of the DBR gratings with the peak reflectivity of around 25 % were presented. Third order gratings were selected for this work due to the fabrication feasibility. The experimental results of the fabricated gratings were presented. Monolithic DBR-MLLs were designed, fabricated and characterised before then being monolithically integrated with the SOAs. The output power, optical spectrum and the pulse width measurements of the fabricated mode locked DBR lasers were given. The average output power of the mode locked DBR laser corresponding to the optimal mode locking bias conditions was around 24 mW. Compared to the FP-MLL, the DBR-MLLs showed narrower optical spectra and wider pulse durations.

5.7 References

1.   Minch, J., et al., *Theory and experiment of In1-xGaxAsy P1-y and In1-x-yGaxAlyAs long-wavelength strained quantum-well lasers.* IEEE Journal of Quantum Electronics, 1999. 35(5): p. 771-782.

2.   Lianping Hou, et al., *10GHz AlGaInAs/InP 1.55 um passively mode-locked laser with low divergence angle and timing jitter.* Optics express, 2011. 19(26).

3.   D. Garbuzov, et al., *1.5um wavelength, SCH-MOW InGaAsP/lnP broadened-waveguide laser diodes with low internal loss and high output power.* Electronics Letters 1996. 32(18): p. 1717-1719.

4.   G. P. Agrawal and N. K. Dutta, *Long-Wavelength Semiconductor Lasers*, Van Nostrand Reinhold Company: New York.

5.   Takahiro Numai, *Fundamentals of semiconductor lasers*. 2004, Newyork: Springer.

6.   B. Qiu, et al., *Design and Fabrication of Low Beam Divergence and High Kink-Free Power Lasers.* IEEE Journal of Quantum Electronics, 2005. 41(9): p. 1124-1130.

7.   E. Ippen, *Principles of passive mode locking.* Applied Physics B: Lasers and Optics, 1994. 58(3): p. 159-170.

8.   U. Bendelow, et al., *40GHz mode locked semiconductor lasers: Theroy , simulations and experiments.* Optical and quantum electronics, 2006. 38: p. 495-512.

9.   Available Online, *http://w.w.w.rp.photonics.com/: Last accessed Oct 2011*.

10.   Lau K. Y. and Paslaski J., *Condition for short pulse generation in ultra high frequency mode locking of semiconductor lasers.* IEEE Photonics Technology Letters, 1991. 3: p. 974-976.

11.   K. Mergem, et al., *Short pulse generation using a passively mode locked single InGaAsP/InP quantum well laser.* Optics express, 2008. 16(14).

12.   Fabien Kefelian, et al., *RF linewidth in monolithic passively mode-locked semiconductor lasers.* IEEE Photonics Technology Letters, 2008. 20(16).

13.   Kresten Yvind, *Ph.D. Thesis, "Semiconductor mode locked lasers for optical communication systems"*, in Technical University of Denmark. 2003: Denmark.

14.   Dennis J. Derickson, et al., *Short Pulse Generation Using Multisegment Mode-Locked Semiconductor Lasers.* IEEE Journal of Quantum Electronics, 1992. 28(10).

15.   K A Williams, M G Thompson, and I H White, *Long-wavelength monolithic mode-locked diode lasers.* New Journal of Physics, 2004. 6(179).

16.   Julien Javaloyes and Salvador Balle, *Mode locking in Semiconductor Fabry-Pérot Lasers.* IEEE Journal of Quantum Electronics, 2010. 46(7): p. 1023-1030.

17.   D. Kunimatsu, S. Arahira, and Y. Ogawa, *Passively Mode-locked Laser Diodes with Bandgap-Wavelength Detuned Saturable Absorbers.* IEEE Photonics Technology Letters, 1999. 11(11): p. 1363-1365.

18.   Kresten Yvind, et al., *Design and evaluation of mode-locked semiconductor lasers for low noise and high stability.* Proceedings of SPIE 5825, 2005. 37.

19.   Available online, *http://camfr.sourceforge.net/index.html : last accessed 19 Oct 2011*.

20.   Lianping Hou, et al., *Monolithic 40-GHz Passively Mode-Locked AlGaInAs-InP 1.55-um MQW Laser With Surface-Etched Distributed Bragg Reflector.* IEEE Photonics Technology Letters, 2010. 22(20): p. 1503-1505.

21.   L. A. Coldren and S. W. Corzine, *Diode Lasers and Photonic Integrated Circuits*, Singapore: John Wiley and Sons, Inc.

22.   S. A. Merritt, et al., *Measurement of the Facet Modal Reflectivity Spectrum in High Quality Semiconductor Travelling Wave Amplifiers.* Journal of Lightwave Technology 1995. 13(3).

23.   Lianping Hou, et al., *Monolithic 45-GHz Mode-Locked Surface-Etched DBR Laser Using Quantum-Well Intermixing Technology.* IEEE Photonics Technology Letters, 2010. 22(14): p. 1039-1041.

24.   Giuseppe Tandoi, *Monolithic High Power Mode Locked GaAs/AlGaAs Quantum Well Lasers*, in School of Engineering. 2011, University of Glasgow, Glasgow.

Chapter 6

Mode Locked Lasers with Integrated SOAs: Results

6.1 Introduction

This chapter presents the design of the mode locked laser (MLLs) integrated with semiconductor optical amplifier (SOAs), and display the main results obtained from both the SOA alone and SOA integrated with the MLL. These devices were based on the 3-QW active region epitaxial material due to its higher output power and improved mode locking performance, as described in the Chapter 5. Basic characterisation results of the SOAs such as light-current characteristics, optical spectra, optical gain and saturation output power are presented. The SOAs are integrated with the DBR-MLLs at the output for increasing the output power of the lasers. The output power measurements of the MLLs with integrated SOAs, at both the SA and SOA facets are given. The far-field measurement results of the devices also are presented. This is followed by the mode locking characterisation results such as the optical spectra, RF spectra and pulse width measurements of the integrated devices measured at both the SA and SOA facets. The output peak power and time bandwidth product (TBP) measured at the SOA facet for different SOA currents are shown. Finally, some suggestions for achieving further higher output powers are explained.

6.2 Semiconductor Optical Amplifiers

As mentioned in Chapter 3, SOAs are optoelectronic devices which can amplify input optical signals. SOAs in this project were used to increase the output power of the MLLs in a monolithically integrated master oscillator power amplifier (MOPA) configuration. The stand-alone SOAs were fabricated and characterised to analyse the basic device properties such as ASE output power, optical spectra, optical gain and saturation output power. The fabricated SOAs were 1000 µm long, single contact devices based on the 3-QW active region epitaxial material. The optical microscope picture of the fabricated SOA is shown in Figure 6.1.
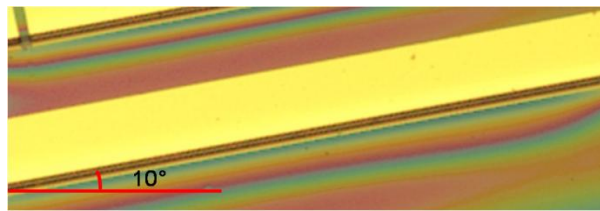
Figure 6.1: Optical microscope picture of the fabricated SOA with the waveguides tilted at 10° to the output facet.

Similar to the lasers fabricated in this work, the ridge waveguides of the SOAs were 2.5 µm wide and 1.92 µm high to ensure single mode operation. The output waveguides were tilted at 10° to the output facet to reduce the facet reflection coupling into the waveguide. The fabrication of the device was completed in four electron beam lithography steps. After the fabrication was completed, the chip was cleaved into devices bars and mounted on brass sub-mounts for testing.

6.2.1   Light-Current Characteristics

The devices were mounted on a copper heat sink with the temperature controlled at 20°C. Continuous wave (CW) current is injected into the device, while the output power is measured using a wide area photodetector, placed as close as possible to the facet of the device. Figure 6.2 shows typical light-current (*L-I*) and voltage-current (*V-I*) characteristics of the device. The soft turn-on observed in the *L-I* curve (indicated by red colour) as shown in the plot is due to the amplification of the spontaneous emission of the device. As expected, the voltage increases with increase in the bias current. The *V-I* curve (indicated by the blue colour) shows the electrical behaviour and the resistance of the device.
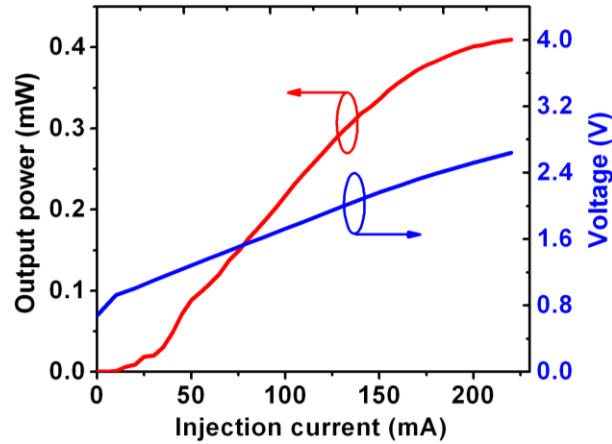
Figure 6.2: *L-I* curve of 1mm long SOA with the waveguides tilted at 10° to the output facets.

The device resistance calculated from the slope of the *V-I* curve above the turn-on voltage is around 8 Ω. At lower injection currents, the output power of the device is due to the spontaneous emission, whereas at higher currents, the stimulated emission is the dominant effect which results in an increase in the slope efficiency of the *L-I* curve. At higher injection currents, the output power is mainly given by the spontaneously emitted photons coupled into the active region and then amplified as they propagate inside the waveguide. The output power saturates at around 230 mA injection current.

6.2.2   Optical Spectra Measurements

As discussed in Chapter 3 (Section 3.8), the ASE spectrum is an important parameter of the SOAs as it can show the gain bandwidth and ripples. Unlike the semiconductor laser diodes, the SOAs give a broad spectral bandwidth, which is always desired. The ASE spectra of the SOAs were measured by coupling the ASE output from the device facet into a lensed fiber and going through an optical isolator into an optical spectrum analyser. Due to the tilted waveguide structure of the device, the output from the device was emitted at around a 32° offset in the horizontal direction (modal index 3.18 and internal angle 10°). Therefore, to couple the output light from the device, a single mode lensed fiber was aligned at 32° to the output facet of the device. The ASE spectra of the device at different biases are shown in Figure 6.3. From the figure, it is clear that an increase in the injection current causes blue shift of the emission wavelength, which is caused by the band filling effect [1]. From the plot, it is observed that increasing the SOA injection current results in an increase in the ASE rate and hence a higher value of optical gain.
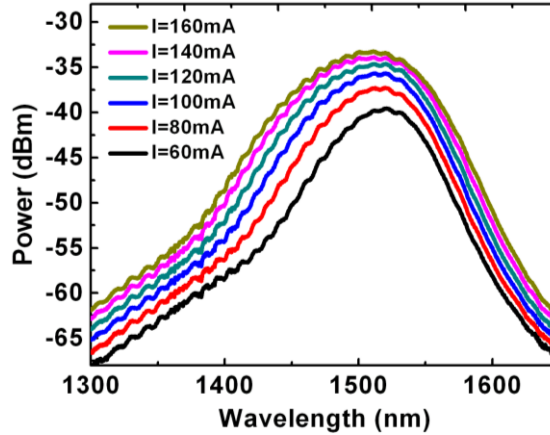
Figure 6.3: Measured ASE spectra of the SOA at different injection currents.

The modulation in the ASE spectra is limited by the resolution of the spectrum analyser, therefore lower than the actual modulation. Using the modulation values given in Figure 6.3, a facet reflectivity value of 5×10^{-4} is obtained.

6.2.3 Optical Gain and Saturation Output power

The optical gain is one of the most important characteristics of an optical amplifier. Optical gain is the ratio of signal power at the output to the input. The saturation output power is the value of output power at which the optical gain of the SOAs reduces by 3 dB from its small signal value. The optical gain and the saturation output power of the SOAs determines the ability of the device to scale up the power of an input signal. We wish to fabricate a high output power MLL by integrating an SOA at the output of the MLL. Thus to get high output power, higher optical gain and saturation output power of the SOA is desired. The schematic of measurement setup used for measurement of the optical gain and saturation output power of the SOAs is shown in Figure 6.4.
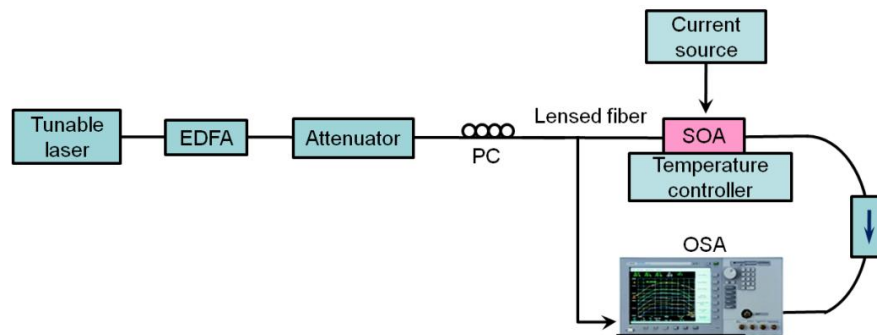
Figure 6.4: Schematic of experimental setup used for measurements of the optical gain and saturation output power of SOAs.

These measurements were carried out at 20°C heat sink temperature. The CW light from a tunable laser operating at 1.55 μm wavelength was amplified by an EDFA and injected into the SOA after passing through a polarisation controller, attenuator and an optical isolator. The polarisation controller allows the adjustment of the input signal polarisation. The input signal polarisation was adjusted for maximum SOA gain (TE gain) as this will be the case in the integrated devices. The variable attenuator allows the adjustment of the input signal power to the SOA. The optical isolators at both the input and output side of the device were used to avoid back reflected light into the device. Finally, the optical spectrum analyser was used to measure the power of the input and output signals. These measurements were carried out using LABVIEW codes for automated remote control.
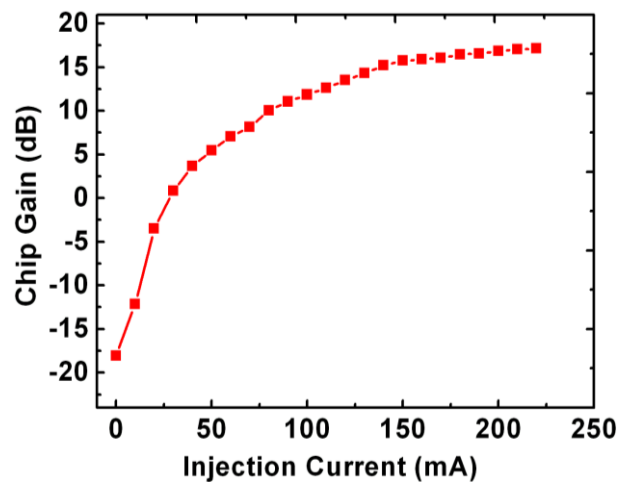
Figure 6.5: Measured chip optical gain as a function of SOA injection current for an input power of -20 dBm and input signal wavelength of 1.55 μm.

The chip optical gain as a function of SOA injection current is shown in Figure 6.5. These results were obtained for the input signal wavelength of 1.55 μm and power of -20 dBm. From the plot, typical trends are observed, i.e. the chip optical gain initially increases with increasing the SOA injection current and at around injection current of 230 mA, the optical gain cannot be further increased by increasing the injection current. No gain ripples were observed, which indicate that the effective facets reflectivity was sufficiently low. The maximum small signal chip gain of the device is 17 dB. The largest possible small signal gain obtained from the device is limited by the saturation of ASE due to gain clamping mechanism of ASE [2]. The chip optical gain as a function of output power for injection current of 250 mA and input wavelength of 1.55 μm is shown in Figure 6.6.
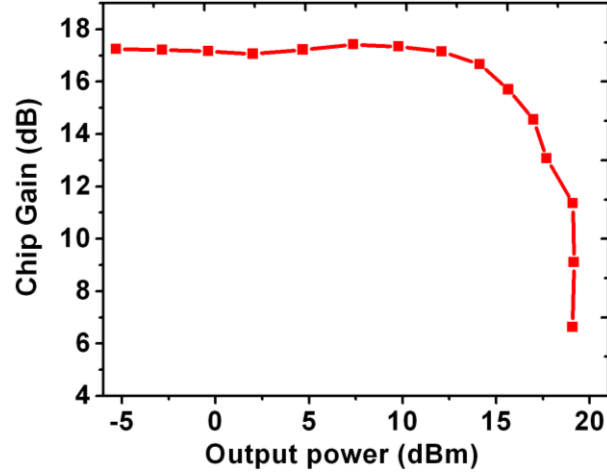
Figure 6.6: Measured optical gain as a function of output power of the SOA at input wavelength of 1.5 μm and injection current of 250mA.

For low output powers the optical gain of the device is higher, however, for large output powers the optical gain of the device starts to decrease. The decrease in the optical gain at higher output powers is due to the decrease in carrier density. The saturation output power of the device is 15.8 dBm. For an output power of 19.3 dBm, the optical gain of the device drops to 6.6 dB. For SOAs based on the 3 QW active region InGaAsP material, saturation output power value of 19.6 dBm is reported [3].

6.2.4   Noise Figure Measurements

The noise added to the signal during optical amplification is an important characteristic of the SOAs. During the amplification process, ASE promotes chaotic signal fluctuations, which can degrade the signal to noise ratio (SNR). The added noise can be quantified using a parameter called the noise figure, which is the ratio of the signal to noise at the input to the signal to noise measured at the output. The values of chip noise figures are typically within the 4 to 8 dB range [3, 4]. This is due to the signal-spontaneous and spontaneous-spontaneous beat noise [5]. The total spontaneous noise power in a single mode of one polarisation at the output facet of the amplifier is given by [6]:

$$P_{sp} = hv\frac{F}{2}(G-1)\delta v$$

Equation 6.1

where *hv* is the photon energy, *F* is the noise figure, *G* is the single pass gain and *δv* is the effective bandwidth of the noise spectrum.
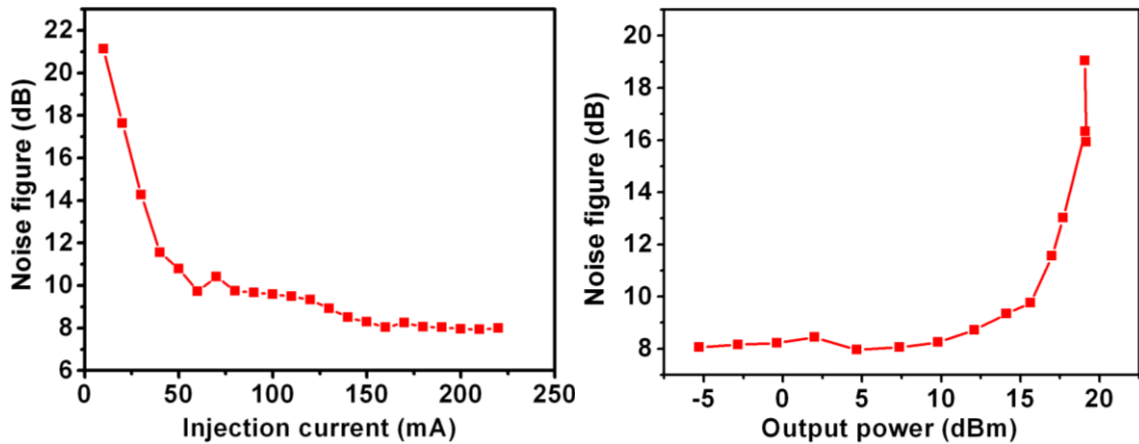
Figure 6.7: Measured (Left) noise figure as a function of injection current and (Right) noise figure as function of output power of the SOA for input wavelength of 1.5 μm.

Figure 6.7 shows the chip noise figure of the SOA for an input wavelength of 1.55 μm. Figure 6.7 (left) shows the decrease in the noise figure as the injection current is increased. In SOAs, the population inversion parameter determines the amount of ASE added to the input signal. For higher current densities, the population inversion parameter is lower and thus leads to a reduction in the noise figure. Similarly, for higher SOA output powers, the population inversion parameter is higher, which leads to an increase in the noise figure, which is shown in Figure 6.7 (right).

6.3 Curved Waveguide Design

Curved waveguides were required in this work to allow the waveguides at the output facet tilted at 10°, as shown in Figure 6.9. Losses in the curved waveguides refer to the optical power losses due to the curves in the waveguides. During propagation in the curved waveguides, the guided mode loses its symmetry and moves towards the outer radii of the curved structure [7]. Curved losses (bending losses) are inversely related to the bend radius and the index difference between the core and the cladding layers of the material. Comparing to the deeply etched waveguides, the shallow etched waveguides results in more bending losses for a given curve radius [8]. Bending losses as a function of bend radius for a 2.5 μm wide and 1.92 μm high ridge waveguides were obtained using a 3-D beam propagation simulations tool, BeamPROP. Figure 6.8 shows that the bending losses exponentially decrease with increasing the bend radius. The critical bend radius is found to be ~ 350 μm. The optical losses are minimum for bend radius greater than the critical value.
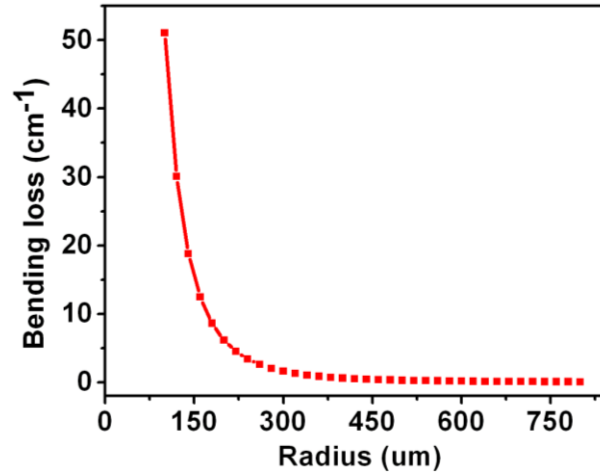
Figure 6.8: BPM Simulation results of the bending losses for 2.5 μm wide and 1.92 μm high ridge waveguides.

6.4 Mode Locked Laser with Integrated SOA: Device Layout

As already mentioned in Chapter 5 (Section 5.5), a DBR-MLL device consists of an electrically isolated saturable absorber (SA), gain and DBR section. To realise high power DBR-MLLs, SOAs were monolithically integrated at the output of the DBR-MLLs. Figure 6.9 shows the schematic of a DBR-MLL with a curved SOA, monolithically integrated at the output.
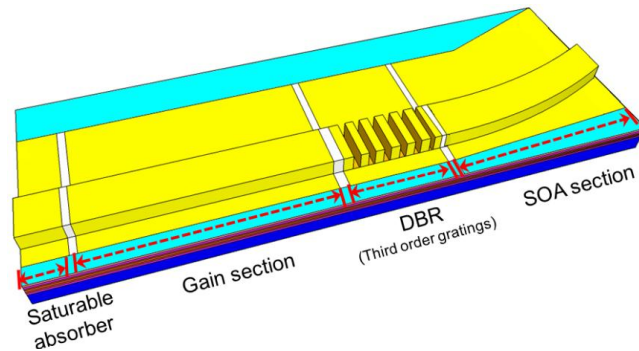
Figure 6.9: Schematic of a DBR-MLL monolithically integrated with an SOA.

The devices in this work were designed to operate with a pulse repetition frequency of around 40 GHz, due to future telecommunication system requirements [9]. The electrical isolation between the SA, gain, DBR and SOA sections of the device was obtained by leaving 15 μm wide gaps in the p-contact metallisation and dry etching the heavily p-doped cap layer. The total length of the device was 2200 μm with a 30 μm long SA section, 1020 μm long gain section, 150 μm long DBR section and 955 μm long SOA section. Based on the simulation results presented in Chapter 4 (Section 4.14), the width of the waveguide was selected to be

2.5 µm and height 1.92 µm, for single mode operation of the device. In these devices, the length of the SA was 3 % of the total cavity length, which is optimum for the devices based on the 3-QW epitaxial material. The DBR section consists of 150 µm long 3rd order surface etched gratings, which were simultaneously defined with the ridge waveguides using electron beam lithography and etched using $CH_4:H_2:O_2$ etch chemistry. The ridge waveguides and the DBR structures were planarized using HSQ and SiO_2 to provide greater mechanical stability to the device and avoid breaks in the p-contact metallisation of the vertical waveguide side walls, as discussed in Chapter 4 (Section 4.12). The 734 nm period gratings were numerically optimised using the Cavity Modelling Framework (CAMFR) simulation tool to obtain low loss gratings. Based on the simulation results reported in [10], a slot width of 180 nm was selected as a trade-off between lower optical losses and fabrication tolerance. The mode locking performance of the device can be strongly influenced by the facet back reflections from the SOA facet. Therefore the output waveguide of the SOA was tilted at 10° to the cleaved facet to reduce facet effective reflectivity. The SOA is a curved waveguide with a curve radius of 5.7 cm, which is significantly larger than the critical bend radius as shown in Figure 6.8. The picture of the integrated device taken by a camera fitted in an optical microscope is shown in Figure 6.10.
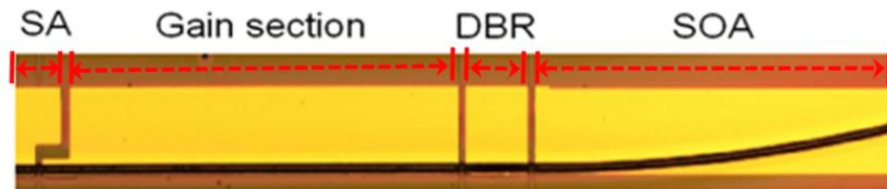
Figure 6.10: Optical microscope picture of the DBR-MLL integrated with an SOA.

6.5 Output Power Measurements of MLLs with Integrated SOAs

Generally, narrow optical pulses and RF line-widths from MLLs are obtained at low gain current, which corresponds to low output powers. The reason of integration of SOAs with the MLLs in this work was to increase the output power of the laser in mode locked operation. Output power measurements were performed to analyse the effect of the integrated SOA on the output power of the lasers. This section details the output power measurements at both the SA and the SOA facets of the integrated device. These devices were mounted on brass mounts using conductive epoxy and both the SA and SOA facets were left uncoated and tested on a temperature controlled heat sink set at 20°C. All the measurements were carried out by reverse

biasing the SA section, while forward biasing the gain, DBR and SOA sections. The output power from the device was collected using a broad area Germanium based photodetector.

6.5.1   Light-Current Characteristics

The *L-I* curves of the device were measured using CW current drive. The output at the SOA facet was collected using a broad area photodetector, whereas the DBR and the SOA currents were fixed at 5 and 250 mA, respectively.
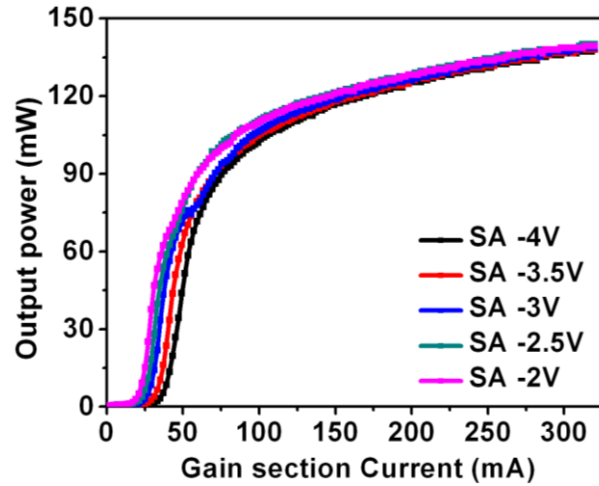
Figure 6.11: *L-I* curve of the mode locked laser with integrated SOA, measured at SOA facet for $I_{DBR} = 5$ mA and $I_{SOA} = 250$ mA.

Figure 6.11 shows the output power versus gain current for different SA reverse voltages. From the figure, some typical trends can be observed, such as increase of threshold current and decrease of slope efficiency with increase in the SA reverse voltage. The *L-I* curves show that the output power is nearly constant at higher gain section currents, which is caused by the saturation of the integrated SOA. Due to the saturation behaviour of the output power, the value of output power at higher gain currents for different SA biases is nearly the same. The maximum CW output power obtained from this device is around 140 mW. Mode locking in these devices occurs in the range of gain current from around 180 to 250 mA and SA reverse voltage from 2.5 to 4 V. The maximum average output power corresponding to the mode locking regime of these devices is around 130 mW. The average output power map measured at both the SA and SOA facets is shown in Figure 6.12.
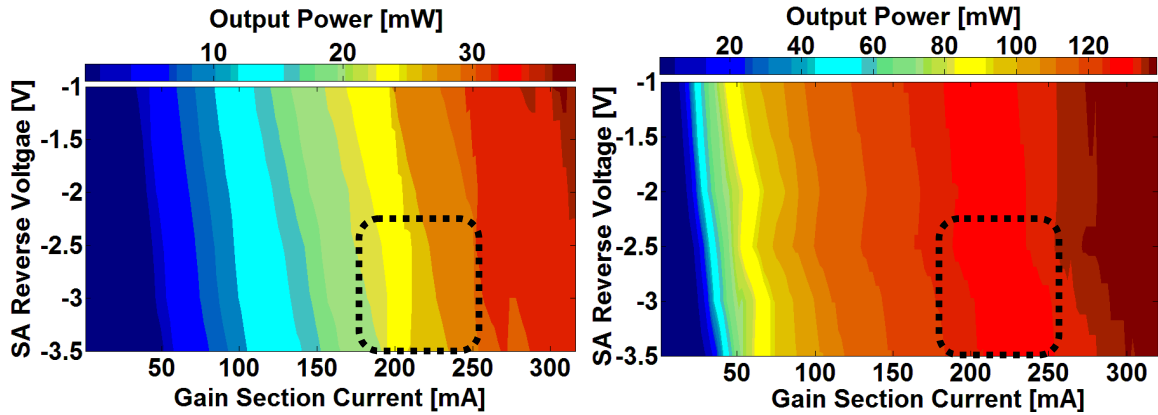
Figure 6.12: Map of the average output power as a function of gain current and SA reverse voltage from (Left) SA facet of the device and (Right) SOA facet of the device at I_{SOA}= 250 mA, I_{DBR} = 5 mA.

The region enclosed by the dotted black lines in the output power maps indicate the average output power corresponding to the mode locking regime. The maximum average output power obtained from the SA facet of the device under mode locking operation was around 28 mW, whereas that from SOA facet was 130 mW. These results shows that the integration of SOA at the output facet of the device increased the average output power in the mode locked operation by a factor of around 4.6.

6.5.2   Effect of SOA Bias on the Output Power

To analyse the effect of the SOA bias on the output power of the device, the output power was measured under different SOA bias conditions. The output power was measured at the SOA facet with the DBR current fixed at 5 mA and SA reverse voltage at 4 V.
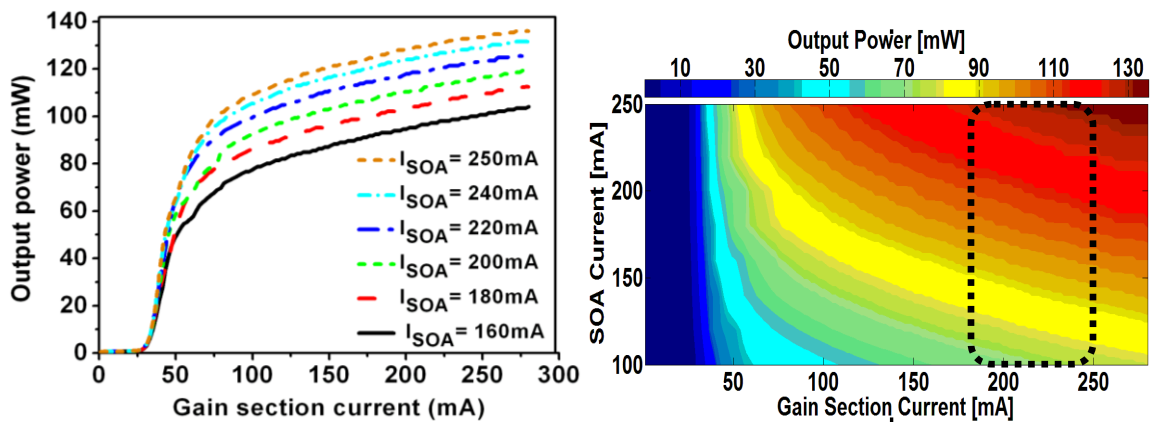
Figure 6.13: Measured (Left) *L-I* curves for different SOA currents and (Right), output power map for different SOA and gain currents while the I_{DBR} = 5 mA and V_{SA} = -4 V.

The *L-I* curves for SOA currents ranging from 160 to 250 mA are shown in Figure 6.13 (left). The *L-I* curves shows, that as expected, the output power increases with increasing the SOA current. Increase in the SOA current results in an increase in the optical gain and hence the output power increases. At a gain section current of 220 mA and SOA current of 250 mA, the output power was 130 mW. For the SOA currents above 250 mA, there is no further increase in the output power of the device. This is due to the output power roll-over of the SOA at higher injection currents, which will be explained in more details in Chapter 7 (Section 7.3). Figure 6.13 (Right) shows the output power contour map as a function of gain current and SOA current, while the DBR current is fixed at 5 mA. The region enclosed by dotted black lines in the output power map indicates the output power of the device corresponding to the mode locking region of the device. The output power of the device for SOA injection currents from 0 to 280 mA at $I_{gain} = 220$ mA, $I_{DBR} = 5$ mA and $V_{SA} = -4$ V is shown in Figure 6.14.
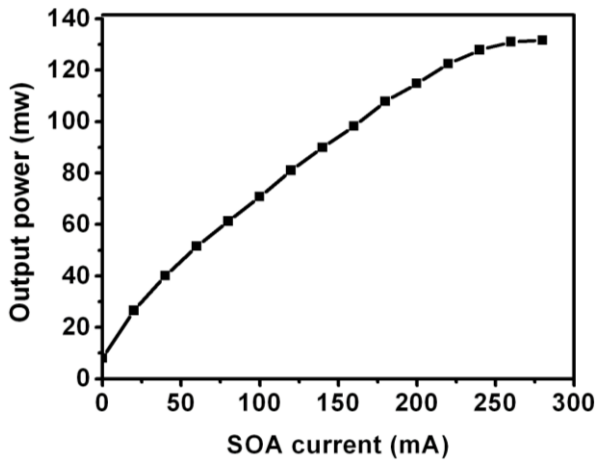
Figure 6.14: Measured output power versus different SOA currents for $I_{gain} = 220$ mA, $I_{DBR} = 5$ mA and $V_{SA} = -4$ V.

The maximum output power obtained from these devices was limited by the saturation of the SOA. A tapered SOA design was employed to increase the saturation output power of the SOAs by increasing the modal cross-section; this will be explained in details in the next chapter.

6.6   Far-field Measurements

The far-field pattern of these devices was measured directly at the SOA facet with the detector placed at around 5 mm away from the device facet and the beam intensity as a function of

angular position was measured by a rotating detector. The device was mounted on a copper heat sink with the temperature controlled at 20°C and driven with the CW current.
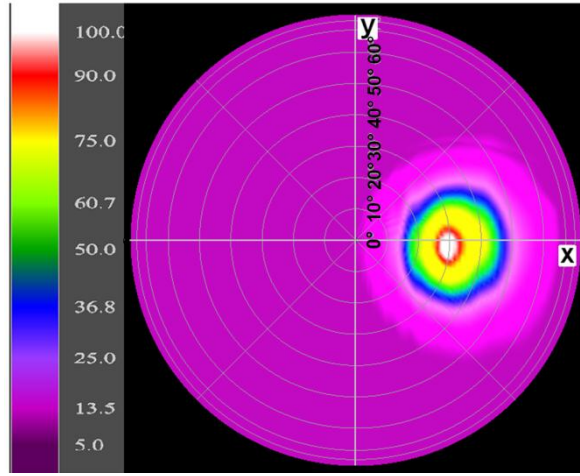
Figure 6.15: 2-D picture of the measured far-field at the SOA facet of the device at I_{gain}= 200 mA, I_{DBR}= 5 mA, I_{SOA}= 250mA and V_{SA}= - 4 V.

From Figure 6.15, one could clearly see that the output is single moded, and symmetric, and due to the 10° tilt angle of the SOA, the output is 32° offset in the horizontal direction, which is consistent with the calculated value of 32.4°. Figure 6.16 shows the far-field profile in the horizontal and vertical direction, respectively, as a function of SOA current at I_{gain}= 200mA, I_{DBR} = 5 mA, I_{SOA}= 250 mA and V_{SA}= - 4 V.
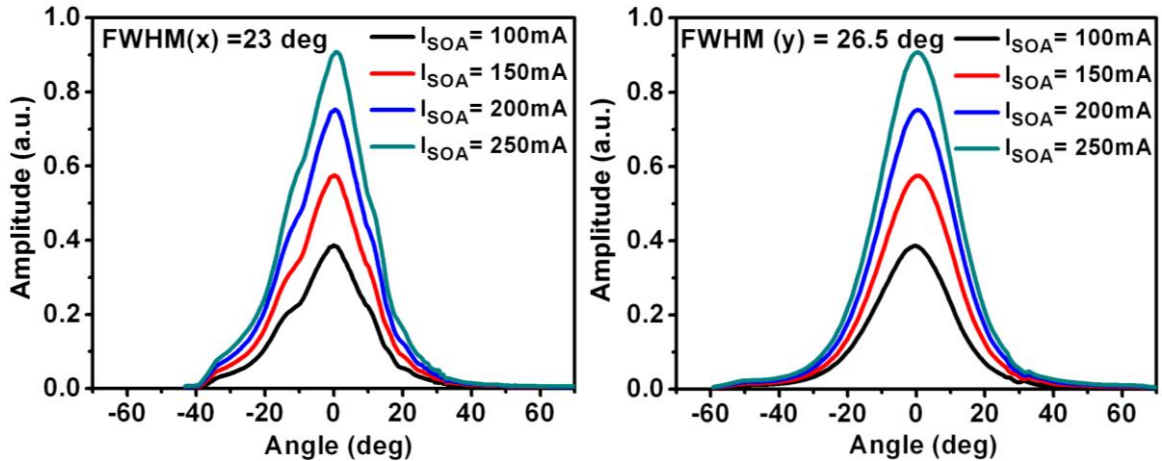
Figure 6.16: Measured far-field at the SOA facet of the device in horizontal direction (Left) and vertical direction (Right) at I_{gain}= 200 mA, I_{DBR}= 5 mA, I_{SOA}= 250 mA and V_{SA}= - 4 V.

The measured FWHM of the far-field in the horizontal and vertical direction is 23° and 26.5° respectively, which is consistent with the simulation results presented in Chapter 4 (Section

4.14). Furthermore, an increase in the SOA current does not affect the beam divergence in the horizontal and vertical directions.

6.7 Optical Spectra Analysis

The optical spectra shown in Figure 6.17 were measured at both the SA and SOA facets of the device under the optimal mode locked operation. The figure shows that the measured optical spectrum is smooth and symmetric. For measurements at the SA facet, the SOA section was kept floating. As shown in the plot, the optical spectrum at the SA facet of the device is centred at slightly lower wavelengths (1553.8 nm) than that measured at the SOA facet (1555 nm) with SOA biased at 250 mA. This suggests thermally induced red-shift due to heating up of the device, when the SOA section is biased. The mode spacing of the optical spectrum is around 0.31 nm, which corresponds to repetition frequency of 38 GHz. The 3 dB bandwidth of the optical spectrum at the SA facet of the device is 0.95 nm, while that at the SOA facet is 1.14 nm. The main cause for larger spectral bandwidth at the SOA facet is the self phase modulation (SPM) in the SOAs. This can be explained by the energy of the input pulse approaching the saturation energy of the gain medium, which leads to the depletion of the carrier density. The change in the carrier density causes changes in the refractive index, which causes phase modulation to the optical pulse. The SPM induces frequency chirp on the optical pulses, which results in an increase in the spectral bandwidth beyond the pulse transform limit [11].
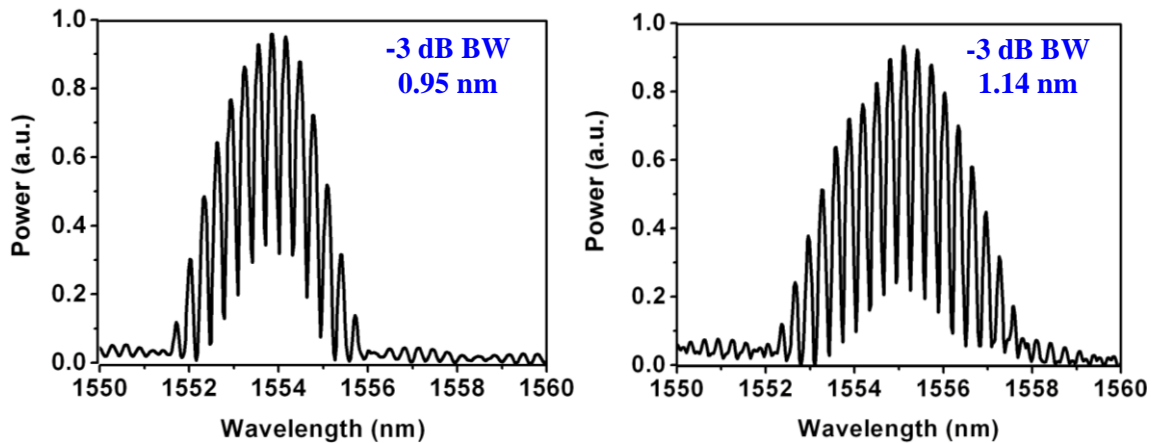
Figure 6.17: Measured optical spectra at the (left) SA side of the device at I_{gain}= 200 mA, I_{DBR}= 5 mA and V_{SA}= - 4 V and the (right) SOA side at I_{gain}= 200 mA, I_{DBR}= 5 mA, I_{SOA}=250 mA and V_{SA}= - 4V.

Figure 6.18 shows the peak wavelength dependence on the DBR section current. The peak wavelength initially experiences a blue-shift when the DBR current was increased from 0 to 4 mA. This is due to the band filling effect. The total wavelength jump for the DBR current range from 0 mA to 4 mA is 0.6 nm, which corresponds to two longitudinal modes. At higher DBR currents, the thermal effects caused by the injected carriers causes a slight red-shift in the emission wavelength of the device [10].
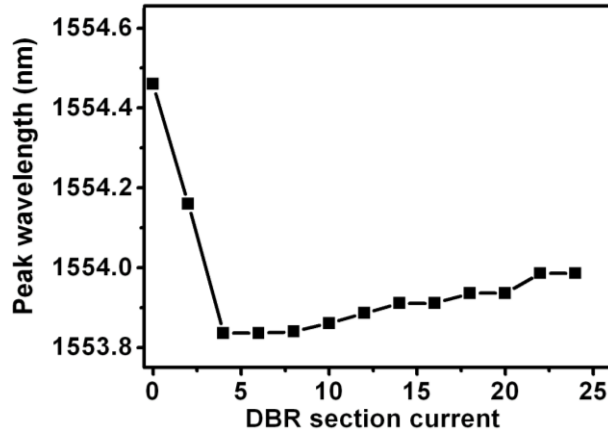
Figure 6.18: Emission peak wavelength versus DBR section current measured at the SA side of the device at I_{gain}= 200 mA, V_{SA}= - 4 V and SOA floating.

To see the difference in the laser's performance with and without the integration of SOA, the optical spectra were measured at both the SA and SOA facets of the device. Figure 6.19 shows the map of the optical spectra peak wavelength as a function of gain current and SA reverse bias, measured at the SA (left) and SOA (right) facets respectively. In the MLLs, stable mode locking occurs when the gain peak coincides with the absorber band edge [12].
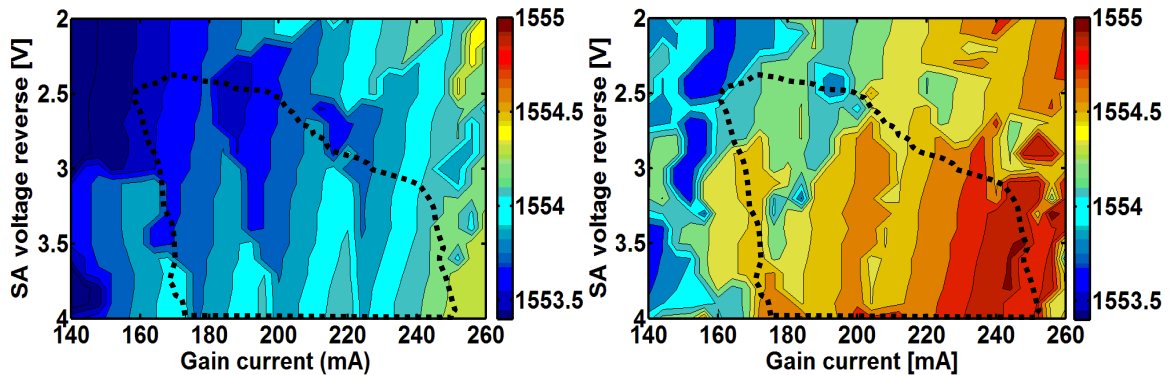
Figure 6.19: Map of peak wavelength of measured optical spectrum as a function of gain current and SA reverse bias at I_{DBR}= 5 mA from (Left) SA facet and (Right) SOA facet of the device with I_{SOA}= 250 mA.

The peak wavelength corresponding to the mode locking regime is indicated by the region enclosed by the black dotted lines in the peak wavelength map. An increase in the gain section current causes an overall red shift in the peak wavelength. It is anticipated that the observed tuning (around 0.3 nm) in the peak wavelength with increase in the gain current is due to the thermal tuning of the cavity modes inside the DBR stop-band.

6.8 RF Spectra Analysis

The radio frequency (RF) spectra of a MLL confirm the pulse repetition frequency when the laser is mode locked. The RF spectrum measured under the mode locking conditions at the SA and SOA facets of the device is shown in Figure 6.20.
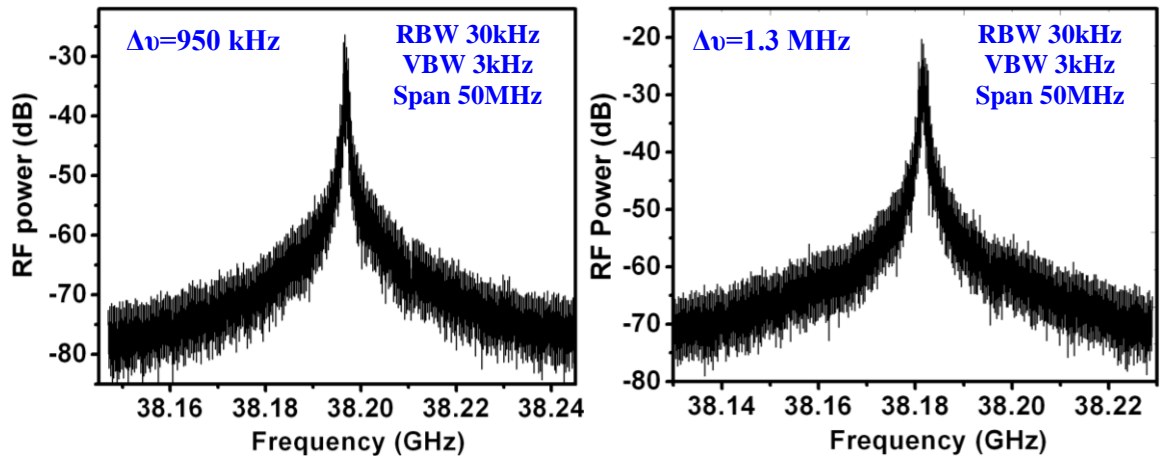
Figure 6.20: Measured RF spectrum at the (left) SA facet and (right) SOA facet of the device at I_{gain}= 200 mA, I_{DBR}= 5 mA, I_{SOA}= 250 mA and V_{SA}= - 4V.

The RF spectra in the figure show the RF peak at around 38.20 GHz (left) and 38.18 GHz (right), corresponding to the length of the designed cavity. The amplitude of the RF peak measured at both the facets is around 45 dB above the noise floor. The 3 dB linewidth of the RF spectrum measured at the SA facet is 950 kHz, while that measured at the SOA facet under the same bias conditions is 1.3 MHz (measured with 30 kHz resolution bandwidth). Figure 6.21 shows the repetition frequency versus DBR section current for a fixed gain current and SA reverse voltage. The plot shows that the repetition frequency decreases with increasing DBR current. A tuning range of 20 MHz was obtained when the DBR current was varied from 0 to 24 mA, which is consistent with the results reported in [13]. The decrease in the repetition frequency with increasing the DBR current is caused by the increase in the DBR effective length due to lower absorption losses [14].
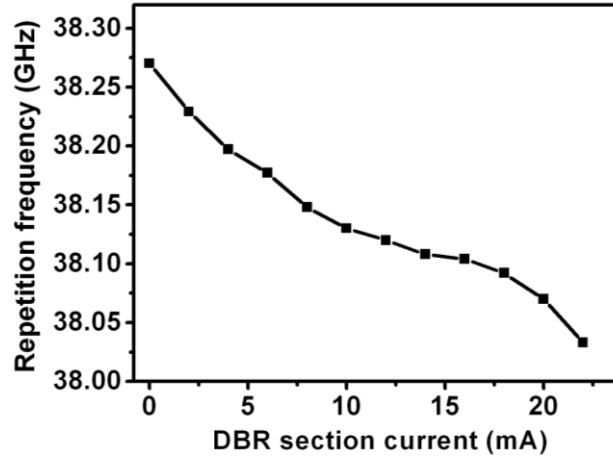
Figure 6.21: Repetition frequencies versus DBR section current measured at the SA facet at I_{gain}= 200 mA, V_{SA}= - 4V, and SOA floating.

To evaluate the range of mode locking and analyse the difference in the laser's performance with and without the use of integrated SOA, the RF spectra at both the SA and the SOA facets of the device were recorded for gain section current ranging from 140 to 260 mA and SA reverse voltage from 2 to 4 V. Figure 6.22 shows the map of the RF peak amplitude as a function of the gain section current and absorber reverse voltages. As mentioned earlier, for optimal mode locking the RF peak-to-noise ratio > 25 dB. The region enclosed by the black dotted lines in the Figure 6.22 indicates the optimal mode locking region. The figure shows that at both the SA and the SOA facets, there is a similar and well defined region of optimal mode locking with RF peak power of around 45 dB above the noise floor.

Figure 6.22: Map of RF peak amplitude as a function of gain current and SA reverse bias at I_{DBR}= 5 mA from (left) SA facet and (right) SOA facet of the device with I_{SOA}= 250 mA.

The high RF peak power at both the SA and SOA facets is achieved for gain section current range of around 180 to 250 mA and SA reverse voltage range from 2.5 to 4 V. From the

figure, it is clear that the RF spectra at the SOA facet exhibit slightly higher RF peak powers, which is due to the higher output power of the device at the SOA facet.

Similarly, the repetition frequency of the device measured at both the SA and SOA facets are mapped in Figure 6.23 for a range of gain currents and absorber reverse voltages.
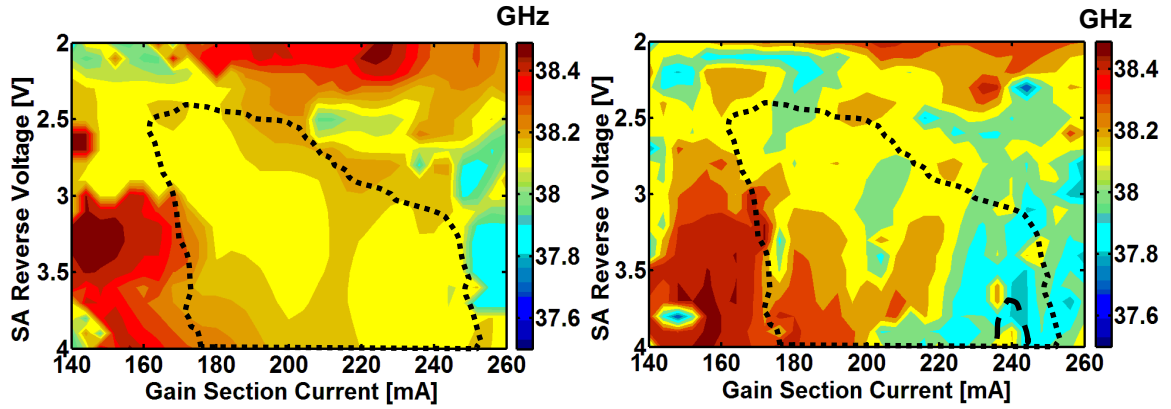
Figure 6.23: Map of the repetition frequency as a function of gain section current and SA reverse bias at I_{DBR}= 5 mA at the (Left) SA facet and (Right) SOA facet of the device for I_{SOA}= 250 mA.

The region enclosed by the black dotted lines in RF repetition frequency maps indicates the mode locking region. Typical trends were observed, such as repetition frequency tuning by varying the gain section currents and the absorber reverse voltages. The large frequency shifts (several hundred MHz) are not caused only by the carrier density induced refractive index changes. The main reason for these frequency shifts is the detuning of the cavity roundtrip frequency by the gain/absorption saturation effects [9]. In a low unsaturated gain regime, for a fixed SA reverse voltage, an increase in the gain current causes an increase in the pulse energy and hence decrease in the repetition frequency. Similarly, for a fixed gain current, an increase in the SA reverse voltage causes decrease in the pulse energy and thus increase in the repetition frequency [15].

6.9 Pulse Width Analysis

The emitted pulses from the device were measured using a second harmonic generation (SHG) intensity autocorrelator, as explained in Chapter 5 (Section 5.3.3). The pulse train of the emitted pulses at the SOA facet of the device, under the mode locking operation is shown in Figure 6.24 (left). The repetition rate of these devices, i.e. 38 GHz was supported by the spacing between the two adjacent pulses in the pulse train. The most appropriate fitting for the autocorrelator traces emitted at the SOA facet was found to be Gaussian. A singulated pulse

emitted at the SOA facet, with a Gaussian fit and corresponding FWHM is shown in Figure 6.24 (right). After deconvolution, the pulse duration was found to be 3.3 ps.
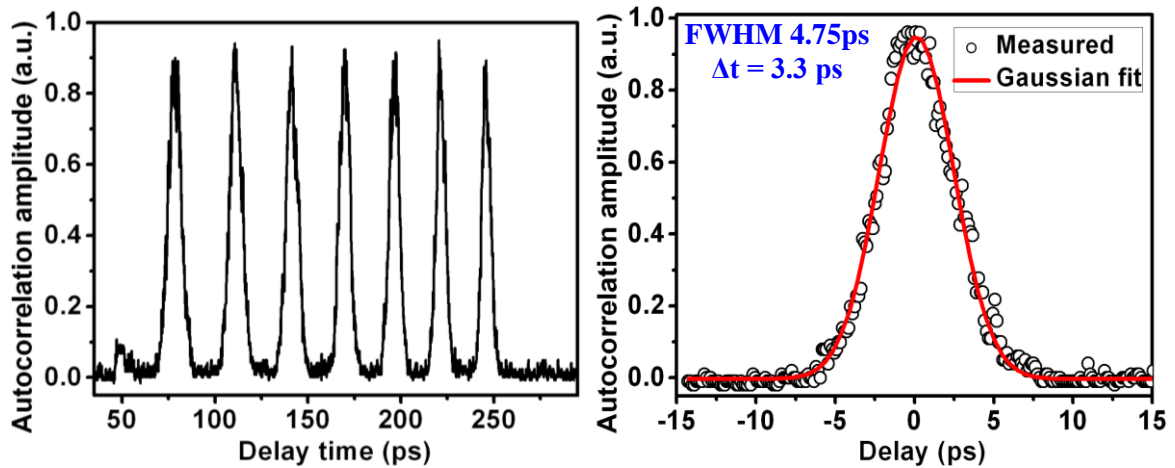
Figure 6.24: Measured SHG intensity autocorrelation pulses at the SOA facet of the device at I_{gain}= 200 mA, I_{DBR}= 5 mA, I_{SOA}= 250 mA and V_{SA}= - 4V.

The pulse width measured at the SA facet under the same bias conditions was 3 ps assuming a sech^2 fit. In order to see the correlation between the mode locking regions indicated by the RF spectra and the pulse widths, the SHG autocorrelation traces were recorded at both the SA and SOA facets for a range of gain currents and SA reverse voltages. Figure 6.25 shows the approximate pulse width contour map at both the SA and SOA facets as a function of gain current and absorber reverse voltage.
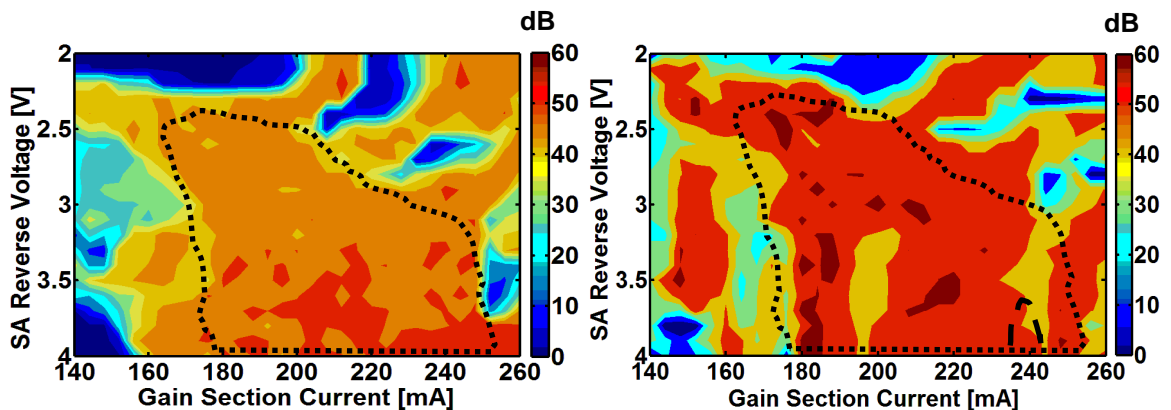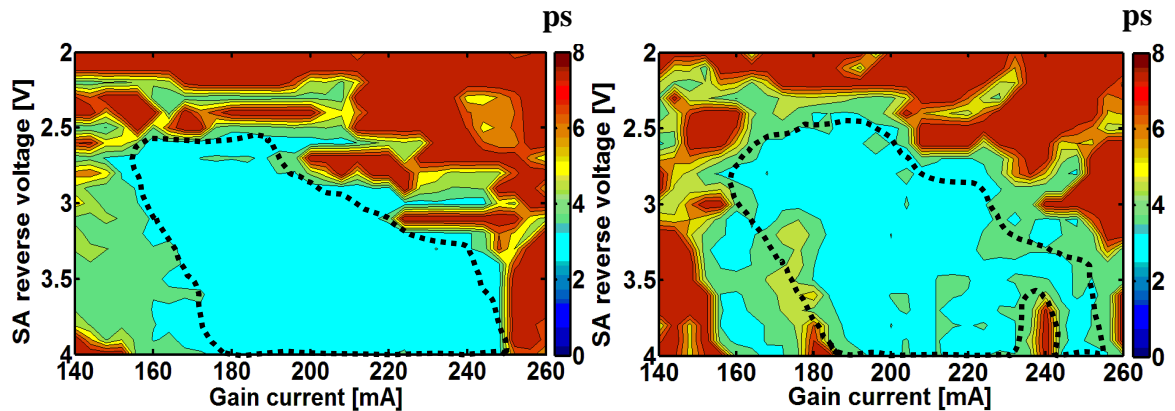

Figure 6.25: Map of pulse width as a function of gain current and SA reverse bias at I_{DBR}= 5 mA from (Left) SA facet and (Right) SOA facet of the device with I_{SOA}= 250 mA.

The region enclosed by the black dotted lines in the pulse width maps represent the range of mode locking of the device. The contour plots of the pulse width shows the similar mode locking trends to those obtained from the RF peak power maps. From the pulse width contour

maps, it is clear that short pulses (< 4 ps) were obtained at both the SA and SOA facets for a wide range of gain section currents and SA reverse voltages. The pulse width map obtained at the SOA facet indicates no significant difference from that obtained at the SA facet, which suggests minimal effects on the pulse widths due to the integration of SOA. Typical trends were observed, i.e. pulse broadening with increased gain section current and pulse shortening with increase in the SA reverse bias. The pulse broadening with increasing gain section current is caused by the SPM and pulse shortening with increase in absorber reverse voltage is due to the reduction in absorber recovery time [16].

6.9.1   Effect of SOA Current on the Pulse Width

In order to observe the effect of SOA injection current on the measured pulse duration, the pulse width was measured for SOA currents ranging from 100 to 260 mA. The output power roll-over of the SOA occurs at an injection current of around 260 mA. Figure 6.26 shows the autocorrelation pulse width as a function of SOA current and SA reverse voltage for gain current of 200 mA and DBR current of 5 mA respectively.
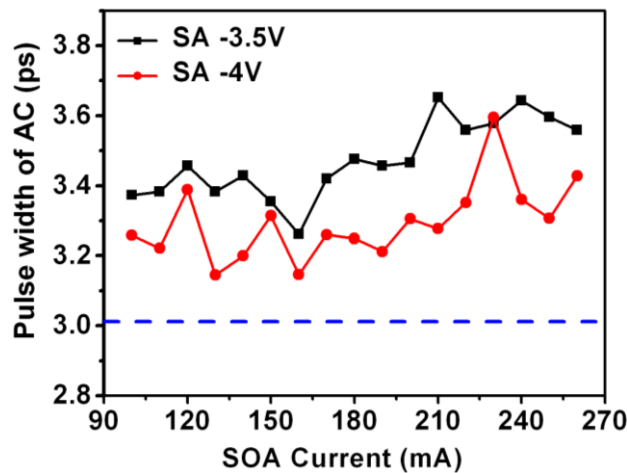
Figure 6.26: Measured pulse widths at the SOA facet of the device as a function of SOA injection current at I_{gain}= 200 mA, and I_{DBR}= 5 mA. The blue dotted line represents the pulse width measured at the SA facet.

The dashed blue line corresponding to 3 ps in the plot shows the pulse width of the autocorrelation trace measured at the SA facet of the device with SOA unbiased. From the plot, it can be clearly seen that there is a trend of increase in the pulse width with increase in the SOA current. This is likely to be caused by the SPM and the gain compression based pulse distortion, which will increase with increasing the SOA optical gain. However, increase in

pulse width with increasing the SOA current is not very significant, as an increase in SOA current from 100 to 260 mA causes only 0.2 ps increase in the pulse width.

6.10 Output Peak Power and Time Bandwidth Product

The output peak power (black colour) and the TBP (red colour) as a function of the SOA current for I_{gain}= 200 mA, I_{DBR}= 5 mA and V_{SA}= - 4 V is shown in Figure 6.27.
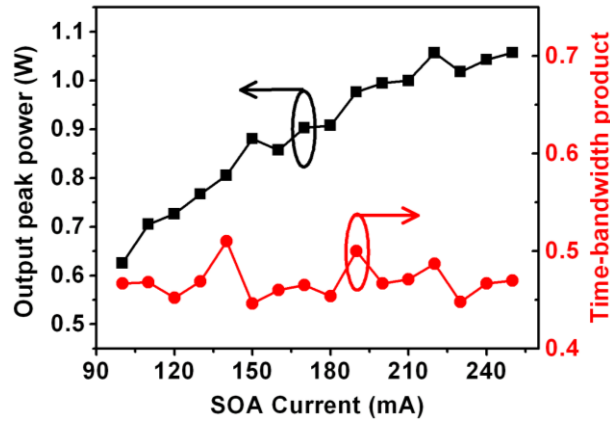
Figure 6.27: Measured output peak power and time bandwidth product as a function of SOA injection current at the SOA facet of the device for I_{gain}= 200 mA, I_{DBR}= 5 mA and V_{SA}= - 4 V.

As expected, the output peak power obtained at the SOA facet increases with increasing the SOA current and gets constant at SOA current of 250 mA. The plot shows that the TBP for a wide range of the SOA injection currents is constant at around 0.47. Assuming Gaussian shaped pulses, this shows near transform limited output over a wide range of SOA injection currents. The pulse energy and the output peak power with I_{gain}= 200 mA, I_{DBR}=5 mA and V_{SA}= - 4 V was 3.42 pJ and more than 1 W, respectively. The pulse energy and the output peak power measured at the SA facet of the device under the same bias conditions were found to be 0.74 pJ and 240 mW. By integrating SOA with the MLL, the output peak power is increased by a factor of 4.5, without degrading the mode locking performance of the device.

6.11   Chapter Summary

The main results including the *L-I* curves, optical spectra, optical gain and saturation output power characterisation of standalone SOAs were obtained for a comparison. These devices showed small signal chip gain of 17 dB and saturation output power of 15.8 dBm. The simulation results of losses in curved waveguides were presented. The design and the main

results obtained from the mode locked DBR lasers with integrated SOAs were also presented. The integration of SOA at the output of the DBR-MLL increased the average output power to 130 mW and corresponding peak power > 1 W. The effect of the integrated SOA on the mode locking performance of the laser was investigated. The measured far-field pattern for different SOA currents showed symmetric and single mode output, with divergence angles of 23° and 26.5° in horizontal and vertical directions, respectively, which is consistent with the simulation results. The recorded optical spectra, RF spectra, and pulse duration at both the SA and SOA facets showed minimal effects of integrated SOA on the mode locking performance of the laser. The shortest pulse obtained using the Gaussian fit was 3.3 ps, with the corresponding 3 dB optical bandwidth of 1.14 nm. The device emits nearly transform limited output (TBP ~ 0.47) for a wide range of SOA injection currents. The output power could be further improved by optimising the waveguide design to further increase the modal cross-section or by improving the heat sinking of the devices. The output peak power could be further increased by increasing the reflections bandwidth of the intra-cavity reflector, which would reduce the pulse width and hence increase the output peak power. Another way to increase the peak power is to reduce the repetition frequency by designing longer cavities. Increase in the saturation output power would also cause an increase in the output power, which could be achieved by using tapered SOAs. Results of the MLLs integrated with tapered SOAs are presented in the next chapter.

6.12   References

1.   Mitsuo Fukuda, *Optical semiconductor devices*. 1999, USA: John Wiley and Sons. p. 137-139.

2.   Lorenzo Occhi, *Semiconductor Optical Amplifiers made of Ridge Waveguide Bulk InGaAsP/InP: Experimental Characterisation and Numerical Modelling of Gain, Phase, and Noise*, in Eidgenössische Technische Hochschule Zürich. 2002: Zürich.

3.   Ken Morito, et al., *A Broad-Band MQW Semiconductor Optical Amplifier With High Saturation Output Power and Low Noise Figure.* IEEE Photonics Technology Letters. 2005. 17(5).

4.   Yoshihisa Yamamoto, *Coherence, Amplification, and Quantum effects in Semiconductor Lasers*. 1991: John Wiley and Sons, Inc.

5.   Niloy K Dutta and Qiang Wang, *Semiconductor optical amplifiers*. 2006, Singapore: World Scientific Publishing.

6.   Yoshihisa Yamamoto., *Coherence, Amplification, and Quantum effects in Semiconductor Lasers*: John Wiley and Sons, Inc.

7.   B. M. A. Rahman, et al., *Bending loss, transition loss, mode coupling and polarization coupling in bent waveguides*, in Proc. of SPIE Vol. *6996 69960O*. 2008.

8.   V. Subramanian, et al., *Measurement of mode field profiles and bending and transition losses in curved optical channel waveguides.* Journal of Lightwave Technology, 1997. 15(6): p. 990-997.

9.   R. Kasier and B. Huttl, *Monolithic 40-GHz Mode-Locked MQW DBR Lasers for High-Speed Optical Communication Systems.* IEEE Journal of Selected Topics in Quantum Electronics. 2007 13(1): p. 125-135.

10.   Lianping Hou, et al., *Monolithic 40-GHz Passively Mode-Locked AlGaInAs–InP 1.55-.* IEEE Photonics Technology Letters. 2010. 22(20): p. 1503-1505.

11.   Derickson, D.J., et al., *Short pulse generation using multisegment mode-locked semiconductor lasers.* IEEE Journal of Quantum Electronics. 28(10): p. 2186-2202.

12.   D. Kunimatsu, S. Arahira, and Y. Ogawa, *Passively Mode-Locked Laser Diodes with Bandgap-Wavelength Detuned Saturable Absorbers.* IEEE Photonics Technology Letters, 1999. 11(11): p. 1363-1365.

13.   Lianping Hou, et al., *10-GHz Mode-Locked Extended Cavity Laser integrated With Surface-Etched DBR Fabricated by Quantum-Well Intermixing.* IEEE Photonics Technology Letters. 2011. 23(2): p. 82-84.

14.   I. Ogura, et al., *Precise operation-frequency control of monolithic mode-locked laser diodes for high-speed opitcal communication and all-optical signal processing.* Opt. Quantum Electron, 2001. 33: p. 709-725.

15.   Steven McMaster, *Monolithic Integrated Mode-Locked Ring Lasers and Mach-Zehnder Interferometers in AlGaInAs*, in Department of Electronics and Electrical Engineering, 2010, University of Glasgow.

16.   R. Green, et al., *Fast saturable absorption and 10 GHz wavelength conversion in Al-quaternary multiple quantum wells.* Optics. Express, 2011. 19: p. 9737-9743.

Chapter 7

Mode Locked Lasers with Integrated Tapered SOAs: Results

7.1 Introduction

This chapter presents the device design and the results obtained from MLLs monolithically integrated with tapered SOAs. The tapered SOAs were integrated with the DBR-MLLs at the output in a similar way to the devices discussed in Chapter 6. Comparing to the single mode SOAs, the tapered SOAs results in higher saturation output power and hence higher output power of the devices integrated with tapered SOAs. These devices were based on the 3-QW active region epitaxial material due to its higher output power and better mode locking performance, as described in Chapter 5. An overview of tapered SOAs and the simulation results are presented. Heat sinking performance of the devices using aluminium nitride (*AlN*) sub-mounts with gold-tin (*AuSn*) eutectic soldering is also discussed. Comparison of the output power of the ridge waveguide lasers mounted on the conventional brass sub-mounts and *AlN* sub-mounts using *AuSn* soldering is given in Section 7.3.1. This is followed by the far-field simulation and measurement results of the devices. The characterisation results of the MLLs with integrated 2°-tapered SOAs, measured at both the SA and SOA facets are presented. Finally, the results obtained from the MLLs monolithically integrated with 6°-tapered SOAs are presented.

7.2 Tapered Semiconductor Optical Amplifiers

In order to improve the saturation output power of SOAs, different design geometries such as broad area geometry [1] and tapered waveguide geometry [2, 3] have been used. In the tapered waveguide devices, the waveguide width increases in lateral direction towards the output facet as shown in Figure 7.1. When the input light enters the waveguide of a tapered SOA, it is subjected mainly to two effects, i.e. amplification of the input light by the gain medium and the optical mode expansion due to the diffraction as it travels towards the output facet. The optical mode in the tapered devices is guided in the vertical direction and expanded in the horizontal direction due to the waveguide geometry. According to Equation 4.11, an increase in the mode cross-sectional area due to the tapered waveguide structure will result in an improved saturation output power. Tapered SOAs can produce higher saturation output powers, and lower facet reflectivity due to the mode expansion. An improvement of 7 dB in the saturation output power for a tapered SOA, as compared to the conventional narrow ridge waveguide SOA was reported by G. Bendelli et al., [2]. To provide low loss transition, the optical mode should propagate adiabatically in the tapered structure, i.e. the lowest order mode should propagate through the waveguide without cumulative power transfer to the higher order modes. The tapered SOAs allow adiabatic expansion of the optical mode, while still keeping a single mode operation.
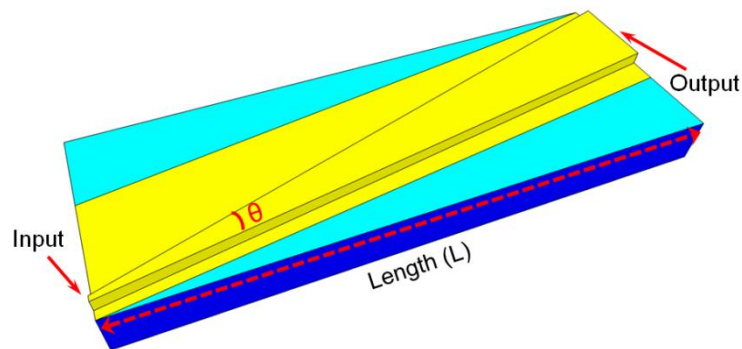
Figure 7.1: Schematic of a tapered SOA with the input and output facets indicated.

These devices should be designed to provide lower optical losses in the tapered waveguide section. The internal taper angle (θ) should be designed to allow quasi adiabatic single mode propagation. If the designed taper angle is larger than the divergence angle of the input light, the injected carriers in the outer gain regions do not contribute to stimulated emission and emits spontaneously or recombine non-radiatively. Similarly, if the designed taper angle is

smaller than the divergence angle of the input light, the outer parts of the light are absorbed, while the inner parts are amplified which reduces the output beam quality [4]. The taper angle depends on the divergence of the input light, which is determined by the refractive index step (Δn). For smaller divergence angles, smaller taper angles are required and vice versa. In a situation where the optical mode completely overlaps with the gain region, reduction in spatial hole burning (SHB), self-focusing and high quality output is obtained [4]. The main issues related to the tapered SOAs are multimode emission and non-linear effects such as self-focussing and filamentation, which degrades the beam quality of the device. During mode propagation through the tapered waveguide, the gain in the middle of the waveguide is saturated due to peak intensity of the mode. The gain saturation in the middle causes reduction in carrier density through gain saturation, which in turn increases the refractive index in the middle and causes self-focussing, leading to filamentation. For a given epitaxial structure design, these non-linear effects depends on the device geometry such as taper angle, ridge waveguide width, refractive index step (Δn) and the total length of the device. Under pulsed current conditions, these non-linear effects are caused only by the carrier induced lensing whereas in the CW current operation, both the thermal and carrier induced effects come into play. Therefore, devices in the CW current operation are more susceptible to self-focussing and filamentation [4]. To allow CW operation of tapered SOAs with a good output beam quality, careful designing of the device geometry is of paramount importance. The simulation results reported in [4] shows that 3° tapered devices provides better beam quality. The epitaxial structure used in this work results in an increased mode spot size, as explained in Chapter 4 (Section 4.5) and hence lower diffraction angles. The lower diffraction angles require shallow taper angles to reduce the non-linear effects in the devices. Therefore, we designed tapered SOAs with shallow (2°) taper angle, which would reduce the non-linear effects in the device and allow CW operation, without degrading the output beam quality of the device. The tapered SOAs were monolithically integrated with the DBR-MLLs in a similar way to the devices discussed in Chapter 6. To compare the performance and beam quality, MLLs with integrated 6° tapered SOAs were also fabricated and tested, as discussed in Section 7.9.

To investigate the propagation of the optical mode inside tapered SOAs, 3-D beam propagation simulations were carried out using a commercially available software, BeamPROP. Using this simulation tool, fundamental mode for the 2.5 μm wide ridge waveguide laser was computed and then launched into the input waveguide of the 2° tapered

SOA. The simulations results showing the optical mode expansion during the propagation (along the z-direction) inside the tapered SOAs are shown in Figure 7.2.
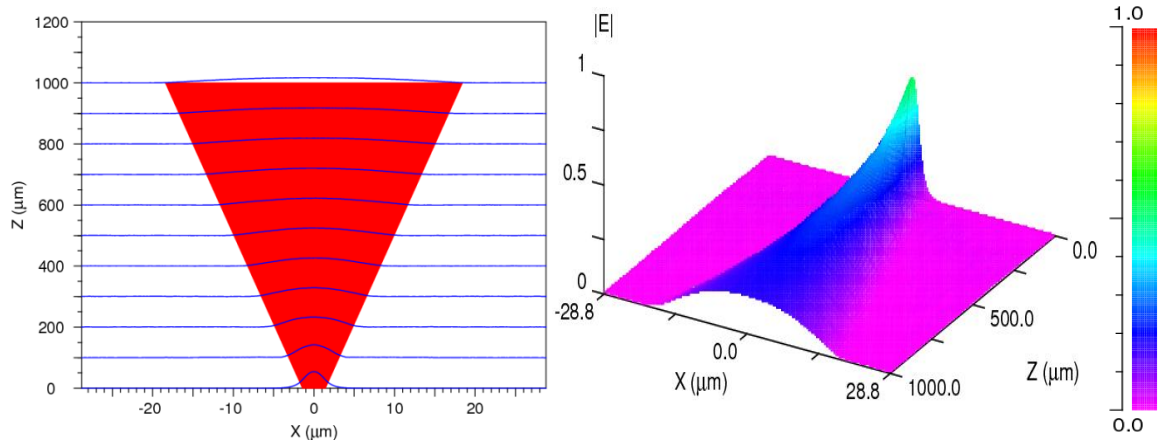
Figure 7.2: 3-D beam propagation simulation results showing the optical mode expansion during propagation along z-direction inside the 2° tapered SOA.

7.3 Heat Sinking of the Devices

To obtain high output power from semiconductor lasers, efficient thermal management of the devices is required. Generally, high power operation of lasers is obtained at high injection currents, which lead to production of large heat flux in the device. To remove heat efficiently from the lasers, design solutions such as buried heterostructure designs could be used. The lasers performance is strongly dependent on the thermal management of the devices. Devices operating at 1.55 µm have worst temperature performance due to variety of reasons including the Auger recombination, which is a dominant non-radiative recombination mechanism in long-wavelength semiconductor lasers. The heat flux is generated in the active region of the laser which, flow through the cladding layers, semiconductor substrate, solder layers, sub-mount and then finally absorbed by the heat sink [5]. An efficient external thermal management is thus quite important for devices heat dissipation. Laser diodes are commonly mounted on a high thermal conductivity copper (*Cu*) heat sink and the temperature of the heat sink is actively controlled and monitored. The most critical part of thermal management of semiconductor lasers is how they are mounted to its heat sink. Commonly, laser bars are manually mounted epitaxial-side-up on brass sub-mounts using conductive epoxy. The brass sub-mounts take the generated heat away from the device and pass it to the *Cu* sink thus reducing the thermal impedance and temperature of the device. The thermoelectric cooler

(TEC) connected to the *Cu* heat sink dissipate the heat of the laser and a thermister placed in the *Cu* heat sink monitors and control the temperature of the heat sink. The length and the width of the brass sub-mounts need to be carefully designed. If the width of the sub-mount is shorter than that of a laser bar, the heat dissipation from the overhanging regions of the lasers bars will be insufficient and may degrade the device performance. The soldering interface and the sub-mounts should provide sufficient mechanical stability, low electrical resistance and effective heat sinking to the devices. Different sub-mounts materials such as silicon (*Si*), copper (*Cu*), Diamond and Aluminium Nitride (*AlN*) has been widely used for mounting of laser bars. Comparing to other options, *Cu* is cost effective with high thermal conductivity (~393W/mK at RT). The use of *Cu* sub-mounts is not a preferable choice due to its co-efficient of thermal expansion (CTE) (Cu ~ 17 x 10^6/K) mismatch to that of InP (CTE of InP~ 4.5 x 10^{-6}) [6]. Such a large CTE mismatch leads to stress in the lasers structures, which reduce the devices lifetime and degrade the performance. The soldering material used to mount laser bars to the sub-mounts is an important component. Normally, devices are soldered to *Cu* using indium (*In*) as a solder. The *In* requires aggressive pre-processing such as acid etching before soldering to allow flux-free soldering. Lasers mounting on the *Cu* heat sinks using *In* solder and flux reduces the devices reliability and reproducibility [6]. Other solders such as *SnPb* and *Pb*-free which are mostly used, exhibits low stress but insufficient bonding strength and low creep resistance. Low creep resistance of the solders causes reduction in the fiber coupling efficiency of the devices. To obtain reliable device performance with efficient heat sinking, the bonding stress and the number of voids in the bonding should be minimized. Uniform solder interface, reduced solder voids, greater creep resistance and excellent mechanical and thermal properties could be obtained using Gold-Tin (*AuSn*) eutectic solder [7]. The *AuSn* eutectic solder has a melting point of 283°C and is composed of 80 % *Au* and 20 % *Sn*. Further, *AuSn* has the advantage of low oxidation rate which allows fluxless soldering. Since *AuSn* is a hard solder with high melting point (283°C), a bonding substrate material (sub-mount) with CTE matched between the laser and the sub-mount material is necessary to reduce the bonding stress. Furthermore, the sub-mount material should provide high thermal conductivity to allow efficient thermal management. Due to these demands, Aluminium nitride (*AlN*) was selected as sub-mount material. The *AlN* sub-mounts has high thermal conductivity (~180W/mK) and CTE value of 4.5 x 10^{-6}/K, which is perfectly matched to that of the *InP* [8]. Further, the *AlN* is an electrical insulator and allows the formation of electrical interconnects on the sub-mounts. Properties of *AlN,* such as high purity, superior

micro-structural and chemical uniformity leads to very consistent properties [9]. Different metal coatings could be applied to the *AlN* sub-mounts for reliable soldering and wire-bonding purposes. The metal layers are deposited to full-fill three general requirements: (1) surface adhesion, (2) diffusion barrier, which should provide stable bond with the contact layer and non-reactive to *Sn* and (3) cap layer, which is used to prevent oxidation of the surface prior to reflow. Generally, for the ceramic sub-mounts, *Ti/Pt/Au* (adhesion/barrier/cap) are used to full-fill the above mentioned requirements.

The *AlN* sub-mounts and *AuSn* soldering provides efficient heat sinking and offers benefits of high scalability and reliability. In this work, *AlN* sub-mounts with pre-deposited top face covered with *Ti/Pt/AuSn/Au* (100nm/60nm/3000nm/50nm) and bottom face covered with *Ti/Pt/Au/Ti/Pt/AuSn/Au* (100nm/200nm/1000nm/40nm/60nm/3000nm/50nm) were used to get better heat sinking of the devices. The laser devices were epi-layer-up soldered to the top face of the *AlN* sub-mount using Cammax EDB-80 die bonder and mounted on the *Cu* heat sink using silicon thermo-conductive paste. The schematic of a device mounted on the *AlN* sub-mount using *AuSn* soldering, and placed on *Cu* heat sink is shown in Figure 7.3. The Thermo-conductive paste applied in the interface between the ceramic sub-mount and the *Cu* heat sink improves the thermal conductivity between the device and the heat sink.
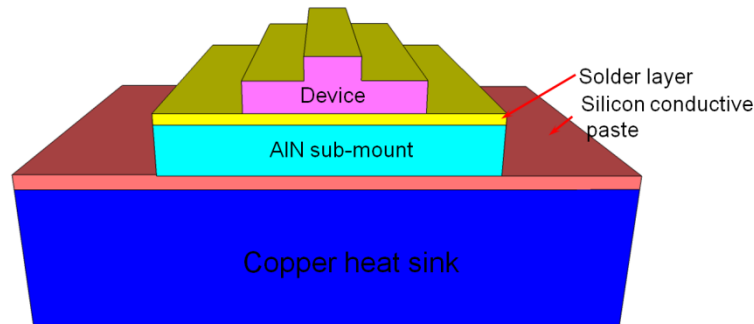
Figure 7.3: Schematic of a device mounted on *AlN* sub-mount using *AuSn* soldering.

7.3.1 Performance of Device Mounted on *AlN* Sub-mounts Using *AuSn* Solder

To compare the heat sinking performance of the *AlN* sub-mounts and the brass sub-mounts, 1.7 mm long ridge waveguide lasers were mounted p-side up on *AlN* sub-mounts using *AuSn* soldering and brass sub-mounts using conductive epoxy. In order to assess the optical and electrical performance of the devices mounted on both different schemes, the *L-I* and *V-I* curves were recorded under CW current conditions. Devices were placed on a temperature

controlled *Cu* heat sink and thermo-conductive paste was applied to the interface between the sub-mounts and heat sink to improve the thermal conduction.
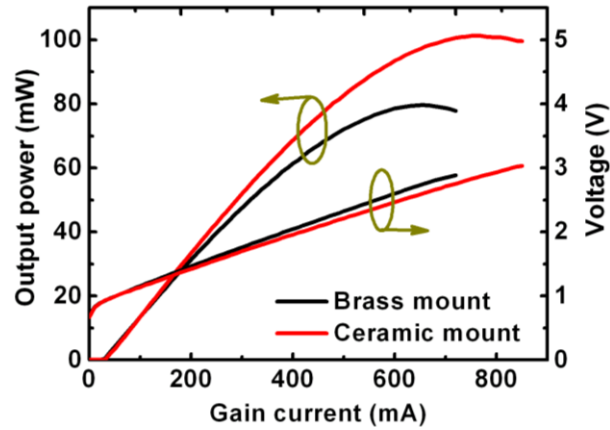
Figure 7.4: *L-I-V* comparison of 1.7 mm long ridge waveguide lasers mounted on *AlN* and brass sub-mounts.

Figure 7.4 shows the *L-I-V* curves of the ridge waveguide lasers mounted on *AlN* sub-mounts (indicated by red colour) and brass sub-mounts (indicated by black colour). From the *L-I* curves, it is clear that the threshold current for the devices in both the schemes is around the same. The devices mounted on the *AlN* sub-mounts exhibits higher slope efficiency. For the devices mounted on the brass sub-mounts, the output power roll-over occurs at an output power of 78 mW, while for the devices mounted on the *AlN* sub-mounts using *AuSn* soldering, the power roll-over occurs at an output power of around 100 mW. The power roll-over in the semiconductor lasers is mainly due to the device self heating under the CW current operation. The self heating of the device increases optical losses and non-radiative recombination, which enhances the power roll-over of the devices at lower injection currents [10, 11]. The 28 % increase in the power roll-over value of the devices mounted on the *AlN* sub-mounts is due to the lower junction temperature caused by the increased thermal conductivity of the *AlN* sub-mounts. The *V-I* curve of the devices mounted on *AlN* sub-mounts shows slightly lower device resistance, which is likely to be due to the increased electrical conductivity of the *AuSn* soldering as compared to the conductive epoxy.

7.4 MLLs with Integrated Tapered SOAs: Device Layout

The schematic of a MLL monolithically integrated with a tapered SOA is shown in Figure 7.5. The integrated device consists of four sections, i.e. gain, SA, DBR and a tapered SOA section.

The tapered SOAs were monolithically integrated at the output of the DBR-MLLs in a similar way of to the devices discussed in Chapter 6.
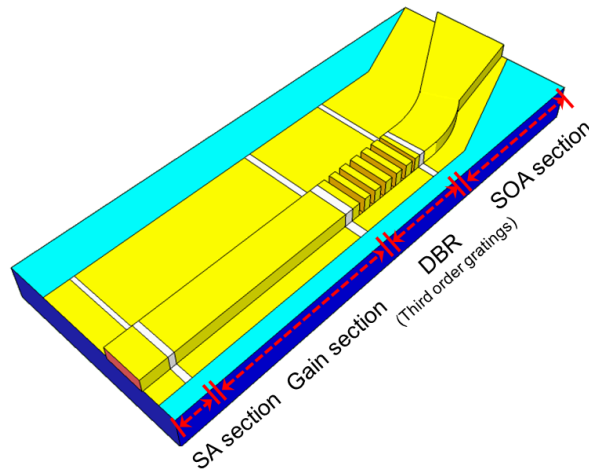
Figure 7.5: Schematic of a DBR-MLL with monolithically integrated tapered SOA.

The total length of the device was 2200 μm with a 30 μm long SA section, 1020 μm long gain section, 150 μm long DBR section and 955 μm long tapered SOA section. Similar to the devices discussed in Chapter 6, the length of the SA was 3 % of the total cavity length. The DBR section consists of 150 μm long 3rd order surface etched gratings with the gratings period of 734 nm. Tapered SOAs with taper angles of 2° and 6° respectively, were integrated with the DBR-MLLs for comparing their performance and beam quality under CW current operation. The output facet of a 955 μm long 2°-tapered SOA was 36 μm wide, whereas that for a 955 μm long 6°-tapered SOA was 105 μm wide. To reduce the facet back reflection into the waveguide, the output waveguide of the SOA was tilted at 10° to the facet. A curved waveguide was required to connect straight (laser section) and the 10° tilted waveguide (SOA section). The radius of the curved waveguide was chosen to be 800 μm, which is significantly larger than the critical bend radius (~ 350 μm) as shown in Chapter 6 (Figure 6.7). Further, this curve waveguide also acts as a spatial mode filter, which cut off the higher order modes in the waveguide [12].

7.5 Output Power Measurements of MLL integrated with 2° Tapered SOAs

As shown in Chapter 6 (Section 6.5.1), the maximum output power of the MLL with integrated narrow ridge waveguide SOAs was limited by the saturation characteristics of the

integrated SOAs. The reason of integration of tapered SOAs to the MLLs in this work was to further increase the output power of the laser by taking advantage of the improved saturation characteristics of the tapered SOAs. These devices were mounted on the *AlN* sub-mounts using *AuSn* eutectic solder and were tested on a temperature controlled *Cu* heat sink with the temperature set at 20°C. All the measurements were carried out by reverse biasing the SA section, whereas forward biasing the gain, DBR and SOA sections. The output power measurements were performed to analyse the effect of the integrated tapered SOAs on the output power of the MLLs.

The *L-I* curves and the average output power map of these devices, as shown in Figure 7.6, were measured under the CW current conditions. The output light at the SOA facet was collected using a broad area Germanium based photodetector, while the DBR current and the SA reverse voltage were fixed at 5 mA and 3.2 V, respectively. In order to observe the effect of the SOA bias on the output power of the device, the output power for SOA current ranging from 600 to 900 mA was measured.
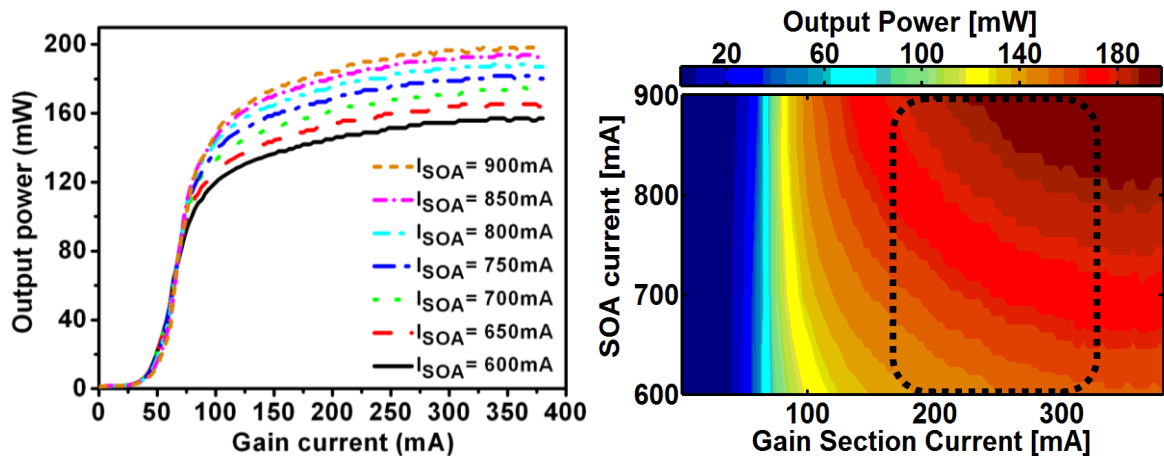
Figure 7.6: Measured (Left) *L-I* curves for different SOA currents and (Right) average output power map for different SOA and gain currents for I_{DBR} = 5 mA and V_{SA} = -3.2 V, respectively.

It is evident from the *L-I* curve that the output power increases with increasing the SOA current. At gain current of 340 mA and SOA current of 900 mA, the maximum average output power obtained was around 200 mW. Increasing the SOA current above 900 mA, there is no further increase in the output power of the device. This is due to the output power roll-over as discussed in Section 7.3.1. Figure 7.6 (right) shows the average output power contour map as a function of gain current and SOA current, whereas the DBR current and the SA reverse voltage were fixed at 5 mA and 3.2 V, respectively. The region enclosed by the dotted black

lines in the output power map indicates the output power of the device corresponding to the optimal mode locking of the device. The optimal mode locking of these devices occurs in the range of gain current from around 180 to 350 mA and SA reverse voltage from around 2.3 to 4 V. The maximum average output power of these devices corresponding to the mode locking regime is around 200 mW. The maximum average output power obtained at the SA facet of the device under the mode locking operation was around 40 mW. These results shows that the integration of tapered SOA at the output facet of the device increased the average output power in the mode locked operation by around 5 fold.

7.6 Far-field Results of MLLs Integrated with 2° Tapered SOAs

The far-field of the devices integrated with 2° tapered SOA was simulated with 3-D beam propagation simulations using a commercial mode solver, BEAMPROP. First, the fundamental mode for a 2.5 µm wide and 1.92 µm high ridge waveguide was computed, and then this fundamental mode was used as an input to the 2° tapered waveguide. After propagation in the 1000 µm long, 2° tapered waveguide, the far-field was computed, which is shown in Figure 7.7. In the plot, each colour from the centre represents a 12% decrease in the intensity. The FWHM of the simulated far-field in the horizontal and vertical direction is 2.3° and 24°, respectively.
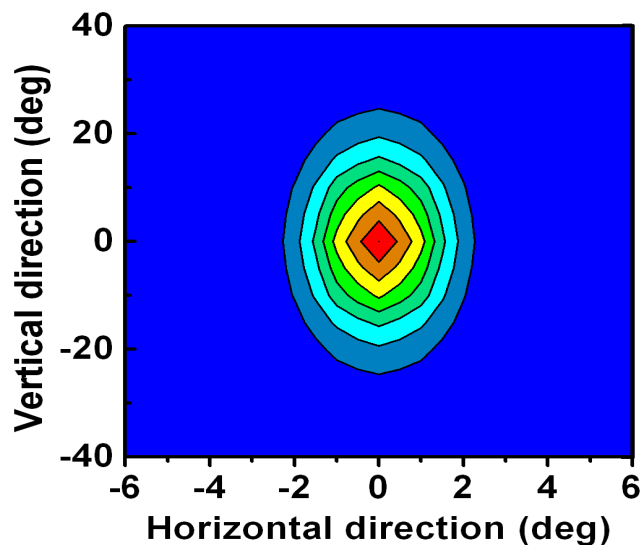

Figure 7.7: Simulated far-field of the 2° tapered waveguide using 3-D BPM simulations. Each colour from the centre represents a 12% decrease in the intensity.

Similar to the devices discussed in Chapter 6, the far-field of these devices was measured at the 36 µm wide tapered-SOA facet with the detector placed at around 5 mm away from the device facet. The schematic of the experimental setup used for these measurements was given in Chapter 4 (Figure 4.19). The device was mounted on a heat sink with the temperature controlled at 20°C and tested under the CW current. Figure 7.8 shows the 2-D picture of the measured far-field. The figure shows that the output is single moded, symmetric, and due to the 10° tilted waveguide of the tapered SOA, the output is 32° offset in the horizontal direction, which is similar to the results presented in Chapter 6 (Figure 6.15). Figure 7.9 shows the far-field profile in the horizontal and vertical direction, respectively as a function of SOA current for I_{gain}= 340 mA, I_{DBR} = 5 mA and V_{SA}= -3.2 V. The far-field of the device in CW and mode locking operation mode was similar. The FWHM of the measured far-field in the horizontal and the vertical direction is 5.5° and 25°, respectively. The simulation and the measurement results of the far-field are slightly different (particularly in the horizontal direction), which is most likely to be due to the gain saturation and self focussing effects in the device, that are not taken into account in the simulations.
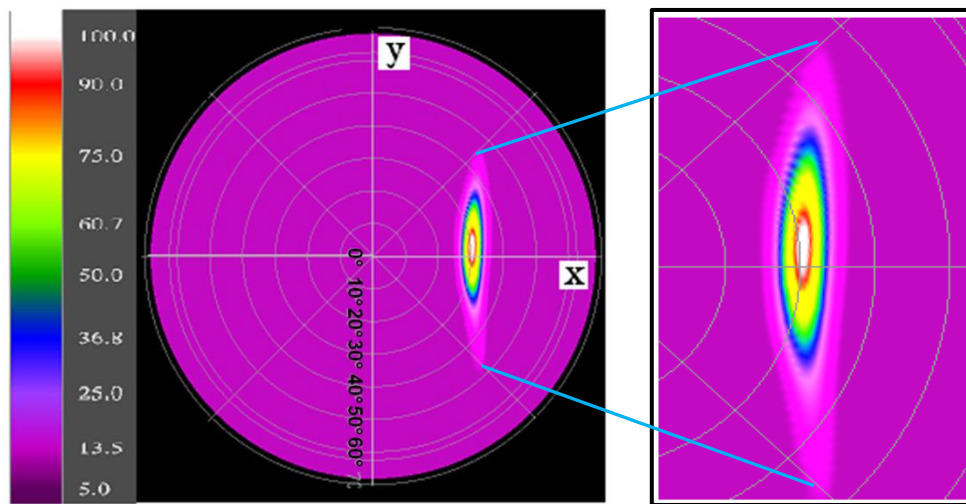
Figure 7.8: 2-D picture of the measured far-field at 36 µm wide SOA facet of the device at I_{gain}= 340 mA, I_{DBR}= 5 mA, I_{SOA}= 900mA and V_{SA}= -3.2 V.

Comparing to the results obtained from narrow ridge waveguide SOA Chapter 6 (Figure 6.16), the reduction of divergence angle in the horizontal direction for these devices is due to the mode expansion in tapered structure of the SOA. Furthermore, an increase in the SOA current does not affect the beam divergence angles and the device emits stable single mode output for a wide range of SOA injection currents.
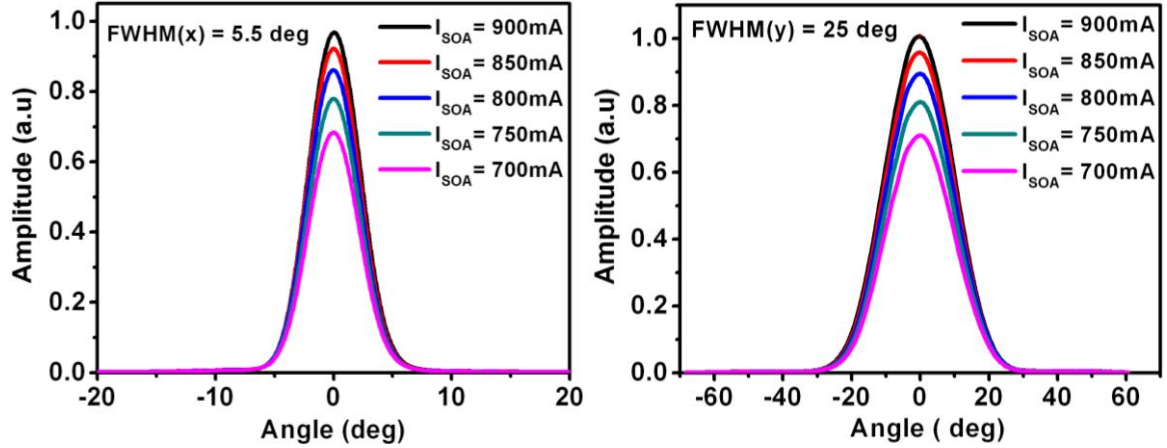
Figure 7.9: Measured far-field at the SOA facet of the device in the horizontal direction (left) and vertical direction (right) as a function of I_{SOA} for I_{gain}= 340 mA, I_{DBR} = 5 mA and V_{SA}= -3.2 V.

7.7 Mode locking Performance of MLLs with Integrated 2° Tapered SOAs

The tapered SOAs integrated at the output of the MLLs were aimed to increase the output power with a minimum effect on the mode locking performance of the device. In this section, the mode locking performance of the MLLs with integrated tapered SOAs will be discussed. The mode locking characterisation was performed at both the SA and the SOA facets, respectively, by measuring the optical spectra, RF spectra and pulse durations. The bias conditions used for mode locking characterisation corresponds to the maximum output power. The measurement setup used for the mode locking characterization of these devices was the same as discussed in Chapter 5.

7.7.1   Optical Spectra Measurements

The optical spectra shown in Figure 7.10 were measured at the SA and the SOA facet of the device, respectively, under the mode locked operation. At both the facets, i.e. SA and SOA facets, the optical spectrum is smooth and symmetric. For measurements at the SA facet, the SOA section was kept floating. As can be seen in Figure 7.10 (left), the optical spectrum at the SA facet of the device is centred at slightly lower wavelengths (1555.9 nm) than that measured at the SOA facet (1556.7 nm) with the SOA biased at 900 mA.
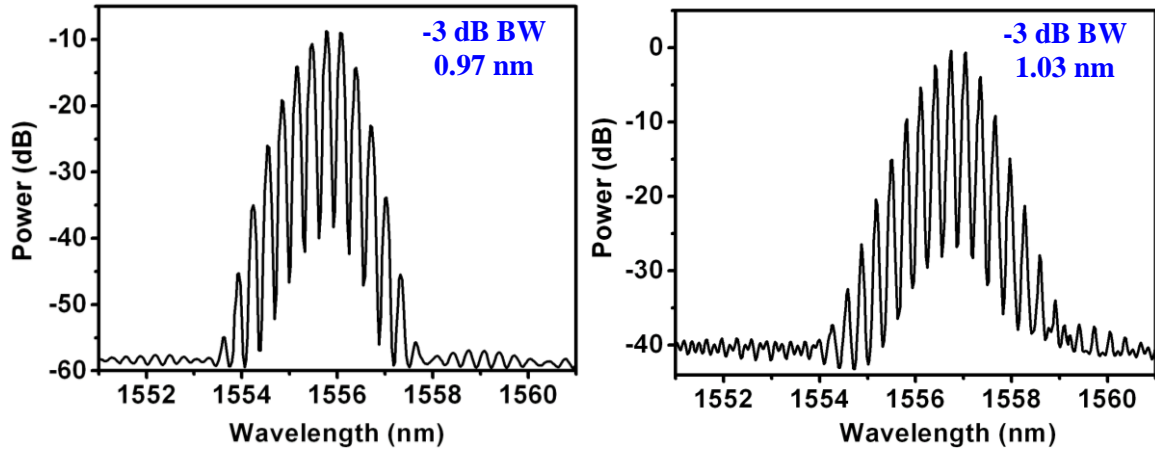
Figure 7.10: Measured optical spectra at the (left) SA side of the device at I_{gain}= 340 mA, I_{DBR}= 5 mA and V_{SA}=-3.2 V and (right) SOA side at I_{gain}= 340 mA, I_{DBR}= 5 mA, I_{SOA}=900 mA and V_{SA}= - 3.2 V.

As compared to the peak wavelength measured at SA facet, a red-shift of 0.8 nm was observed at the SOA facet, which is due to heating up of the device when the SOA section is biased at 900 mA [13]. The results shown in Chapter 6 (Section 6.7), shows that the MLLs integrated with single mode SOAs mounted on the brass mounts exhibits peak wavelength red shift of 1.2 nm at SOA section current of 250 mA. The smaller red shift observed in the peak wavelength of the devices mounted on the *AlN* sub-mounts using *AuSn* soldering, is due to the better heat sinking of the devices. The 3-dB bandwidth of the optical spectrum measured at the SA facet of the device is 0.97 nm, while that at the SOA facet is 1.03 nm. The main cause for larger spectral bandwidth measured at the SOA facet is the self phase modulations (SPM) in the SOAs, as discussed in Chapter 6 (Section 6.7).

7.7.2   RF spectra measurements

The RF spectra measured in the mode locking operation at the SA (left) and SOA (right) facets of the device, respectively, are shown in Figure 7.11. The RF spectra measured at the SA facet and SOA facets indicates the presence of peak at around 38.23 GHz and 38.24 GHz, respectively. While measuring the RF spectra at the SA facet, the SOA section was floating. The RF spectrum measured at the SOA facet shows a slightly higher repetition frequency than that at the SA facet, which is due to the heating of the device at higher SOA section current (900 mA) [14]. The peak amplitude of the RF peak in each case is around 45 dB above the noise floor, which suggests stable mode locking of the device.
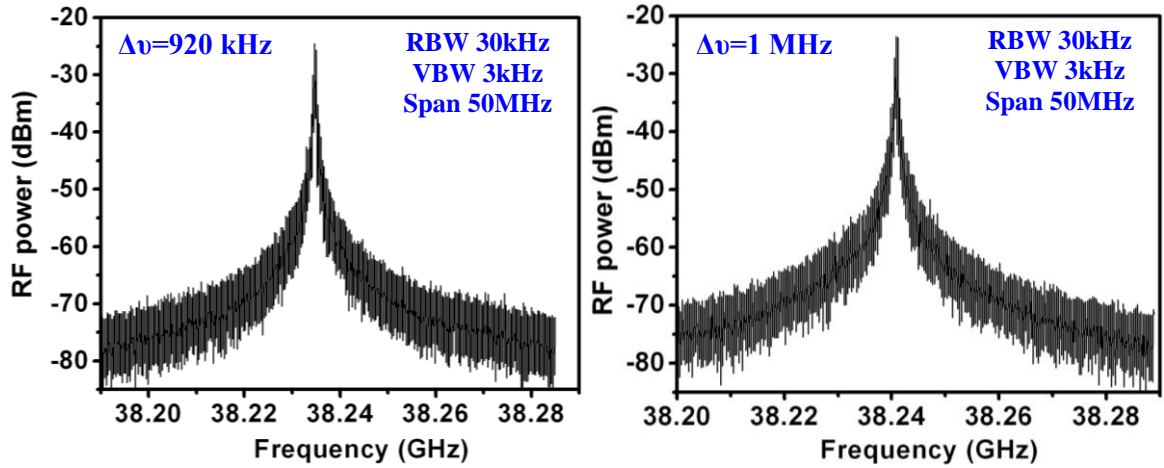
Figure 7.11: Measured RF spectrum at the SA facet (left) and SOA facet (right) of the device at I_{gain}= 340 mA, I_{DBR}= 5 mA and V_{SA}= - 3.2V, (right) I_{SOA}= 900 mA.

The 3 dB linewidth of the RF spectrum by fitting the Lorentzian fit, at the SA and SOA side is found to be 920 kHz and 1 MHz (measured with 30 kHz resolution bandwidth), respectively. The RF spectra performance of the device suggests minimal effects of the tapered SOA integration at the output of the DBR-MLL.

7.7.3   Pulse Width Measurements

The optical pulses measured at the SA facet of the device, while the SOA section floating and the SOA facet, for SOA current of 900 mA are shown in Figure 7.12. The repetition rate of these devices, i.e. ~ 38.2 GHz was confirmed from the spacing between the two adjacent pulses in the measured pulse train.
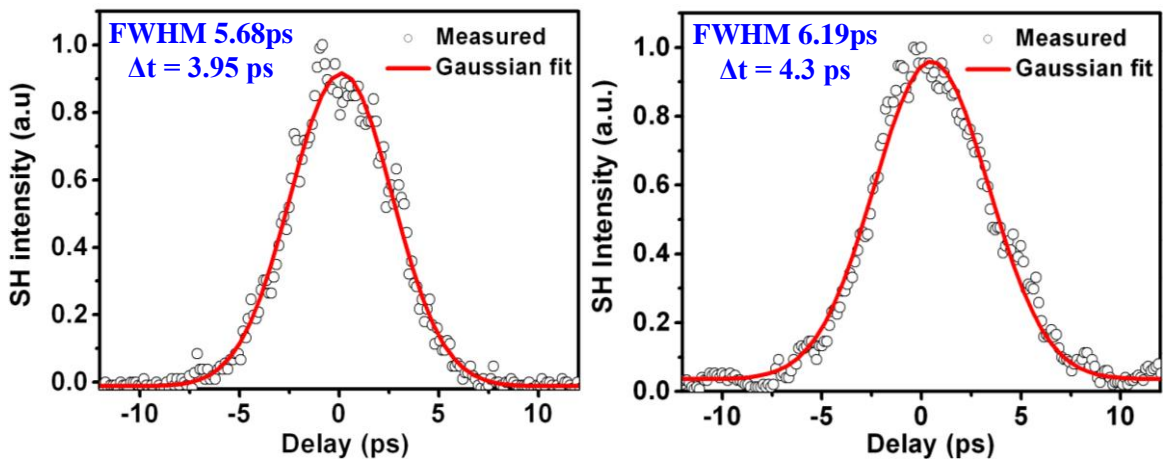

Figure 7.12: Measured SHG intensity autocorrelation pulses at the SA (Left) and the SOA facet (Right) of the device at I_{gain}= 340 mA, I_{DBR}= 5 mA, V_{SA}= - 3.2 V, and (Right) I_{SOA}= 900 mA.

The most appropriate fitting curve for the SHG autocorrelator traces emitted at both the SA and the SOA facet was found to be the Gaussian fit. A single pulse emitted at the SA facet (left) and the SOA facet (right) with a Gaussian fit is shown in Figure **7.12**. Corresponding to the same bias conditions, i.e. gain current, SA reverse voltage and DBR current, the pulse duration at the SA facet was found to be 3.95 ps, while that at the SOA facet was 4.3 ps (SOA biased at 900 mA). The pulse width measured at the SOA facet of the device is larger than that obtained at the SA facet under the same bias conditions. This suggests SPM effects [15] and pulse distortion due to the gain compression of the integrated tapered SOA. In order to observe the effect of the SOA injection current on the measured pulse width, the pulse width of the emitted pulses was measured at the SOA facet, for SOA currents ranging from 600 to 950 mA. Figure 7.13 shows the SHG autocorrelation pulse width as a function of SOA current for gain current of 340 mA, DBR current 5 mA and SA reverse voltage 3.2 V. The blue dashed line corresponding to 3.95 ps in the plot indicates the pulse width of the SHG autocorrelation traces measured at the SA facet of the device with SOA unbiased. From the plot, it can be clearly seen that there is a trend of increase in the pulse width with increase in the SOA current. It is anticipated that this is caused by the SPM and gain compression based pulse distortion, which will increase with increasing the gain of the SOA. Increasing the SOA current from 600 to 950 mA causes around 0.2 ps increase in the pulse width, which is not significantly large. However, comparing to the pulse width obtained at the SA facet, there is an increase of around 10 % in the pulse width measured at the SOA facet of the device.
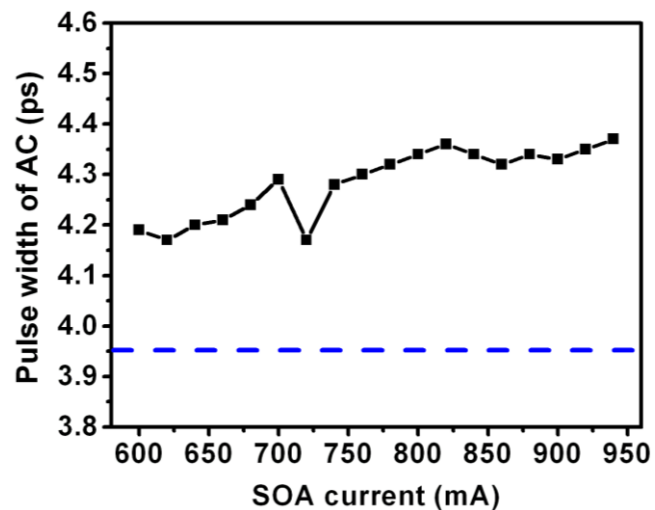

Figure 7.13: Measured pulse widths at the SOA facet of the device as a function of SOA injection current at I_{gain}= 340 mA, I_{DBR}= 5 mA and V_{SA}= -3.2V.

7.8 Output Peak Power and Time Bandwidth Product

The output peak power (indicated by the black colour) and the TBP of a MLL integrated with 2° tapered-SOA (indicated by the red colour) as a function of SOA current for I_{gain}= 340 mA, I_{DBR}= 5 mA and V_{SA}= - 3.2 V is shown in Figure 7.14. As expected, the output peak power at the SOA facet increases with increasing the SOA current and gets constant at around 900 mA, which is due to the output power roll-over of the SOA. The pulse energy and the output peak power at I_{gain}= 340 mA, I_{DBR}=5 mA and V_{SA}= - 3.2 V is 5.23 pJ and > 1.2 W, respectively. The pulse energy and the output peak power measured at the SA facet of the device under the same bias conditions are around 1.04 pJ and 260 mW, respectively. By integrating tapered-SOA with the MLL, the output peak power is increased by around 4.6 times. The plot shows that the TBP slightly increases with increasing the SOA current, which is due to the SPM [15]. The dashed red line shown in Figure 7.14 indicates the TBP measured at the SA facet of the device with SOA unbiased. Assuming Gaussian shaped pulses, nearly transform limited output over a wide range of SOA injection currents was obtained at the SOA facet.
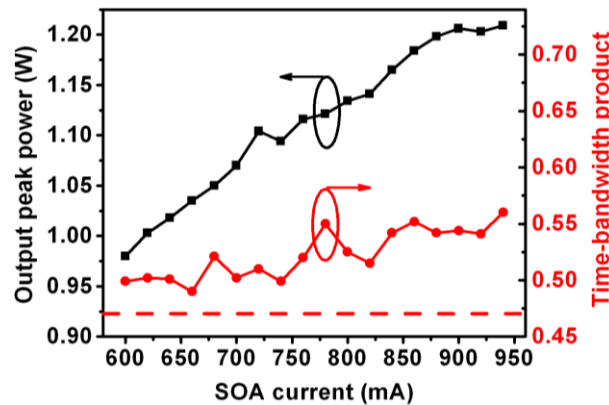
Figure 7.14: Measured peak power and TBP as a function of SOA injection current at the SOA facet of the device at I_{gain}= 340 mA, I_{DBR}= 5 mA and V_{SA}= - 3.2 V.

7.9   MLLs Integrated with 6°-Tapered SOAs

To investigate the effects of integrated SOA on the output power of the MLLs, different types of SOAs, such as single mode SOAs, 2° tapered SOAs and 6° tapered SOAs were integrated with the DBR-MLLs. The results obtained from the DBR-MLLs integrated with the single mode SOAs and 2° tapered SOAs were presented earlier. The devices with 2° tapered SOAs produce higher output powers as compared to the devices with the narrow ridge waveguide SOAs. This is due to the increased saturation output power and better heat sinking. To further

improve the output power, MLLs integrated with 6° tapered SOAs were also fabricated. The schematic of the integrated device is the same as given in Figure 7.5.

These devices were mounted on the conventional brass sub-mounts using conductive epoxy and placed on a temperature controlled *Cu* heat sink, with the temperature controlled at 20°C. These devices couldn't be mounted on the *AlN* sub-mounts due to limited number of devices available after the cleaving. The devices were measured under the CW current conditions and the output power at the SOA facet of the device was measured using a broad area Germanium based photodetector. Figure 7.15 shows the *L-I* curve as a function of SOA current, for SOA current range of 450 to 700 mA at I_{DBR} 5 mA and V_{SA} -3.5 V. The output power increases with increasing the SOA current. At the gain current of 250 mA, SOA current of 700 mA, and SA reverse voltage of 3.5 V, the maximum output power obtained is around 105 mW. For further higher SOA currents, there is no increase in the output power of the device. The maximum output power is limited by the output power roll-over of the devices as discussed in Section 7.3.1.
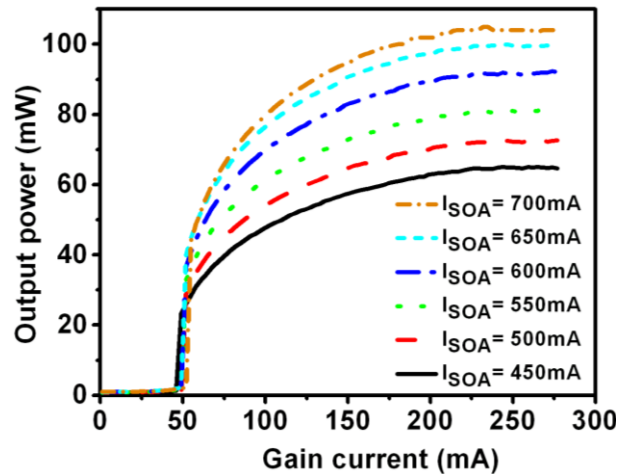
Figure 7.15: Measured output power vs. gain current for different SOA currents at I_{DBR} = 5 mA and V_{SA} = -3.5 V.

Due to the larger pumped area of the 6°-tapered SOAs as compared to the 2° tapered SOAs, higher injection current is required for getting higher output power from these devices. However, higher CW injection current would cause more heating in the device, which in turn reduces the optical gain due to increase in the losses and non-radiative recombination [10]. These effects limit the maximum output power, obtained from the device in the CW current operation. From the threshold current behaviour of the device shown in Figure 7.15, one could

clearly see an increase in the threshold current for increase in the SOA current. This shows the self-heating of the devices.

Due to the lower output power of the MLLs integrated with 6°-tapered SOAs as compared to the MLLs integrated with 2° tapered SOAs, no further measurements were performed on these devices. However, the devices with 6°-tapered SOAs are expected to exhibit better output power performance under pulsed current conditions. Maximum output power from the devices with 6° tapered angles can be obtained when tested under the pulsed current conditions, where the influence of the thermal effects is minimum [16, 17]. The performance of these devices under the pulsed current could not be examined within the timescale of this PhD project.

7.10   Chapter Summary

The basic operation principles of the tapered SOAs were discussed. Efficient heat sinking plays an important in the device operation. Devices mounted on the *AlN* sub-mounts using *AuSn* eutectic solder showed improved output power roll-over, increased slope efficiency and lower series resistance. The devices layout and the output power results obtained from the mode locked DBR lasers with integrated 2° tapered SOAs, mounted on the *AlN/AuSn* were presented. An average output power of 200 mW was obtained at the SOA facet of the device. The measured far-field pattern showed symmetric and stable single-moded output with the divergence angles of 5.5° and 25° in horizontal and vertical directions, respectively. The effect of the integrated tapered SOA on the mode locking performance of the MLL was investigated. The recorded optical spectra, RF spectra and SHG autocorrelation measurements, measured at both the SA and SOA facets showed minimal effects of the output SOA on the mode locking performance of the device. The measured results showed maximum output peak power > 1.2 W with nearly transform limited output for a wide range of SOA currents. The output power measurements of the MLLs with 6° tapered SOAs mounted on the conventional brass sub-mounts were presented. Due to the device self-heating at higher CW injection currents, these devices showed lower output power as compared to the MLLs integrated with the single mode SOAs and 2°-tapered SOAs, respectively.

The devices with integrated 6° tapered SOAs may exhibit improved output power performance with better heat sinking or measuring the devices under pulsed current conditions. The output peak power of the SMLL integrated with SOA, could be further improved by increasing the

reflection bandwidth of the intra-cavity reflector, which would reduce the pulse width and hence increase the peak power.

7.11 References

1. L. Goldberg, et al., *12 W broad area semiconductor amplifier with diffraction limited optical output.* Electronics Letters, 1991. 27(11): p. 927-929.

2. G. Bendelli; K. Komori.; S. Arai.; Y. Suematsu, *A new structure for high-power TW-SLA* IEEE Photonics Technology Letters, 1991. 3(1): p. 42-44.

3. F. Koyama, *Tapered Semiconductor Optical Amplifiers for Broad-Band and High-Power Operations*, in *22nd European Conference on Optical Communication - ECOC'96,*. 1996: Oslo.

4. Luis Borruel, et al., *Design strategies to increase the brightness of gain guided tapered lasers.* Optical and Quantum Electronics, 2008. 40: p. 175-189.

5. Xingsheng Liu, et al., *Thermal Management Strategies for High Power Semiconductor Pump Lasers.* IEEE Transactions on Components and Packaging Technologies, 2006. 29(2): p. 268-276.

6. Alexei. Tsekoun, et al., *Improved performance of quantum cascade lasers through a scalable, manufacturable epitaxial-side-down mounting process.* Proceedings of the National Academy of Science. 103(13): p. 4831-4835.

7. J.W.R. Tewa, X.Q. Shib, and S. Yuana, *Au/Sn solder for face-down bonding of AlGaAs/GaAs ridge waveguide laser diodes.* Materials Letters, 2004. 58: p. 2695-2699.

8. Xingsheng Liu; Hu Martin Hai.; Hong Ky Nguyen; Catherine.G. Caneau, M.H.R.R.W.D. Jr.; Chung-En Zah, *Comparison between epi-down and epi-up bonded high-power single-mode 980-nm semiconductor lasers.* Advanced Packaging, IEEE Transactions on, 2004. 27(4): p. 640-646.

9. Available Online: http://www.ceramic-substrates.co.uk/bespoke_ceramics/aluminium_nitride.html.

10. Joachim Piprek, J. Kenton White, and Anthony J. Spring Thorpe, *What Limits the Maximum Output Power of Long-Wavelength AlGaInAs/InP Laser Diodes?* IEEE Journal of Quantum Electronics, 2002. 38(9): p. 1253-1259.

11. Govind P. Agrawal and Niloy K. Dutta, *Long-wavelength semiconductor lasers*. 1986: Van Nostrand Reinhold.

12. R. B. Swint, et al., *Curved Waveguides for Spatial Mode Filters in Semiconductor Lasers.* IEEE Photonics Technology Letters, 2004 16(1).

13.   Wei Kiong Tan, *High operating temperature of passively mode-locked InGaAsP/InP semiconductor lasers*, in School of Engineering. 2005, University of Glasgow.

14.   Wei Kiong Tan, et al., *Temperature Behaviour of Pulse Repetition Frequency in Passively Mode-Locked InGaAsP/InP Laser Diode—Experimental Results and Simple Model.* IEEE Journal of Selected Topics in Quantum Electronics. 2007. 13(5).

15.   Dennis J. Derickson, et al., *Short pulse generation using multisegment mode-locked semiconductor lasers.* IEEE Journal of Quantum Electronics. 28(10): p. 2186-2202.

16.   D. Mehuys, L. Goldberg, and D. F. Welch, *5.25 W CW Near-diffraction Limited Tapered Stripe Semiconductor Optical Amplifiers".* IEEE Photonics Technology Letters, 1993. 5(10).

17.   Thorsten Ulm, et al., *InGaAs diode laser system generating pulses of 580fs duration and 366 W peak power.* Applied Physics B: Lasers and Optics, 2008. 92: p. 481-485.

Chapter 8

Summary and Conclusions

8.1 Conclusions

This Chapter presents a summary of the research work presented in this thesis and also provides some suggestions for future work. This thesis was mainly focused on the investigation and development of high output power monolithically integrated semiconductor mode-locked lasers (SMLLs), operating at wavelength of 1.55 μm. A new epitaxial structure designed by a colleague Dr Lianping Hou, was used for the fabrication of devices, which led to high output power, shorter optical pulses and lower beam divergence angles. The novel material design provided a low loss waveguide and low confinement active layer material providing higher saturation energy of the gain medium. A farfield reduction layer (FRL) inserted in the n-cladding layer increases the mode spot size that leads to reduced divergence angles.

To realise high output power SMLLs, 40 GHz SMLLs monolithically integrated with surface etched DBR gratings and 1 mm long narrow ridge waveguide SOAs were designed, fabricated and tested. The effects of the integrated SOA on the output power and the mode-locking performance of the SMLL were investigated. A maximum average output power of 130 mW with corresponding peak power of > 1 W, was obtained under mode locked operation. To further improve the output power, SMLLs monolithically integrated with the tapered SOAs were also designed and fabricated. Better heat sinking was provided by using *AlN* sub-mounts and *AuSn* soldering to allow higher CW currents required by the tapered SOAs. The SMLLs integrated with 1 mm long 2°-tapered SOAs resulted in a maximum average output power of

200 mW and peak power of 1.2 W, under mode locked operation. Further, the SMLLs integrated with the 1mm long 6°-tapered SOAs mounted on conventional brass sub-mounts, resulted in an average output power of 105 mW. It was supposed that the output power of these devices was limited by the heating effects occurring at the higher CW injection current. However, these devices are expected to exhibit better output power performance under pulsed current conditions.

8.2 Review of the Work Presented

Chapter 1 introduced this research work based on SMLLs, which are attractive pulse sources due to their excellent intrinsic properties such as greater stability, compact size, ease of integrability and direct electrical pumping. The main focus of this PhD project and the summary of the main achievements related to this work were given. The outline of this thesis was also presented in this Chapter.

Chapter 2 briefly discussed the modern optical communication systems and multiplexing schemes for increasing the transmission capacity of the optical fiber links. The potential applications of SMLLs and various common approaches used to increase the output power of SMLLs were discussed. Of these approaches, the master oscillator power amplifier approach was chosen to realize high power SMLLs in this work.

Chapter 3 started with a brief introduction of semiconductor lasers. Various methods for producing short optical pulses from the semiconductor lasers were given. Description of the active, passive and hybrid mode-locking schemes were presented with special attention given to the passively mode-locked lasers, since it was the type of SMLLs lasers fabricated in this research work. This was followed by the review of the basic theory of SOAs. Basic characterisation of the fabricated SOAs including the ASE spectra, the optical gain and the saturation output power were discussed. Tilted facets structures and anti-reflection (AR) coatings for reduction of effective facets reflectivity was briefly discussed. Various processes occurring during pulses amplification in the amplifiers were discussed. Finally, the SMLLs with integrated DBRs were introduced.

Chapter 4 started with an introduction of QW lasers. It described the basic properties of the AlGaInAs/InP multiple quantum well (MQW) epitaxial structures. The design of the epitaxial structure for realizing high power SMLLs in this project was given. This material design was based on the standard commercially available epitaxial design for lasers. The number of QWs

in the active region were reduced from five to three and a 160 nm thick FRL and 75 µm thick spacer layers were inserted in the n-cladding layer. The FRL pulls the optical mode towards the n-cladding layer causing reduction in the optical overlap with the p-cladding layer. This structure resulted in an increase in the mode spot size and hence reduced farfield. Further, the insertion of the FRL gives a better suppression of lasing of higher order transverse modes. The key fabrication tools and processes used in this work were described. An introduction of the electron beam (e-beam) lithography and the e-beam resists was given. The AlGaInAs/InP epitaxial material with a dry etch stop layer facilitate the controlled etching and accurate etch depth by using $CH_4/H_2/O_2$ etch chemistry for RIE dry etching.

Single lateral mode waveguides were modelled using 3-D beam propagation simulations. The optimum waveguide width was found to be 2.5 µm for 1.92 µm high ridge waveguides. Ridge waveguide lasers were fabricated and characterized to access the quality of the epitaxial material. The internal quantum efficiency of 86 %, internal losses of 4.8/cm, and threshold current density for infinite length of 550 A/cm^2 were obtained. The measured farfield results show the beam divergence angles of 22° x 26° in the horizontal and vertical directions, respectively.

Chapter 5 was mainly concerned with the comparison of mode locking performance of the devices based on the novel three-QW and standard commercially available five-QW active region epitaxial materials. Compared to the ridge waveguide lasers based on five-QW material, the devices based on three-QW material showed a 126 % increase in output power, a 43 % decrease in the internal optical losses and significant decrease in the beam divergence angles. Similarly, comparing to the MLLs based the five-QW epitaxial material, the SMLLs based on the three-QW material showed 85 % reduction in the RF linewidth, 31 % reduction in the pulse width and a broader region of optimal mode locking. The higher gain saturation energy and the lower ASE coupling co-efficient of the three-QW epitaxial structure results in narrower temporal width pulses, lower RF linewidth, lower timing jitter and broader region of mode locking.

Modelling results of the 3rd order surface etched DBR gratings were presented. Monolithic DBR-MLLs were designed, fabricated and characterised before then being monolithically integrated with the SOAs.

Chapter 6 mainly focussed on the measurement results obtained from the discrete SOAs and the DBR-MLLs monolithically integrated with the narrow ridge waveguide SOAs. The 1 mm

long, stand-alone SOAs with the waveguide tilted at 10° to the facet resulted in small signal gain of 17 dB and saturation output power of 15.8 dBm.

To allow 10° tilted facets of the SOAs in the integrated devices, curved waveguides were used. The simulations performed using the 3-D beam propagation showed that the critical curve radius for 1.92 µm high and 2.5 µm wide ridge waveguides was around 350 µm.

The 40 GHz DBR-MLLs monolithically integrated with 1 mm long curved SOAs were designed, fabricated and characterized. These devices were characterized both at the SA and SOA facets in terms of the optical power, optical spectra, RF spectra and SHG-autocorrelation. The maximum average output power obtained from the device at the SOA facet under the mode-locked conditions was 130 mW with corresponding peak power of > 1 W. The output power from the same device under the same bias conditions measured at the SA facet was only 28 mW.

Furthermore, these devices produced 3.3 ps wide pulses with optical spectrum bandwidth of 1.14 nm and RF linewidth of 1.3 MHz. The time bandwidth product was found to be around 0.47 for a wide range of SOA currents. The maps of optical spectra, RF spectra and SHG intensity autocorrelation measurements obtained at both the SA and SOA facets suggested minimal effects of the output SOA on mode-locking performance of the DBR-MLLs.

The maximum output power of these devices was limited by the output power saturation of the SOAs. The use of tapered SOAs will result in increased saturation output power of the SOAs and hence the output power of the devices.

Chapter 7 presented the results of DBR-MLLs integrated with tapered SOAs. The tapered SOAs were integrated to the MLLs to further increase the output power of the devices. To investigate the device performance while under CW operation, a number of SOAs with different taper angles were integrated with the MLLs. Due to high CW current requirements of the tapered SOAs, improved heat sinking using Aluminium Nitride (*AlN*) sub-mounts and Gold-Tin (*AuSn*) eutectic solder was used. Comparing to devices mounted on conventional brass sub-mounts using conductive epoxy, the devices mounted on *AlN* sub-mounts using *AuSn* solder showed around 28 % improvement in the output power.

DBR-MLLs with integrated 1 mm long tapered SOAs with the taper angle of 2° and 6° were fabricated. To allow 10° tilted facet of the integrated SOAs at the output, curved waveguides, with curve radius of 800 µm were used.

Maximum average output power of 200 mW and corresponding peak power of 1.2 W, measured at the SOA facet under the mode-locked operation was obtained. Minimum pulse width of 4.3 ps with the spectral width of 1.03 nm and the RF bandwidth of 1 MHz were obtained. To investigate the effects of the SOA on the mode-locking performance of these devices, optical spectra, RF spectra, and pulse width were measured both at the SA and SOA facets. These measurements showed negligible effects of the output SOA on the mode-locking performance of these devices. The Farfield pattern was measured at the SOA facet for SOA injection current of 900 mA. The FWHM of the farfield in the horizontal and vertical directions were found to be 5.5° and 25° respectively.

The DBR-MLLs integrated with 6°-tapered SOAs showed a maximum average output power of 105 mW. Comparing to the devices integrated with 2°-tapered SOAs, the lower output power of these devices is likely to be due to the thermal effects caused by the higher current requirements due to the larger effective area. The higher CW injection current causes excessive heating effects in the device, which limits the maximum output power.

8.3 Future Work

Suggestions of some possible areas for the future work as a follow up to this research work as listed below:

- The output power of the MLLs integrated with the tapered SOAs, especially for 6°-tapered SOAs, is limited due to the excessive heating induced effects at large injection currents. These devices could result in higher output power under pulsed measurements.

- Further improving the waveguide design to increase the modal cross-sectional area will led to increased average output power.

- Devices based on the slab coupled optical waveguides may also be investigated with monolithically integrated SOAs.

- Increasing the reflections bandwidth of the intra-cavity reflector would further reduce the pulse width and hence an increase the output peak power.

- Designing longer laser cavities will decrease the pulse repetition frequency and hence and increase the output peak power.